

**Frontiers of Advanced Materials  
and Engineering Technology**

**Part 1**

Edited by  
Ran Chen, Dongye Sun and Wen-Pei Sung

# **Frontiers of Advanced Materials and Engineering Technology**

Edited by  
Ran Chen  
Dongye Sun  
Wen-Pei Sung

# Frontiers of Advanced Materials and Engineering Technology

Selected, peer reviewed papers from the  
2012 International Conference on  
Frontiers of Advanced Materials and Engineering Technology  
(FAMET 2012),  
January 4-5, Xiamen, China

*Edited by*

**Ran Chen**

Chongqing University of Technology

**Dongye Sun**

Chongqing University

**Wen-Pei Sung**

Chin-Yi University of Technology



**Copyright** © 2012 Trans Tech Publications Ltd, Switzerland

All rights reserved. No part of the contents of this publication may be reproduced or transmitted in any form or by any means without the written permission of the publisher.

Trans Tech Publications Ltd  
Kreuzstrasse 10  
CH-8635 Durnten-Zurich  
Switzerland  
<http://www.ttp.net>

Volumes 430-432 of  
*Advanced Materials Research*      *3-vol.-set*  
ISSN 1022-6680

Full text available online at <http://www.scientific.net>

***Distributed worldwide by***

Trans Tech Publications Ltd  
Kreuzstrasse 10  
CH-8635 Durnten-Zurich  
Switzerland

Fax: +41 (44) 922 10 33  
e-mail: [sales@ttp.net](mailto:sales@ttp.net)

***and in the Americas by***

Trans Tech Publications Inc.  
PO Box 699, May Street  
Enfield, NH 03748  
USA

Phone: +1 (603) 632-7377  
Fax: +1 (603) 632-5611  
e-mail: [sales-usa@ttp.net](mailto:sales-usa@ttp.net)

# Preface

2012 International Conference on Frontiers of Advanced Materials and Engineering Technology (FAMET 2012) will be held in Xiamen, China during January 4-5, 2012. The aim is to provide a platform for researchers, engineers, academicians as well as industrial professionals from all over the world to present their research results and development activities in Advanced Materials and Engineering Technology.

In this conference, we received more than 1000 submission from email and electronic submission system, which were reviewed by international experts, and about 465 papers have been selected for presentation, representing 8 national and international organizations. This high level of interest truly reflects the worldwide importance of Advanced Materials and Engineering Technology. I think that FAMET 2012 will be the most comprehensive Conference focused on the Advanced Materials and Engineering. The conference will promote the development of Materials and Technology, strengthening the international academic cooperation and communications, and exchanging research ideas.

We would like to thank the conference chairs, organization staff, The authors and the members of International Technological Committees for their hard work. Thanks are also given to Trans Tech Publications.

We hope that FAMET 2012 will be successful and enjoyable to all participants. We look forward to seeing all of you next year at the FAMET 2013.

November, 2012

Wen-Pei Sung  
National Chin-Yi University of Technology

Dongye Sun  
Chongqing University

Ran Chen  
Chongqing University of Technology, China  
Conference Chairman

# FAMET 2012 Committee

## Conference Chairman

Prof. Wen-Pei Sung, National Chin-Yi University of Technology, Taiwan  
Prof. Jimmy (C.M.) Kao, National Sun Tat-Sen University, Taiwan

## Publication Chair

Dr. Chen Ran, Chongqing University of Technology, China  
International Frontiers of science and technology Research Association

## International Technological Committees

Yu-Kuang Zhao, National Chin-Yi University of Technology  
Wen-Sheng Ou, National Chin-Yi University of Technology, Taiwan  
Ming-Hsiang Shih National Chi Nan University, Taiwan  
Viranjay M.Srivastava, Jaypee University of Information Technology, Solan, H.P. India  
Liu Yunan, University of Michigan, USA  
Mir Mahdi Zalloi, Iran  
Hsien-Jung Wang, Rong sheng Engineering Design Co., Ltd  
Wang Liying, Institute of Water Conservancy and Hydroelectric Power, China  
Zhou Liang, Donghua University, China  
Chenggui Zhao, Yunnan University of Finance and Economics, China  
Ting-Yu Chen, National Chin-Yi University of Technology, Taiwan  
Tzai-Tang Tsai, National Chin-Yi University of Technology, Taiwan  
Li-Xin GUO, Northeastern University, China  
Hsiang-Chuan Liu, Asia University  
Mostafa Shokshok, National University of Malaysia, Malaysia  
Ramezan ali Mahdavinejad, University of Tehran, Iran  
Anita Kovač Kralj, University of Maribor, Slovenia  
Tjamme Wieggers, Delft University of Technology, Netherlands  
Gang Shi, Inha University, South Korea  
Zengtao Chen, University of New Brunswick, Canada

## Co-sponsors

International Frontiers of science and technology Research Association  
HongKong Control Engineering and Information Science Research Association

# Table of Contents

## Preface and Committee

## Chapter 1: Advanced Materials Science

<b>Effect of a Novel Phosphorus and Silicon System on Flame Retardancy and Thermal Degradation of PC</b> W. Zhao and B. Li	3
<b>Effect of Long-Term Aging on the Tensile Properties of Nickel-Based Superalloy</b> L.W. Xu, H.B. Li, Q.F. Ma and Z.H. Jiang	7
<b>Effect of Fe Doping on the Morphology of Hydrothermally Derived BaTiO<sub>3</sub> Crystals</b> L.L. Yang, Y.J. Wang, S.L. Huang and Y.G. Wang	12
<b>Polaron Effect on the <i>D</i><sup>-</sup> Center at the InP(GaP) Heterointerface in a Magnetic Field</b> X.Y. Zhang and G.L. Fan	16
<b>Effect of Cellulose Nanocrystal on Crystallization Behavior of Poly(3-hydroxybutyrate-co-3-hydroxyvalerate)</b> H.Y. Yu and Z.Y. Qin	20
<b>Preparation and Properties of a Novel Thermosetting Resin Based on 4,4'-Bismaleimidodiphenyl Methane and Allyl COPNA Resin</b> L. Xiong and Q.L. Lin	24
<b>First-Principles Study of the Self-Assembly Monolayer on Silicon (100) Surface</b> L.Q. Shi, F. Yu, X.P. Hu, X.W. Li, T. Sun and S. Dong	28
<b>Li<sup>+</sup> Extraction/Insertion Reaction with MgMn<sub>0.5</sub>Ti<sub>0.5</sub>O<sub>3</sub> Spinel in the Aqueous Phase</b> H. Li	32
<b>1-3xLn<sub>2</sub>xTiO<sub>3</sub> (Ln=La, Nd, Sm) Ceramics</b> B.L. Liang, Y.L. Ai, X.H. Zheng, D.P. Tang and F. He	36
<b>Analysis of Influencing Factors of Ultrasonic Nondestructive Testing with Carbon Fiber Reinforced Plastics</b> D. Xue, J.B. Zhang and C.H. Li	41
<b>Fabricating TiO<sub>2</sub> Coated ZnO Nanowire Array/Graphene Heterostructure</b> Y.Q. He, S.Y. He, N.N. Zhang, W.C. Wang, H. Sun, W. Wang and H.X. Qiu	45
<b>High Functional PET Sericin Composite Fabric</b> G.X. Zhang, X.H. Shi, W. Hu, F.X. Zhang and D.Y. Wu	49
<b>Study on Nitrogen Shock Absorber Oil</b> G.G. Zhang, Z.B. Chang and L.B. Wang	53
<b>The Kinetics and Activation Energy of Photocatalytic Degradation of Phenol by TiO<sub>2</sub> and TiO<sub>2</sub>/PANI Photocatalyst under UV Irradiation</b> X.Y. Li, Q.Z. Luo, J. An and D.S. Wang	57
<b>Effects of SiC Addition on the Properties of MgO-Based Castables</b> J.C. Wei and J.B. Tu	61
<b>Selective Etching of Pressure-Crystallized Bisphenol-A Polycarbonate by Dimethylacetamide at Room Temperature</b> J. Lu and R. Huang	66
<b>Li<sup>+</sup> Extraction/Insertion Reaction with LiTi<sub>1.25</sub>O<sub>3</sub> Spinel in the Aqueous Phase</b> H. Li	70
<b>Sheet Single Point Vibration Incremental Forming Process Simulation and Analysis of Process Parameters</b> G.P. Cai, C.W. Xing, Z.H. Jiang and Z.K. Zhang	74
<b>Graphene Based Ultrahin Composite Films Prepared by Layer-by-Layer Electrostatic Assembly and Spinning Coating</b> Y.Q. He, S.Y. He, Q.J. Gong, J.P. Gao and X.D. Wang	79
<b>Analysis of the Stability of POY Filament Structure and Properties Spun by WINGS System</b> B. Yang, Z.Y. Yan and Y. Xue	83

<b>Influences of Solution Treatment, Deformation Strain and Nanometric Al<sub>2</sub>O<sub>3</sub> Particulate on Hardness for Nanometric Al<sub>2</sub>O<sub>3</sub> Particulate Reinforced Al Alloy Matrix Composites Manufactured by Casting</b>	
Y.B. Yang, Z.M. Zhang and M. Meng	88
<b>Study on the Synthesis and Characters of Waterborne Polyester Resin</b>	
Y. Chen, G.S. Zeng, W.Y. Liu and Y.G. Huang	92
<b>Effect of Carbon Nanotube on Physical and Ablative Properties of Silicone Elastomer</b>	
D. Li, S.X. Wu, Z. Chen, Y. Li and J.G. Wang	97
<b>Laser Cladding of Ni60/WC/TiN Composite Coatings on 00Cr13Ni4Mo Hydro Turbine Blade Stainless Steel for Improvement of Wear Resistance</b>	
K.J. Huang, H.R. Jiang and X. Lin	101
<b>The Stress Relaxation Characteristic and Martensitic Transformation of Fe-Mn-Si Shape Memory Alloys under Different Deformation Condition</b>	
L.L. Liu, C.X. Lin and C.Y. Zhou	106
<b>Effect of Inorganic Flame Retardant on the Properties of Wood/PVC Composites</b>	
K.M. Xu, K.F. Li, Y.P. Deng, X. Yan and C.P. Xie	110
<b>Study on Magnetic Abrasive Machining for the Small Hole</b>	
J.H. Cheng, L. Wu and W.J. Zhang	115
<b>Study on Modification of Micro-Crystal Muscovite by Using of Amino Silane</b>	
J. Liu, Z.W. Hu and M.G. Zhang	119
<b>Resorption Rate of Calcium Sulfate Bone Fillers Adjusted by Incorporation of Hydroxyapatite</b>	
Y.L. Zhang, C. Xu, W.W. Yan, Y. Liu, J.P. Gao and J. Yan	123
<b>Preparation of Activated Carbon with Higher Absorbability from Anthracite</b>	
Q.W. Yang, H. Zhao, J. Chang, K. Wang and L. Tao	127
<b>Formation Reason and Improvement Measure for Surface Defects of 0Cr18Ni10Ti Stainless Steel</b>	
H.L. Wang, H.B. Li, Q.F. Ma and Z.H. Jiang	132
<b>Dissolution Behavior of WC Reinforced Particles on Carbon Steel Surface during Laser Cladding Process</b>	
Z. Zhang, H.X. Liu, X.W. Zhang, S.W. Ji and Y.H. Jiang	137
<b>Damage Mechanism and Fracture Process of Concrete Gravity Dam under Earthquake Action</b>	
J.B. Liu, J.R. Xue and W. Zhu	142
<b>Fabrication and Microwave Characteristics of Fe<sub>3</sub>O<sub>4</sub>/C Composites</b>	
W. Wang, C.G. Wang and Y. Guo	146
<b>Sequestration of Reactive Light-Yellow K-4G by Free <i>Mycobacterium phlei</i> Cells and its Extracellular Polysaccharide</b>	
Y.H. Wang, Z.Y. Liu, C. Ding and H.Q. Xing	150
<b>Dually Responsive Multi-Network Hydrogel of N-Isopropylacrylamide Copolymeric Microgels Embedded in Poly(vinyl alcohol)</b>	
X.M. Ma, Y.H. Li and Y.Z. Xia	154
<b>Study on Effective Elastic Constants of Homogenization Tube Sheet</b>	
Y. Sun, G.Y. Kang, D. Cui and J.R. Ge	158
<b>Synthesis and Luminescent Properties of Europium Chloride with DPA Complexes</b>	
Z.M. Cheng and F.J. Zhang	164
<b>Study on Nonlinear Viscoelasto-Plastic Creep Model of Deep Soft Rock</b>	
Y.C. Wang and Y.Y. Wang	168
<b>First-Principle Study of the Electronic and Optical Properties of Ti Doped ZnS</b>	
C.P. Chen, J.X. Xie and J.F. Wang	173
<b>Numerical Simulation of Cement Concrete Under Corrosion Fatigue</b>	
B.W. Guan, S.F. Chen, Y.P. Sheng and R. Xiong	177
<b>Temperature Field in Simply Supported Laminated Beam</b>	
H. Qian, D. Zhou and W.Q. Liu	181
<b>The Effects of the Development of Teachers Training Programs</b>	
C.Y. Wu, H.Y. Huang and M.C. Huang	185
<b>AirCar CAES-Compressed Air Energy Source-Compendium</b>	
F.A. Wyczalek and C.M. Suh	189

<b>The Study of the Modified Grain Sorghum Stalk to Remove Methylene Blue Dye from Aqueous Solution</b> F.Y. Li, S.H. Zhang and J.Y. Chen	197
<b>Effect of Heat Treatment on the Organization and Properties in Liquid Forging</b> C. Li, J.X. Wang and H.Q. Miao	202
<b>The Synthesis of Novel Material 3,4-ethylenedioxyfuran</b> X.X. Sun, Y.C. Li, L. Li and Y. Hu	205
<b>Research on Heating Resistance in Electric Hot Machining</b> X. Liu, W.J. Xu, J. Sun and L. Zhang	209
<b>Influence of Annealing on Microstructure and Texture of AZ31 Magnesium Alloy Sheet</b> J.Y. Li, Z.H. Yang and J.F. Wang	213
<b>Study on how to Improve Asphalt-Modified with SBS-Added Carbon-Nanotubes-Material</b> Q. Su, L. Sun, W.Y. Yu and G.F. Wang	217
<b>Study on the Application of Catalytic Esterification Modification of Rosin</b> Z.G. Luo, Z. Liu, J.Y. Lin, Q. Wang and C.R. Wan	221
<b>Effect of Temperature and KOH Concentration on Hydrothermal Synthesis of SrTiO<sub>3</sub> Dendrites</b> L.L. Yang, Y.J. Wang, Q.Q. Zou and Y.G. Wang	225
<b>Cracking Analysis of Induction Heat Bend Pipe of X70 Steel</b> L.J. Li, X.D. Huo and L. Guo	229
<b>Enzyme-Mediated Grafting of AGE to Kevlar Fiber Using Horseradish Peroxidase</b> Y. Liu, G.Z. Liang, A.J. Gu and L. Yuan	233
<b>Parametric Study of EAPap Material Properties</b> L.J. Zhao and Q. Fu	242
<b>Preparation of Reduced Graphene Oxide/Chitosan Composite Films with Reinforced Mechanical Strength</b> Y.Q. He, N.N. Zhang, W.C. Wang, S.Y. He, Q.J. Gong, H.X. Qiu and W. Wang	247
<b>Research on the Wear Properties of HVOF Sprayed Nanostructured WC-17Co Coatings</b> G.Q. Gou, D. Li, N. Huang, Y. Liu, H. Chen and L.C. Meng	251
<b>Effect of Strain Rate on the Microstructures and Properties of Hot-Rolled TWIP Steel in the Solution Condition</b> Y. Yang, C.F. Li and K.H. Song	256
<b>Synthesis of a New Platinum Metallopolyyne for Organic Solar Cells</b> L. Li, X.X. Sun, Y. Hu and Q.H. Wu	260
<b>Modified Phenolic Resins Based on Hyperbranched Polysiloxane with Improved Thermal Stability and Flame Retardancy</b> C.L. Gu, A.J. Gu, G.Z. Liang and L. Yuan	264
<b>The Effect of Cr Content on the Microstructure and Performance of Heat Resistant Nodular Cast Iron</b> H.B. Li, H.T. Li, C.J. Li and L.J. Qu	273
<b>Research on Compact Resistance Performance of Flexible Fiber and Rigid Fiber Reinforced Concrete</b> Y.M. Wang, W.W. Yang, Y. Sun and K. Liu	277
<b>Study on Microwave Curing Behavior and Performance of Epoxy/Versamid 125</b> Y.B. Lei and X.J. Cao	281
<b>Damage Study on AZ31 Mg Alloy under Bending Load</b> M. Tan, Z.M. Liu, G.F. Quan, Z. Chen, Z. Zhang and G.R. Xu	285
<b>Synthesis of Acetals and Ketals Catalyzed by H<sub>4</sub>SiW<sub>6</sub>Mo<sub>6</sub>O<sub>40</sub>/SiO<sub>2</sub></b> S.J. Yang, L. Yu, Y.K. Huang and G.B. Duan	289
<b>Simulation Analysis of Metal Flow during Extending Extrusion Semisolid AA2017 Alloy</b> R.G. Guan, Z.Y. Zhao, C. Lian, Q.S. Zhang, C.G. Dai and C.M. Liu	293
<b>Damping Property of Polyurethane/Poly(methylmethacrylate-butylmethacrylate-2-Hydroxyethyl methacrylate) Interpenetrating Polymer Networks</b> G.J. Song, M.J. Liu, J. Yi and Y.G. Xu	297
<b>Rheological Properties of Blend Spinning Solution of Sodium Alginate and TiO<sub>2</sub> Nanoparticles</b> L.W. Tan, D.M. Xu, Q. Ji, B.B. Wang and Y.Z. Xia	301

---

<b>Study on the Machinability of Free Cutting Non-Lead Austenitic Stainless Steels</b> D. Wu and Z. Li	306
<b>Effect of Na-Doped Concentration on the Structure and Optical Properties of ZnO Thin Films</b> W. Wang, W. Meng, M.H. Liu and X.B. Wang	310
<b>Synthesis and Photoluminescence Properties of Two-Bands Excited SrSi<sub>2</sub>O<sub>2</sub>N<sub>2</sub>: Yb<sup>2+</sup> Phosphors</b> X.W. Xu, K. Fu, L. Hu, Z.M. Lu, X.H. Zhang and C.C. Tang	315
<b>Mechanical Properties of Cement Concrete under Corrosion Fatigue</b> B.W. Guan, S.F. Chen, R. Xiong and Y.P. Sheng	319
<b>Research on the Influence of Surface Sizing on Handmade Xuan Paper's Modification</b> W.G. Bai and L.Z. Wang	323
<b>A pH and Electric Responsive Graphene Oxide Based Composite Hydrogel</b> Y.Q. He, H.B. Chen, H. Sun, X.D. Wang and J.P. Gao	327
<b>The Study on Carbon Fiber Reinforced Concrete Beams Based on Finite Element Analysis</b> J.H. Wang	331
<b>Thermodynamics Software Development on Composition Prediction of Inclusions in Molten 430 Stainless Steel</b> Y. Zhuang, Z.H. Jiang and Y. Li	337
<b>Crack Size Tolerance of Under-Matched Joints of Hull Steel with Different Weld Toughness</b> J. Sun, C.B. Gui and W.J. Chen	341
<b>Preparation and Laboratory Study of Cationic Copolymer Clay Stabilizer PDA</b> Z.Z. Fan and C. Li	345
<b>Process Conditions of Exfoliated Single-Layer Graphite</b> C. Yang, T.Y. Zhao, L.J. Sun, H.S. Song and D.B. Liu	350
<b>Study on Mathematical Model of Homogenization of Dendritic Segregation</b> X.G. Liu, B. Liu, H. Guo, M. Jin and B.F. Guo	355
<b>Silicon Float Zone Single Crystal Automatic Growth</b> L.H. Jin, Y.T. Wang, H.P. Shen, J. Liu, C.G. Yang, Y.J. Wang and J.X. Chen	361
<b>Experimental Study on Nitrogen-Spray Water Quenching for 9SiCr</b> B.D. Shao, L.F. Wang, H.M. Cheng, R.J. Wang, J.Y. Li, Z.L. Li, L.J. Hou, J. Hou, C. Tian and D.F. Ding	365
<b>Nanostructure-Dendrite Ti<sub>44</sub>Cu<sub>46</sub>Co<sub>4</sub>Zr<sub>6</sub> Composite with Excellent Mechanical Properties</b> X.F. Zhang, X.Q. Guo, C.Y. Gao and Z.Q. Jiang	369
<b>Influence of SiC Whisker on Formation and Oxidation Resistance of Coating for C/C Composite</b> Y. Chen, C.G. Wang and W. Zhao	373
<b>Preparation and Tribological Behavior of Carbon Fiber Reinforced Pantograph Slide Plate</b> H. Yuan, C.G. Wang, W.B. Lu and S. Zhang	378
<b>Study on Finite Element Model of Pneumatic Artificial Muscle</b> K.J. Zang, Y. Ma, N. Sun, Z.K. Niu, X.C. Gui and X.P. Hu	383
<b>The Dynamics of Pin Gear Drive Drum Mixer</b> S.H. Wan and M.H. Bai	387
<b>Raman Band Redshifting of <math>\alpha</math>-Cu<sub>2</sub>(OH)<sub>3</sub>Cl with Decreasing the Temperature</b> X.D. Liu, X.L. Xu, D.D. Meng, M. Fujihala, X.G. Zheng, Z.W. Chen and Q.X. Guo	391
<b>Optimization of Removal Conditions of Soluble Reactive Dyes from Aqueous Solutions by <i>Bacillus sp.</i> Biomass</b> G.X. Fang and L.H. Chen	395
<b>Research on the Reaction of IPDI and PPG with Organo-Tin Mixed Catalyst</b> Y. Wei, S.L. An and S.R. Liao	399
<b>Simulation of near-Crack-Tip Strain Fields on Single-Crystal Silicon Wafer</b> J.J. Li, C.W. Zhao, Y.M. Xing, Z.Y. Lv and Y.G. Du	404
<b>Construction Optimization of the Bridge-Tunnel Sections</b> W.L. Chao and X.H. Wang	408
<b>Chitosan Metal Complex: An Artificial Metalloprotease Hydrolyzing Trypsin Inhibitor from Soybean</b> P. Liang, D.F. Wang, X.Y. Wang, M. Ding, L. Zhang and Y. Xu	414

<b>Surface Morphology and Roughness of Cu Thin Films Prepared by Ionized Cluster Beam Deposition</b>	
B. Cao, T.R. Yang, G.P. Li, S.J. Cho and H. Kim	419
<b>Improved Physical and Electrochemical Hydrogen Storage Kinetics of the As-Spun Mg<sub>2</sub>Ni-Type Alloys by Substituting Ni with M (M=Co, Cu)</b>	
Y.H. Zhang, B.W. Li, H.P. Ren, Z.G. Pang, Z.H. Hou and D.L. Zhao	423
<b>The Study of Steel Channel's Cold Bending Forming Process through Numerical Simulation</b>	
L. Chen, Z.Y. Zhang and Y. Wang	429
<b>Research on Hardening Mechanism of Cement-Emulsified Asphalt-Epoxy Resin</b>	
F. Shen, S.L. Huang, Z. Sun and Q.J. Ding	434
<b>Antimicrobial Activity of Essential Oil from <i>Pinus yunnanensis Franch.var tenuifolia</i> Growing in China</b>	
Y.H. Tian, Z. Li, S.H. Wu and Q. Huang	438
<b>Synthesis of Superabsorbent Polymer in Inverse Emulsion via Post-Cross-Linking</b>	
Y.F. Cao, K. Liu, Z.L. Liu, F.Z. Tan and Y. Li	443
<b>Application of Fractal Theory in Electro-Discharge Dressing Diamond Grinding Wheel</b>	
L.R. Cai, Y. Li and M. Li	449
<b>A Study on Cu and Nb Precipitation during High Temperature Tempering in Low Carbon Steels</b>	
H. Guo, X.R. Sun, S.W. Yang, X.M. Wang and C.J. Shang	453
<b>Oxidation Kinetics of Superplastic Stainless Steel</b>	
W.H. Cho and H.S. Lee	458
<b>Influence of KF Concentration on Thickness and Energy Consumption of Micro-Arc Oxidation Coatings on LY12 Aluminum Alloy Substrate</b>	
J. Chen, J.Y. Xu, J.C. Zhao, C. Gao and G. Wang	462
<b>Retaining Structure Design and Residential Energy-Saving Research</b>	
J.Z. Huang and J.H. Wang	466
<b>A Particle Swarm Optimization Algorithm for Minimizing Weight of the Composite Box Structure</b>	
P.Y. Jiang, Z.M. Lin, J. Xu and J.Q. Sun	470
<b>Synthesis of a Novel Double Crosslinking Amphoteric Cassava Starch</b>	
H.Q. Lv, H.P. Li, G.W. Bai, H. Ou, Y.Z. Yang and Y. Zhang	476
<b>Effect of Substrate Temperature on High Rate Deposited ZnO:Al Films by Magnetron Sputtering</b>	
W.M. Li and H.Y. Hao	480
<b>Study on the Residual Compressive Strength of a Composite Sandwich Panel with Foam Core after Low Velocity Impact</b>	
Z.H. Xie, J. Tian, J. Zhao and W. Li	484
<b>Study on the Catalytic Activity of Graphene Oxide</b>	
Y.Q. He, N.N. Zhang, Y. Long, H. Sun, H.X. Qiu and J.P. Gao	488
<b>Research on the Straightening Deformation Process of the Residual Stress of the Numerical Simulation for Different Kinds of Heavy Rail</b>	
Y.Y. Liu, H. Li and L. Chen	492
<b>Synthesis and Characterization of Poly(butylenes succinate) with Control Different End-Group</b>	
C.N. Cui and J.T. Huang	497
<b>The Microstructure Transformation of 10CrMo910 Steel after Running 147000h in High Temperature</b>	
Z.W. Wang, T. Song, W. Mei and C. Wan	501
<b>A Comparative Study on Wood Properties of Teaks from Different Geographical Provenances</b>	
P.X. Peng, K.F. Li, K.N. Liang and K.M. Xu	508
<b>Inversion Behavior for Cylindrical Tubes under Axial Compression</b>	
D.H. Chen and L. Yang	512
<b>Solidification Simulation of Large Flat Ingot in Different Intensive Cooling Conditions</b>	
N. Lv, S.L. Li, Y.L. Jin, X.G. Ai and D.W. Zhang	517
<b>Preparation of Cordierite–Mullite Composite Crucibles and Structure Characterization</b>	
F.F. Li, J. Du, M.X. Zhang, W.C. Yang and Y. Shen	521

<b>Study on Simulation Experiment with Universal Pass Rolling Deformation for Heavy Rail</b> L. Chen and K.X. Bi	525
<b>The Research of Collaborative Navigation Localization Based on GPS and INS Integrated System</b> Y. Liu, J. Li, L.L. Li, Y.L. Lu and Z. Fang	530
<b>Biomimetic Aligned Porous Materials Made from Natural Biopolymers by UFDM</b> Y.Q. He, Z. Pan, F.B. Xing and Y. Liu	535
<b>An Experimental Study on Elevated Temperature Biaxial Bulge Test</b> H.S. Lee, J.H. Yoon and J.T. Yoo	539
<b>The Traits of Two-Directional Orthogonal Multivariate Small-Wave Packages with Finite Support</b> Z.Y. Chen	543
<b>Simulation of the Structure and Properties of Room Temperature Molten Salts 1-Ethyl-3-Methyl-Imidazolium Chloride/Chloroaluminate</b> G.C. Tian, D. Wang and Y.D. Li	547
<b>Effects of Semi-Solid Isothermal Treatments on Microstructures of Quasicrystal Reinforced AZ91 Alloys</b> Z.M. Liu, X. Wang, Y.B. Zhang and H. Gao	551
<b>Effect of Sintering Temperature on Microstructure and Performance of Ti(C,N)-Based Cermets</b> L.Y. Zou, Z.P. Sun and G.J. Zhang	556
<b>The Effect of Pre-Strain on the Bake Hardening Property for Ultra-Low Carbon Steel</b> L. Jin, W.J. Li, X. Dong and J. Hou	561
<b>Local Laser Heating Effect on Raman Spectroscopy of <math>\beta</math>-Co<sub>2</sub>(OH)<sub>3</sub>Br</b> X.D. Liu, J. Lu, M. Fujihala, D.D. Meng, X.L. Xu, X.G. Zheng, Z.W. Chen and Q.X. Guo	566
<b>Synthesis of a New Platinum Acetylide Polymer with a Pyrimidine Moiety for Organic Solar Cells</b> L. Li, X.X. Sun, Y. Hu and Q.H. Wu	570
<b>Research on Properties of RE-7075 Al Alloy's Hot Rolled</b> J.H. Zhong, H.B. Zhu, K. Feng and Y.P. Xiao	574
<b>Preparation of Porous ZnO Film by Zinc Oxalate Recurrence Method</b> Y.Q. He, R.G. Huang, Y. Liu and F.B. Xing	578
<b>Preparation and Binding Characteristics of Molecularly Imprinted Polymers for Capsaicin</b> J. Sun, N. Peng, W.X. Ao and X.S. Huang	582
<b>Experimental Research on Wave-Absorbing Properties of Pumice Lightweight Aggregate Concrete</b> X.J. Lv, M.L. Cao, Y. Li and Y. Li	586
<b>The Effect of Ultrasonic Etching on the Structure of Stabilized PAN Fibers</b> X.Y. Hu, C.G. Wang, Q.F. Wang, W.B. Lu and M.J. Yu	592
<b>The Influence of Specific Pressure on the Organization and Properties in Liquid Forging</b> C. Li, J.X. Wang and H.Q. Miao	598
<b>Mixed Proportion Design of Lightweight Concrete Using the Sludge Kilned Coarse Aggregate from Reservoir</b> H.C. Yang, J.P. Wang and J.W. Wu	602
<b>Microstructure and Properties of ZcuSn3Zn8Pb6NiFeCo Alloy</b> Q.S. Wang, Z.F. Song, Z.Q. Feng and Z.D. Wang	609
<b>Study on Fatigue Resistance Performance of Flexible Fiber and Rigid Fiber Reinforced Concrete</b> K. Liu, Y.M. Wang, W.W. Yang and Y. Sun	619
<b>Research on Dielectric Spectrum Characteristics of Nano Fe<sub>3</sub>O<sub>4</sub> Modified LDPE</b> D. Zhang, W. Song, Z. Sun, B. Han and Q.Q. Lei	623
<b>Synthesis and Field Emission Properties of Electroless Nickel Deposition on Carbon Fibers</b> L. Yang, Z.J. Ke, Y. Ye and T.L. Guo	627
<b>The Effects of Sputtering Pressure on the Properties of Carbon Counter Electrodes for Dye-Sensitized Solar Cells</b> S.H. Liu, G.S. Liu, X.Y. Shen and Z.Q. Hu	631
<b>Evaluation on Chloride Cracking of S135 High-Strength Drill Pipe</b> Z. Zhi, X.Y. Zhou, D.Z. Zeng, J.Y. Zhang and T.H. Shi	636

<b>Analysis of Elastic Moduli and Fracture of Concrete with Nature Element Method in Mesoscale</b>	
H.C. Qu, B.Y. Zhang and F. Zhang	640
<b>Preparation and Characterization of MicroPCMsContaining Paraffin</b>	
D.W. Huang, Y. Lian and H.M. Wang	647
<b>Numerical Simulation of Spraying and Jointing for Polyurea Spraying Gun</b>	
B. Li, J. Zhao, Y. Sun, B.H. Li and M.Y. Tan	651
<b>Shape-Controlled Pd Nanoparticles in the Mixed Surfactants by Ultrasonic Irradiation</b>	
Y.L. Wang, M.X. Zhang and D.X. Tan	655
<b>Prediction of Cutting Consumption Based on Optimization-Making RBF Artificial Neural Network</b>	
M.Q. Gong, M.W. Sun, M. Huang and S.W. Xiang	659
<b>Model and Analysis of Flexural Properties of Al<sub>2</sub>O<sub>3</sub> Ceramic Prepared by Centrifugal Slip Casting Using BP Neural Network Model</b>	
J.Y. Yu, Q. Li and X.D. Sun	664
<b>Strip Casting of Al-25%Si Alloy</b>	
T. Haga, H. Harada, S. Kumai and H. Watari	669
<b>Construction of a Museum: An Example of Cultural Education</b>	
C.Y. Wu, H.Y. Huang and M.C. Huang	673
<b>Controlled Drug Release from Biodegradable Bone Fillers</b>	
Y.L. Zhang, C. Xu, Z.M. Sun, M.C. Yi, Y. Liu, J.P. Gao and J. Yan	677
<b>Effects of Mn Addition and Addition Sequence on Carbon Inoculation of Mg-3%Al Alloy</b>	
J. Du, M.H. Wang and W.F. Li	681
<b>Effect of Ultra High Molecular Weight Polyacrylonitrile (UHMW-PAN) on the Rheological Behavior of PAN/DMSO Solution</b>	
H.Y. Jiang, Q.Q. Yin, M.H. Zhou and D. Pan	687
<b>Influences of Pressure Conditions on Synthesis of Mg(Zr<sub>0.05</sub>Ti<sub>0.95</sub>)O<sub>3</sub> Dielectric Ceramics</b>	
C.F. Tseng, C.H. Hsu, C.J. Huang and C.H. Lai	692
<b>Theory Analysis of Biomass Molding Mould</b>	
S.Y. Wang, Z.M. Wang, G.X. Zuo, W.R. Zhang and J. Zhao	696
<b>Development of Various Business Incubation Parks</b>	
L.N. Zheng and T.J. Pan	701
<b>Investigation on <i>In Situ</i> Tensile of Extruded 1420 Al-Li Alloy</b>	
Z.W. Chen, J. Zhao, S.S. Li and J.Z. Zou	705

## Chapter 2: Manufacturing and Design Science

<b>Effect of Isothermal Holding in Solid-Liquid Phase Region on Mg<sub>2</sub>Si Morphology in Hypereutectic Al-Si <i>In Situ</i> Composite</b>	
Z. Liu, H.B. Xu, K. Cao and M.Y. Huang	711
<b>Physical Simulation of the Cutting Process Induced by Tool Geometric Angle and Cutting Parameters</b>	
X.H. Wang, P. Zhou, Y.W. Liu and M.J. Dai	715
<b>Oa-Based Workflow Process Design and Implementation of Approval Procedures</b>	
J.T. Yang, Z.H. Xia, G.F. Li, J.H. Shi and W. Chen	719
<b>Effect of Annealing Temperature on Phosphorus Segregation at Grain Boundary in a Ti-IF Steel</b>	
X.L. Song, Z.X. Yuan, J. Jia, L.X. Fan, K. Peng, M. Li and P.H. Li	724
<b>Preparation and Properties of Sulfonated <math>\beta</math>-Cyclodextrins Used as Water-Reducer</b>	
S.H. Lv, R.J. Gao and D. Li	729
<b>Discussion on the Sustainable Development of Urban Water Conservancy Infrastructure Construction</b>	
C.J. Ma, G.L. Cao and Y.T. Ma	733
<b>Solving the Job Shop Scheduling Problem Using the Imperialist Competitive Algorithm</b>	
J. Zhang, P. Zhang, J.X. Yang and Y. Huang	737
<b>A Novel Rigid Vacuum Insulation Panel: Vacuum Insulation Sandwich</b>	
J. Zhang, Z.F. Chen, J.M. Zhou, B.B. Li and Z. Chen	741

---

<b>Temperature Field of Doublet-Wells Aquifer Thermal Energy Storage in Sanhejian Coal Mine</b>	
Y. Zhang and D.M. Guo	746
<b>Simulation Study on the Fluid-Solid Coupled Heat Transfer of Cylinder Head</b>	
M.Y. Zhang, L. Li and M. Yan	750
<b>Research on Contact Deformation and Influencing Factor of Ball Screw</b>	
Y.S. Wang, M.M. Wang and M. Yan	755
<b>Methods of Improving Part Accuracy during Rapid Prototyping</b>	
A.H. Peng	760
<b>Study on the Stability of Alkaline Silica Sol</b>	
J. Wang, Y.Y. Huang, R. Wang, M. Sun and Y.L. Liu	764
<b>Primary Understanding on the Issue of the Hainan Provincial Environmental Geology</b>	
H. Wei, Y.Y. Liu, X.B. Xia and H.L. Liu	768
<b>A New State Estimator of PMSM Using Adaptive Extended Kalman Filter</b>	
X.Z. Ding, C.R. Zhang, L.H. Yu and H.X. Li	772
<b>Parameters Study on Generation of Uniform Copper Droplet by Pneumatic Drop-on-Demand Technology</b>	
S.Y. Zhong, L.H. Qi, J. Luo and Y. Xiao	781
<b>An Analysis of the Evolution in Internet of Things Industry Based on Industry Life Cycle Theory</b>	
H.S. Qiao and G.L. Wang	785
<b>Fabrication of Aluminiferous Nanofibers by Simple Hydrolysis of Nanosized Al/AlN Powder</b>	
G.H. Liu and S.Y. Du	790
<b>Preparation of TiO<sub>2</sub>-HZSM-5 Composite Used for Removal of Active Brilliant Red X-3B</b>	
W.J. Zhang, Q. Li and H.B. He	795
<b>Application of Asymmetric Eigenvalue Method for Dynamic Analysis of Aqueducts</b>	
Y. Yang, J.M. Ren and D.Z. Liu	799
<b>Air Base Damage Evaluation Using Cloud Barycenter Evaluation Method</b>	
C. Zhang, Q. Shi and T.L. Liu	803
<b>Mold Cavity Surface Subdivision Method Based on Fuzzy Clustering for Edge Detection</b>	
Z.X. Feng, Y.S. Zhai and D.H. Miao	808
<b>Soil Pollution Investigation of Chromium Slag Contaminated Site</b>	
Z.L. Wang, H.Z. Zhang, Y.P. Wang and W.H. Yu	812
<b>Microstructure Evolution of Nb Containing Steel during Simulated Hot Charging</b>	
J. Li, Q. Wang and Y.J. Lu	816
<b>Power Optimal Utilization of DC Bus Micro-Grid System</b>	
Y. Zhao, R.Q. Cheng, G.S. Zhao and Z.H. Zha	820
<b>Numerical Simulation of Temperature Field of Biomass Briquetting Based on ANSYS</b>	
L. Xing, X.D. Liu and W. Lu	824
<b>Topology Optimization Design of High Pressure Storage Tank Structure</b>	
Q.S. Ma, Y. Cai and D.X. Tian	828
<b>The History, Classes and Presentations of Groups</b>	
X.Q. Guo and Z.J. He	834
<b>Study on Reproduction of Color Information of Digital Image Based on Different Color Gamut</b>	
W.G. Chen	838
<b>Research on Wear and Life Prediction of Hobbing Cutter in Cryogenic Cutting with MQL</b>	
X.H. Zhang, C. Xia, P. Chen and G.F. Yin	842
<b>Improved Delay-Dependent Robust Stability Criteria for Discrete-Time Stochastic Uncertain Networks with Time-Varying Delays</b>	
M.Z. Luo and S.M. Zhong	849
<b>Effect of Combined Chitosan Coating and Modified Atmosphere Packaging on the Storability of Cold-Stored Rice Field Eel (<i>Monopterus albus</i>) Fillets</b>	
S.L. Li, X.M. Chen and X.R. Zhao	853
<b>Burnishing and Electrofinishing in Screw Surface Polishing</b>	
P.S. Pa	857
<b>Evaluation of Cooling Wall System and Phenolic Resin as Thermal Barrier in Buildings</b>	
W.P. Sung, T.Y. Chen and M.H. Shih	861

---

<b>The Modification of Mechanical Properties of Changbai Mountain Smell Pine Used by Floor</b>	
X.Y. Niu, Y.W. Bai and X. Wang	866
<b>The Design and Implementation of Tamper Resistant Grading Function in the Science and Technology Awarding Review System</b>	
C.X. Hu, X.X. Liu and X.N. Ma	869
<b>Recovery of Mesoporous Silica from Waste Rice Husk Ash of Biomass Energy Industry</b>	
W.J. Zhu, Y. Zhou, W.H. Ma, M.M. Li, J. Yu and K.Q. Xie	873
<b>The Mechanism Research of Forming Belt of Belt Insulation Board Machine</b>	
J. Sun and T. Xu	877
<b>The Applications of Vibratory Stress Relief in High-Strength Aluminum Alloy Thick Plate</b>	
C.J. Gan and K. Liao	881
<b>Application of Frequency Conversion in Preparation of Semisolid A356 Alloy Slurry</b>	
Z. Liu, F.Y. Wang, K. Cao, H.B. Xu and M.Y. Huang	886
<b>Effect of Exopolysaccharide Producing Lactic Acid Bacterial on the Gelation and Texture Properties of Yogurt</b>	
S. Zhang and L.W. Zhang	890
<b>Morphology and Structure Properties of PEG-<i>b</i>-PBT, PEG-<i>b</i>-PBT-HA Nanofibers Based Gas-Electrospun</b>	
X.Z. Yang, Z.S. Li, J.N. Gao and L.L. Zhang	894
<b>Comparison of Detection Methods of Pore Characteristic of Inkjet Paper Coating</b>	
J.L. Tai, G.X. Chen, Q.F. Chen and B.L. Tang	898
<b>Hybrid Ant Colony Algorithm for Job Shop Schedule with Unrelated Parallel Machines</b>	
J. Zhang and G.B. Liu	905
<b>Effect of Glass Fiber Modification on Tensile Strength and Shrinkage of Ceramic Mould</b>	
Z. Wang, D.H. Lu, H. Gong and X.G. He	909
<b>Spinning Technics Research of St.Ma/Polyester Blended Hard Twist Slub Yarn</b>	
L. Chen, D.F. Yi, Y.L. Zhai and Y.L. Gu	913
<b>Preparation of Al<sub>2</sub>O<sub>3</sub>-Supported Ni Catalyst and its Catalytic Hydrogenation Performance</b>	
W. Liu, X.L. Chen, J. Yang, Y. Li, Y.F. Zhou, Z.L. Huang and Z.Z. Yi	917
<b>A General Approach for Automatically Constructing CAD Models of Human Teeth</b>	
Q. Li and C.A. Rubin	921
<b>Study on Consumables of Ink-Jet Printing in Producing PCB</b>	
M.H. Liao	925
<b>Gas Phase Phosphorus Heavily-Doped FZ Silicon Thermal Field Design and Growth Method</b>	
X.N. Zhang, J.H. Li, Y.T. Wang, C.X. Zhang, C.G. Yang, H.P. Shen and J.H. Wang	929
<b>Applications of Nanomaterials in Acupuncture and Moxibustion Instrument and Materials</b>	
Y.X. Xu, C. Jiang and G.Z. Chen	933
<b>Synthesis and Characterization of LiFePO<sub>4</sub> Prepared by Sol-Gel Technique</b>	
H. Wang, Y.L. Ruan and Z.C. Shi	937
<b>Removal of Se(VI) from Raw Water by Ion Exchange Process</b>	
Y.S. Shi, Y.Z. Shi and L. Wang	941
<b>Mechanism of Mandrel on Thickness and Profile of Parts by Shear Spinning</b>	
M. Zhan, Y.T. Qin, F. Chen, H.B. Jiang, J. Wu and H. Yang	949
<b>The Relationship between Characteristics and Shear Strength of Structural Planes and its Effect on the Stability of Landslide</b>	
H. Wei and J. Yi	956
<b>Preparation and Characterization of Microcapsules for Self-Healing Material</b>	
W.P. Ma, W. Zhang, Y. Zhao, L.P. Liao and S.J. Wang	960
<b>Precipitation Behavior of Cd in Al-5wt.%Cu Based Alloy during Solidification</b>	
M. Li, L.R. Cai and Z.D. Qu	964
<b>The <i>In Situ</i> Shear Strength of Roller Compacted Concrete in the Dam of Jinghong Hydropower Station</b>	
J.B. Xie, J. Fan, T.C. He and C.F. Tang	968
<b>Preparation and Slow-Release Properties of Clay-Based Phosphatic Fertilizers</b>	
J.T. Yang, G.X. Pan and B. Cheng	974

<b>Effect of Sintering Temperature on Microstructure and Properties of VC/Fe Composite</b> G.J. Zhang, Z.P. Sun and L.Y. Zou	978
<b>Characterization of Casting Defects in Aluminium Alloys</b> G. Wu, K. O'Reilly and M. Galano	984
<b>Research on the Quenching Medium Recycling Technology Based on a Melting-Solution Confluence Method</b> L.D. Chen, C.Z. Fu, Y.J. Li, L.Z. Feng and Y.X. Fu	988
<b>Experimental Research on the Quantitative Characterizations of Elasticity and Viscosity of Polyacrylamide Solution</b> H.F. Xia, J.R. Zhang, W.G. Ma, X.N. Li and Q.Y. Yang	992
<b>Research on China's Electronics Listed Company's Financial Risk Probability and Statistics</b> S.B. Yan and W.Q. Zhu	996
<b>Research on Competitiveness Difference of Economic Cooperation Harbor City in Beibu Gulf Rim Based on the Grey Relation Comprehensive Evaluation</b> H.F. Zhang, Y. Chen and J.P. Pei	1000
<b>Preparation and Photocatalysis Properties of TiO<sub>2</sub>/Graphene Nanocomposites</b> D.F. Wang, D. Chen, G.X. Ping, C. Wang, H.Z. Chen and K.Y. Shu	1005
<b>Study on Construction Technique of Complex Multi-Layer Steel Structure</b> S.P. Zheng and X. Chen	1009
<b>Structure Design and Interference Analysis of Walking Aids</b> J.X. Zhang, S.S. Cao and W.W. Wang	1014
<b>Photocatalytic Degradation of ABR X-3B on TiO<sub>2</sub>-HZSM-5 Composite</b> W.J. Zhang, Q. Li and H.B. He	1019
<b>Preparation of Epoxy/PEG Shape-Stabilized Phase Change Materials by <i>In Situ</i> Reactive Blending</b> C.S. Zhao, N. Li, L.Y. Wu and J.M. Chen	1023
<b>Graphene Oxide Containing Composite Hydrogel Fabricated by Freeze/Thaw Method</b> W.C. Wang, Z.L. Li, J.J. Wu, M.C. Yi, Y. Liu, J.P. Gao, W. Wang and J. Yan	1028
<b>Performance of Reactive Plasma Cladding TiC Particle Reinforced High Chromium Fe-Based Ceramics Composite Coating</b> L.M. Wang	1032
<b>Extraction Optimization of Antibacterial Substances from <i>Amomum tsao-ko</i></b> W.X. Chen, M.F. Peng, Y.Y. Hu and H.Y. Qiu	1036
<b>Preparation of Nano-TiO<sub>2</sub> and Performance Study on Photocatalytic Degradation of Methylene Blue</b> J. Liu, Z.X. Ma and S. Liang	1040
<b>HZSM-5 Zeolite Modified by Oxalic Acid and Photocatalytic Activity of Supported TiO<sub>2</sub></b> W.J. Zhang, M.L. Hu and H.B. He	1044
<b>Photocatalytic Degradation Glyphosate with Cerium and Nitrogen Co-Doped TiO<sub>2</sub> under Visible Irradiation</b> L. Lin, X.J. Zhang, G.Q. Xiao and X. Xiong	1048
<b>To Discuss the New Century's Recessive Knowledge Management of Teachers in Senior Schools</b> J. Yang	1052
<b>Comparing Study on Real Drawbead and Equivalent Drawbead Based on Finite Element Analysis</b> X.G. Qiu and H. Huang	1056
<b>Investigation of Tube Drawing Process by Finite Element Simulation</b> Y.H. Li, J. Zhang, X.J. Liang, W.H. Shi and M. Kang	1060
<b>Experiment and Research on Mechanic Behavior of Concrete with Different Addition Amounts of Polypropylene Fibers</b> Y.Z. Chen, W.H. Xuan and X.H. Chen	1064
<b>A Novel Approach to Mine Knowledge from Social Images</b> F.C. Wang	1068
<b>Finite Element Modal Analysis of the Frame of Corn Stubble-Collector</b> J. Tong, B.G. Zeng, D.H. Chen, L.Z. Quan and S.J. Zhang	1072
<b>Starch/SBR Biocomposites Prepared by Solid Blend Method: Effect of Surface Modification and Coupling Agent</b> M.C. Li, X. Ge, J.H. Lim, M.S. Kim and U.R. Cho	1076

---

<b>Comparison and Analysis of Two Auditory Models Faced to Mechanical Faults Diagnosis</b> Y.G. Li and J.P. Zhang	1081
<b>Design and Analysis of the Digging Spring Tooth of Stubble Harvester</b> D.W. Shao, J.F. Wang, D.H. Jiang and G.F. Wu	1087
<b>Research of Telecommunications Access Pricing Based on Evolutionary Game Theory</b> N. Li	1091
<b>Asymmetric Information, Heterogeneous Belief and Risky Asset Pricing</b> X.Q. Yu and S.C. Liu	1095
<b>Application of Random Medium Model in Analyzing Surface Settlement Caused by Pit Excavation</b> G.M. Yin, H.L. Fu, Y.W. He and D.R. Ouyang	1099
<b>A Design of Intelligent Family Network Based on Distributed Control System</b> L.H. Mei	1103
<b>Influence of Process Parameters on the Deep Cup-Drawing Process by Simulation</b> X.B. Zhang and X.H. Jiang	1107
<b>Design of 3D Pattern on Jacquard Fabric Based on Digital Jacquard</b> X.H. Zhu, Y.H. Xu, L. Du and Y. Xie	1111
<b>The Study on the Flocculation Effect of Modified Collagen Protein Cationic Flocculent on Waste Drilling Fluid</b> S. Zhang, X.C. Wang, L. Zhou and T.T. Qiang	1115
<b>Research Progress of SiO<sub>2</sub> Matrix Composite Materials for Radomes</b> X.X. Li, Y. Sun, J.L. Li and M. Ma	1119
<b>Magnetic Properties of Sm-Fe-N Prepared by Melt-Spun in Liquid N<sub>2</sub> and High Gas Pressure Nitrogenation</b> W. Jiang, P.Z. Si, H.X. Wang, J.G. Lee, C.J. Choi, J.J. Liu, M. Zhong, Z.F. Li and H.L. Ge	1123
<b>Ultrasonic Sector Scanning Method in the Application of the Accurate Determination of the Concrete Bored Pile Defect Position</b> D.Z. Liu, J.M. Ren and Y. Yang	1128
<b>Application of Pre-Grouting Technique in Yellow River Crossing Tunnel in Eastern Route of South to North Water Transfer Project</b> X.Y. Wang, S.W. Duan, X.E. Xu and H.L. Wang	1133
<b>Wear Properties of Saw in Granite Cutting Process by Plasma Arc Heating</b> B.B. Xiao, Z.Y. Zhao and J.G. Yang	1137
<b>Analysis of Quality Accidents Arising from Common Interactions in Projects</b> J.W. Li and X.P. Zhu	1141
<b>Theoretical Derivation of the Column (Ball) Expansion in Pressure Grouting</b> P. Wu, H.L. Fu, Y.W. He and X.Z. Zhu	1147
<b>New Ajax Post Method for Multi-Field Data Including Rich Text</b> C.J. Gan and Y. Zhou	1151
<b>Real-Time Visual Analyses on Failure Criteria of Slope Stability in Strength Reduction Finite Element Method</b> R.J. Li, W. Zheng, J.D. Liu and T. Xie	1155
<b>A Research on Environmental Issues Applied to the Hotel Industry</b> Y.F. Yue	1159
<b>The Application of PCA and SVM in Rolling Bearing Fault Diagnosis</b> M. Li	1163
<b>Hardware Design of Ultrasonic Ranging System in Agricultural Robot</b> F. Zhang and S.L. Fu	1167
<b>Research of the Admixture Influence Cement Stabilized Macadam Vibrating Compaction Effect</b> Y.Y. Liu, J.J. Li and Y. Fu	1171
<b>Prediction Algorithm of Spectral Reflectance of Spot Color Ink Based on Color Parallel and Superposition Model</b> C.R. Lin, J.F. Xu and J.L. Xu	1176
<b>Stock Issue Price and the Entrepreneur's Information Manipulation</b> X.Q. Yu and S.C. Liu	1183
<b>Application of DSM Topological Sort Method in Business Process</b> H.L. Yuan and D.W. Wang	1188

---

<b>Sustainable Development Theory of the Natural Step Applying Research in China Manufacturing Industry</b> X.Y. Tang, W.C. Yang, L.L. Yang, S.Q. Li and H. Li	1192
<b>Research on Emission Control of Marine Diesel Engine</b> G.J. Chen, Z.M. Liu, T.T. Liu, S.H. Su, G.J. Yuan and Y.J. Cao	1198
<b>Designment Algorithm on Orthogonal Two-Directional Vector-Valued Wavelets with Three-Scale Dilation Factor</b> J.T. Zhao	1203
<b>Study on Synthesis and Application of Superplasticizer from Chitosan</b> S.H. Lv, J.P. Duan, R.J. Gao and Q. Cao	1207
<b>A Modified Dual-Wavelength Matrix Calculation Method for Fiber Bragg Grating (FBG)</b> X. Liu	1211
<b>The New Development and Application of Optical Sensor</b> B.C. Wang and P. Wang	1215
<b>Oak Veneer Bleaching Technology</b> D.J. Shen	1219
<b>Microstructure and Recrystallization Texture Characterization of Cold-Rolled Dual-Phase Steel</b> Z.G. Wang, Z.Z. Zhao, A.M. Zhao and J.Y. Ye	1223
<b>Study on Feasibility and Accuracy of Stress Test</b> C.J. Gan and K. Liao	1227
<b>The Research of Self-Organizing Maps Based on Document Collections</b> Y. Ding and X. Fu	1232
<b>Study on the Degradable Mulch Sheet Papermaking Technique</b> Y.J. Gao, H.J. Liu and M. Li	1236
<b>Characteristics of Wall Thickness Increase in Pipe Reduction Process Using Planetary Rolls</b> Y. Kotani, S. Kanai and H. Watari	1241
<b>The Communication Feedback Creates a Two-Winner ~ Cognitive Model for Explaining Client-Architect Interaction</b> M.L. Huang and Y.Y. Wang	1248
<b>Experiment Study on Treatment of Chromium(VI)-Containing Groundwater by Modified Synthetic Zeolite</b> Y.J. Huang and H.Z. Zhang	1253
<b>Raman Spectral Properties of <math>\beta</math>-Co<sub>2</sub>(OH)<sub>3</sub>Cl down to the Liquid Nitrogen Temperature</b> J. Lu, X.D. Liu, X.L. Xu, M. Fujihala, D.D. Meng, X.G. Zheng, Z.W. Chen and Q.X. Guo	1257
<b>Researching and Production Technology of Golden Yellow Microcrystalline Glass</b> S.P. Zheng, X. Chen and B.H. Zhao	1261
<b>The Applications of Group Theory</b> X.Q. Guo and Z.J. He	1265
<b>The Morphologies of Nano Carbon Growing <i>In Situ</i> by Catalytic Chemical Vapor Deposition</b> X.F. Xu, Y.Y. Hu and P. Xiao	1269
<b>Research on Main-Line Voltage Fluctuation of Z-Source Inverter</b> R.Q. Cheng, Y. Zhao, G.S. Zhao and Z.H. Zha	1273
<b>Control Strategy of Microgrid Based on Distributed Generation</b> Y. Zhao, R.Q. Cheng, X. Gong and G.S. Zhao	1277
<b>Application of GIS in Internal and External Integration of Land Alteration Survey Technology</b> L.F. Lai and Y.F. Zhang	1281
<b>Numerical Simulation of Rubber Bladder Hydroforming Process for Shrink Flanging Parts with Large Curvature</b> M.H. Chen, F.D. Wang and J. Xiong	1286
<b>White Cloud or Black Cloud: Opportunity and Challenge of Spectrum Sharing on Cloud Computing</b> L.X. Liu, G. Hu, Z. Huang and Y.X. Peng	1290
<b>Flow Stress Behavior of Nanometric Al<sub>2</sub>O<sub>3</sub> Particulate Reinforced Al Alloy Composites Manufactured by Casting</b> Z.M. Zhang, Y.B. Yang and X. Zhang	1294

---

<b>A Novel Method to Compress Real-Time Process Data</b> X.J. Zheng	1298
<b>Finite Element Modeling of Deep Drawing of Coated Sheet</b> X.B. Zhang	1302
<b>A Optimization Model of Incentive Mechanism between Manufacturer and Dealer in Supply Chain</b> J.H. Yang and K. Niu	1306
<b>Numerical Simulation and Experiment Analysis of MIG Welding for Aluminum Alloy Extrusion</b> Z.Z. Luo and Y.S. Pan	1311
<b>Influence of an Anti-Chloride Corrosion Admixture on Density of Cement-Based Materials</b> W. Zhang, X. Yao and R. Mu	1315
<b>Effective Pre-Stress Identification for a Simply-Supported PRC Bridge Based on the Dynamic Response Induced by the Passing Vehicle</b> J.Q. Bu and H.Y. Wang	1320
<b>Research of Information Integration System Supporting for SMEs Rapid Product Development</b> J.Y. Wei and P.S. Zhong	1326
<b>Research on Strategies of Networked Manufacturing Resources Configuration Based on Evolutionary Game</b> Y. Zhan, J.S. Lu and X.H. Ji	1330
<b>Double Qualified Teachers' Training Strategies and Approaches</b> X.P. Chen	1335
<b>Production Process and Nondestructive Testing of Soybean Stalks Particleboard</b> W. Lu, J. Yao, P. Han, W.J. Wu and C. Liu	1339
<b>Ultrafine Glass Fiber Core Material Produced by Wet Method</b> T.Z. Xu, Z.F. Chen, J.M. Zhou, X.Y. Cheng, W.P. Wu and Z. Chen	1343
<b>A Modified MPPT Method for Photovoltaic System</b> Y.S. Huang, Y.J. Wei and X. Chen	1348
<b>The Fast Design and the Optimization of the Injection Mold Based on CAD and CAE Technology</b> H. Tan, Z. Wang, G.H. Dai, X.X. Chen and J.F. Zhu	1352
<b>"Double Teachers" Connotation Standards</b> X.P. Chen	1357
<b>A Facile Synthesis of Carbon Nanobelts over Mo/Fe/MgO Catalysts</b> Y.N. Xiong, X.H. Chen, Z. Yang and L.S. Xu	1361
<b>Briefly Analyse Nowadays College Students' Psychological Health</b> J. Yang	1365
<b>Analysis on the Ultimate Pullout Force of Prestressed Cable Based on Nonlinear Mohr Strength Criterion</b> X.Y. Luo and W.P. Liu	1369
<b>Study on Preparation and Anodic Oxidation of Gradient Porous NiTi Alloy</b> Q. Li, J.Y. Yu and X.D. Sun	1373
<b>The Optimum Design on the Roller Chain Drive of the Machine for Supplementing the Traditional Chinese Pills</b> D.H. Jiang, D.W. Shao and J.Y. Luan	1378
<b>Review and Prospect of Surface Modification of Kaolin</b> S.L. Ding, L.L. Zhang, B.H. Xu and Q.F. Liu	1382
<b>Study on the Safety of Mineral and Synthetic Oil Added Commonly Used Extreme Pressure Additives</b> Z.J. Chen, L.L. Feng, B.L. Li, J.J. Yue, Y.L. Wu and Z.N. Dai	1386
<b>Diseases Features and Treatment Measures of Expansive-Soil Channel Slope</b> X.X. Yang and J. Ren	1390
<b>Reservoir-Forming Conditions Analysis of Shale Gas in Lower Paleozoic of Chongqing Northeast</b> Y. Zhu, D.H. Li and L.J. Cheng	1395

**Chapter 3: Engineering Technology**

<b>Application of Oxygen-Releasing Material to Enhance <i>In Situ</i> Aerobic Bioremediation</b> T.Y. Chen, C.M. Kao, H.Y. Chiou, Y.T. Yu and W.P. Sung	1401
<b>Analysis of Tooth Surface Temperature Field and the Influencing Factors of Face Gear Driven</b> G.Q. He, H.Z. Yan, W. Hu and T.L. Shu	1405
<b>Study on the Effect of Salt Modulation upon the Maize Drying Process</b> J.X. Li, Y.Q. Zhang, W.F. Wu and C.S. Liu	1412
<b>Statistical Analysis on Accelerated Degradation Test Data Based on Multiple Performance Parameters</b> J. Pan, X.Y. Wang, W.H. Chen, S.W. Xu, P. Qian and H.J. Liu	1417
<b>The Fatigue Life Simulation of the Wheel of CHR3 EMU in Random Loading</b> J.W. Yang, Q.L. Shi, G.Y. Zhang and J. Zhang	1424
<b>Design of a Novel Heat Exchanger Using in Automobile Exhaust Thermoelectric Generator</b> R. Quan, X.F. Tang, S.H. Quan and J.G. Wang	1428
<b>Effect of Cold Energy Storage of Single-Well Aquifer Thermal Energy Storage in Sanhejian Coal Mine</b> Y. Zhang and D.M. Guo	1433
<b>Study on Dynamic Balance Weighting for Single-Disk Rotor System Based on Phase Difference Mapping</b> Q.L. Zhao, H.Q. Wang and J.J. Gao	1437
<b>Dynamic Stiffness Characteristics and Test of the Spindle of NC Machine Tool</b> X.L. Liu and J.X. Liu	1442
<b>Experimental Study on Seismic Behavior of Recycled Concrete Latticed Wall</b> J.H. Zhou, C.B. Zhang and X.H. Meng	1446
<b>Renewable Energy Technology in Construction Ecological Residence of New Villages</b> H.R. Dong	1450
<b>Inversion Analysis Based on the Unloading Rock Mass of Underground Powerhouse Monitoring Achievements of Jin Ping Cascade II Hydropower Station</b> J. Liu, J.L. Li, L. Xiao, S.W. Luo and J. Cai	1455
<b>The Application in Hydraulic Elevator System with the Secondary Element in the Network of Hydrostatic Transmission with Secondary Regulation</b> A.F. Wang, X.C. Liu and P. Zhou	1460
<b>Calculation Methods of Surrounding Rock Pressure for Small Clear Spacing Shallow Unsymmetrically Loading Tunnel</b> L.C. Wang, L.M. Peng and D.W. Zhou	1464
<b>Finite Element Model for Damage Detection in Three-Dimensional Cube Structures</b> W. Yan, W.C. Li and W. Wang	1468
<b>Development of Dedicated Controller for HVAC</b> J.M. Yang and Y. Lin	1472
<b>Using Iterated Local Search for Efficiently Packing Unequal Disks in a Larger Circle</b> W.Q. Huang, Z.Z. Zeng, R.C. Xu and Z.H. Fu	1477
<b>Analysis of Impact to Counter Force and Internal Force in Different Arrangements of Minor Radius Curve Steel Box Girder Supporting Point</b> Q.S. Sun and T. Wu	1482
<b>Experimental Study on Additive of the Foam Technology for Dust Control in Underground Coal Mines</b> W.X. Ren and Z.H. Kang	1486
<b>Remote Fault Diagnosis System for Water Cutter Based on GPRS</b> Y.Q. Wang, D.A. Zhao and B. Chen	1493
<b>The Application of Multi-Node Cable Element</b> X.Y. Sun and Z.Q. Wang	1498
<b>Assurance Technology of Testing Adequacy Based on Functional Analysis</b> J.Y. Wu, J. Tian and T.D. Zhao	1502
<b>Failure Analysis of Aircraft Aluminum Alloy Structures in Coastal Environments</b> B. Pan, T.M. Jiang, J.M. Jin and M.D. Ma	1509

---

<b>Time Study of Automatic Edgebanding Machine Using BP Artificial Network</b> J.X. Hao and W.J. Liu	1514
<b>Design of Hi-Power Continuously Adjustable Constant Current Source Based on UC3846</b> Y. Li, C.R. Zhang, M.X. Lin and Y.H. Li	1519
<b>The Modal Analysis of Full Mounted Converter Vessel Tilting Mechaism</b> Y.K. Gu, X.X. Tong and X.C. Luo	1524
<b>Research on Measuring and Controlling of Pose and Position Parameters for Roadheaders</b> J. Mao, H.L. Qi and M. Xie	1528
<b>Modeling Analysis and Simulation of Hydraulic Axial Piston Pump</b> M. Hao and X.Y. Qi	1532
<b>Design of a Digitalized Testing System for Simple Beam Charpy Impact Testing Machine</b> Y. Zheng, J.L. Wang, Y.W. Ye, J. Jiao, G. Wang, Y.G. Deng, S.M. Qin and Z.L. Peng	1536
<b>Assembly Model Based on Dynamic Transition Graph for Satellite General Assembly Process Planning</b> G. Sun, J.F. Yu and Y. Li	1542
<b>Sensitivity Analysis for Design Parameters of Cantilever Casting PC Box-Girder with Corrugated Steel Webs</b> K.B. Jiang, Y. Ding, Y.W. Liu, P. Wang and F. Zheng	1546
<b>Study on Application of Membrane Materials in Home Decoration Design</b> T.T. Yu and W.P. Hu	1551
<b>The Robustness Analysis of Mapping Process from Functional Domain to Physical Domain in Axiomatic Design for Product Design</b> X.F. Cheng	1554
<b>Research on Performances of Hybrid Actuation System with Dissimilar Redundancies</b> L.M. Yu and Z.Q. Ye	1559
<b>Optomechanical Design and Analysis for Rotating Telescope Optical System</b> L.C. Zhao and Y.T. Fu	1564
<b>The Static and Dynamic Characteristics Analysis of a CNC Grinding Machine Bed Made from Artificial Granite</b> H.L. Zhao, B.W. Ren, Y.M. Huang, G.P. Zhang, B. Wang and D.H. Mu	1568
<b>Study on the Plant Protection Effect of Highway Slope</b> Q. Wu, Y. Chen and L. Zhang	1573
<b>Research of On-Line Large-Size Forging Measurement System Based on LabVIEW</b> X.L. Zhao and J.S. Liu	1577
<b>Study on Damage Capabilities of Multiple Hulls Structure under Underwater Explosion</b> F.Y. Zhou, T. Jiang, W.L. Wang, K.Y. Zhang and F.M. Zhan	1581
<b>Design Research on a Kind of Derivative Welding Device of Car Door</b> J.C. Lv and L.B. Yang	1587
<b>The Filtering Mechanism Modeling and Simulation of Passive Power Filter Based on Differentiator Circuit</b> W.N. Yu, S.W. Li and M.Y. Zheng	1593
<b>Dynamic Response of Marine Gear under External Impact Load</b> C. Li, C.H. Qiu and N.L. Lu	1597
<b>Discuss of Express Tunnel Design in Poor Geology Area</b> H.L. Fu, W.B. Lu, Y.W. He and D.R. Ouyang	1602
<b>Electrical Resistivity of Rubberized Cement-Soil in Formidable Environment</b> F.C. Wang, Y. Zhou, M.Y. Zhang and X.J. Yin	1606
<b>Dynamic Simulation for Rolling Impact Compaction Machine</b> Y.S. Gao, Z. Song, A.H. Wang and Z.K. Jin	1610
<b>Finite Element Optimization Design of the Movable Jaw on PC5282 Jaw Crusher</b> N.Q. Guo and W.P. Huang	1614
<b>Research on Mechanism of Two Phase Flow Lifting Pressure Equipment and Output Regulation</b> G. Li, Y.H. Huang, Z.L. Lv and H.L. Huang	1619
<b>Sensitivity Analysis of Input Parameters of Cartesian Serial-Parallel Manipulator</b> J.G. Luo and M.Y. He	1624
<b>Analysis on Quality Issues for External Thermal Insulation System on Outer Walls</b> D.T. Wang	1628

---

<b>The Non-Linear Analysis of Cable</b> X.Y. Sun and Z.Q. Wang	1632
<b>Relative Dynamic Stiffness Testing and Vibration Suppression Technology for the Complete Set of High-Precision CNC</b> F.T. Wang, B. Zhang, Y.Y. Zhang, X.H. Fu and L.H. He	1636
<b>The Creation of the Special Characters Based on AutoCAD</b> L.L. Zhang, D.H. Jiang, D.W. Shao and Y. Zhao	1641
<b>Reliability Evaluation on Machining Center Based on Three-Parameter Weibull Distribution</b> G.C. Ren, Z.W. Yang and B.M. Meng	1645
<b>Depth Control of an Electro-Hydraulic Servo System Based on Fractional Order PID</b> Q. Gao, L.J. Ji, R.M. Hou and J.L. Chen	1650
<b>Upwind Finite Element Method for Solving Radiative Heat Transfer in Graded Index Media</b> L. Zhang, S.Y. Wang and G.L. Niu	1655
<b>Study on Two Degrees of Freedom Turntable with Large Panel Array</b> Y.G. Liu, Z.J. Wang and L. Qin	1659
<b>Analysis of Static Stability of Articulated Hydraulic Excavator with Two Degree of Freedom</b> D.X. Sun and X.H. Liu	1663
<b>Design of Portable Gas Detector Based on DSP</b> X.D. Zhu, T. Han, W. Lu, L. Xing and D. Xue	1667
<b>An Image Restoration Algorithm Based on Improved RBF Neural Network</b> X.Z. Zhao, Z.Y. Liu and Y.J. Xi	1671
<b>Minimal Query Algorithm of XML Document Based on Unconstrained Tree Pattern</b> H.B. Nie and Y. Wang	1677
<b>The Research and Implementation of Expert Identity Authentication Technology in the Science and Technology Awarding Review System</b> Y.H. Ma, X.X. Liu and C.X. Hu	1682
<b>Generating STEP-NC Files for a Circuit Board Milling System</b> K. Wang, C.R. Zhang, R.L. Liu and X.Z. Zhang	1686
<b>Refining the Applications of Computer-Aided Numerical Methods to Differential Settlement of Foundation</b> L.X. Luo, Z.G. Mu, H. Chen, B.H. Li and R.L. Yang	1696
<b>Freeway Slope Stability Evaluation Based on Multi-Level Fuzzy Neural Network</b> Y.K. Wu, X.S. Sang and B. Niu	1700
<b>Application of Equipartition of Entropy Production Principle in Plate Heat Exchanges with Different Corrugation Angles</b> C.S. Guo, W.J. Du and L. Cheng	1704
<b>Structural Optimization Research on Girder of 200t Bridge Crane Based on ANSYS</b> Z.Y. Ning	1708
<b>Influence of Convalescence on Soil Temperature Field of Well Group around Vertical Single-U-Tube Ground Source Heat Exchangers</b> Z.Y. Du and Y.X. Zhang	1712
<b>The Finite Element Simulation Used in Straight Tooth Bevel Gear's Vibration Rotary Forging</b> G.P. Cai, X.H. Zhao and H.T. Su	1716
<b>Monofractality of the Time Series Generated by Golden Section</b> H. Zhang and K.Q. Dong	1721
<b>Cubic Hybrid Mechanism Based on S[T] Output Base and P/R Input Base</b> J.G. Luo and M.Y. He	1725
<b>Experiment of the Rockfall Impact Characteristic onto Gravel Cushion</b> H.M. Tang, L.F. Wang, H.K. Chen and R.J. Wu	1729
<b>Simulation Test Research of Using the Ritchey-Commom Method for the Detection of Large Flat Mirror</b> S. Zhu and X.H. Zhang	1733
<b>Improved on the Routing Protocol of WSN for the Coal Mine Safety</b> Q. Zhang, W.Y. Shen, W.Q. Xu and B.G. Xu	1738

---

<b>Analysis for Combustion Process in Cylinder of 5S60 Diesel Engine</b> G.J. Chen, Z.M. Liu, T.T. Liu, S.H. Su, G.J. Yuan and Y.J. Cao	1742
<b>Study on Fuzzy Control for Vehicle Dynamic Stability</b> F. Du, Z.W. Guan and G.H. Yan	1747
<b>The Finite Element Analysis of Cable</b> X.Y. Sun and Z.Q. Wang	1751
<b>The Security and Privacy Protection in RFID</b> C.C. Fu and W.L. He	1755
<b>The Establish of Digital Simulation System on Continuous Cross-Flow Dryer</b> F. Han, C.C. Zuo, H. Zhu, W.F. Wu and C.S. Liu	1759
<b>Ultrasonic Assistance in Electrofinishing and Grinding on Cylinder Surface</b> P.S. Pa	1764
<b>Research on Aerodynamic Noise Reduction with Non-Smooth Surfaces of Exterior Rearview Mirror Cover</b> X. Chen and L. Yang	1768
<b>Development Scenario and Riser Selection for West Africa's Target Oil Field</b> J.P. Liu, X.L. Luo, M.L. Duan, K. Tian and W. Feng	1773
<b>Face Tracking Algorithm Based on Sequential Monte Carlo Filter</b> Y.M. Du, B.B. Yan and Y.C. Jiang	1777
<b>Design of DSP F2812 Control System in Paste Extrusion Experimental Device</b> H.J. Liu, H. Chen, H.B. Zheng and H. Gao	1782
<b>The Research on the Application of Two Kinds of Light Sources in the Training Venue for Physical Education of Universities</b> S.F. Li	1786
<b>Experimental Study of Influence of Grass Coverage on Runoff Shear Force of the Slope Surface</b> Q. Wu, Y. Chen and L. Zhang	1791
<b>Standard Reflecting Plate for Measurement of Radar Absorbing Materials in 3 mm Band</b> H.L. Yan, T. Hong and J.C. Zhao	1795
<b>The Study of Bus Superstructure Strength Based on ECE R66</b> G.S. Zhang, W. Wang, S.A. Piao and X. Dong	1799
<b>The Construction Technology of Large Amount Concreting to Pouring the Over-Length and Extra-Large Diameter Piles Foundation in Deep Water</b> L. Mu, M.J. Zhou, Y.T. Hu and Y.L. Du	1805
<b>Study on the System Characteristic of a Crane Walking Hydraulic System Based on AMESim</b> L. Li, X.Q. Wu, H.Y. Zhao and X.M. Shan	1809
<b>Application of Rough Set Theory in Stochastic Fatigue Analysis of Vehicle Frame</b> L.H. Zhao and C.H. Liu	1814
<b>Safety Analysis of Arch Dam</b> Y. Xia, Y.Y. Yu, Z.Q. Zhang and X.L. Zhao	1818
<b>Experiment on Vibration Reducing Capacities of Pore Viscous Damping and Liquid Film Damping</b> S.Q. Zhao, D.H. Zhu, Y.X. Qi and H.L. Chen	1822
<b>The Collaboration Control for the Multi-Robot Polishing System</b> M. Yu, H.P. Liu and J. Ji	1826
<b>Bearing Capacity of the Corrosion Reinforced Concrete Axial Compression Members</b> G.Y. Wang, Z.P. Wang, Y. Yin and F.C. Wang	1830
<b>Steady State Modeling of LHP and Analysis</b> Y. Chen, W. Chang, S.S. Zhang and C.S. Guo	1834
<b>The Study and Design of the Wood Horniness Alloy Milling Cutter CAD System</b> Q. Pan, D.H. Jiang and W.M. Lin	1839
<b>A Prediction Model of Concrete Fatigue Residual Strength</b> X.H. Meng, Y.X. Zhang and J.H. Zhou	1843
<b>Vibration of a Crane System Superimposed upon its Nominal Motion</b> J.F. Zhang and Q.R. Luo	1847
<b>The Finite Element Analysis and Improvement Practice of Shaker Based on ANSYS</b> S. Zhang and Y.H. Yang	1851

---

<b>Centralized Router Election for IP-WSN Based on Facility Location Model</b> Z.H. Wu and X.C. Huang	1855
<b>Research on the Application of Compound-Grouting Reinforcement Technology to Earthquake Damaged Masonry Structure</b> Y. Zhang, P. Liu, J. Cheng and R. Liu	1859
<b>Simulation Research of Distributing Valve of Underwater Hydraulic Breaker</b> Z. Chen, H.Q. Sun, X.Z. Liu and Y. Zhao	1862
<b>Design of Six Freedom Vibration Acquisition System for Military Vehicle</b> Z.X. Zhu, S.S. Zhu, G.J. Wang and Y. Zhu	1866
<b>A Novel Method for Tramcar Anti-Collision Warning System Based on Monocular Vision</b> H.B. Bi, X.D. Xian and L.J. Huang	1871
<b>A Superfluous Force Suppression Method Based on Structure Invariance Principle with Particle Swarm Optimization Algorithm</b> G.Z. Zhou, D. Guo and X.Y. Qi	1877
<b>Intelligent Grain Storage Measurement System Design and Research</b> G.C. Ren, Y. Yang and H.C. Guo	1881
<b>A Novel Method of Electrical Discharge Machining in Gas Gap State Control</b> Z.X. Lu, L.E. Guo, Y. Yan and J.J. Li	1886
<b>The Finite Analysis of the Piezoelectric Shell Stack Transducer</b> Y. Lu, L.K. Wang, L. Qin and D.K. Cai	1890
<b>Dynamic Characteristics Analysis of Supercavitating Vehicle Structure with Stochastic Parameters</b> Y.H. Jiang, W.G. An and H. An	1894
<b>Critical Technique and Design Method of Test Data Acquisition System for Centrifugal Shaker</b> Y.Z. Wang, X.M. Yuan, H.H. Huang and R. Sun	1898
<b>Comparative Study of Gobi Soil Subgrade Settlement Forecasting Methods for Double Line 2 of Lanzhou-Xinjiang Railway</b> Z.H. Nie and K. Li	1902
<b>Autoclaved Fly Ash-Lime Brick Wall of the Proposed Shear Strength Formula</b> L. Pan and C. Han	1906
<b>A System's MTTR Allocation Method Based on the Time Factors</b> D. Zhou, C. Lv and Y.X. Li	1910
<b>Reliability Analysis of Hybrid Actuation Based on GSPN</b> L.M. Yu, S.Q. Wei, T.T. Xing and H.L. Liu	1914
<b>Dimension Error Analysis of Bearing Manufacture Based on Probability Statistics</b> G.C. Chen, T.W. Xie and F.H. Mao	1918
<b>Research of Precision CNC Internal Grinder Soft-PLC System Based on Embedded Technology</b> O. Xie, H. Li and Z. Yin	1925
<b>The Research on the Robot Vision System Based on the Target Clamping Technology</b> H.X. Wen and W.S. Wang	1929
<b>Study on Integration of Equipment Running Status and the Management Model Based on Graphical</b> M.M. Wu and H.N. Tu	1935
<b>Study on Remote Condition Monitoring and Fault Diagnosis System for Rotating Machinery Based on LabVIEW</b> C.H. Wu, Y. Gao and Y. Guo	1939
<b>Analysis on Degree of Freedom and Singularity of Mechanism Based on Topological Graph Theory</b> J.G. Luo and M.Y. He	1943
<b>Tilt Measurement with a MEMS Accelerometer Based on Kalman Filter</b> Q.H. Ji	1947
<b>The Research on the Control System of Bulldozer Based on the EPEC Controller and its Traction Experiment</b> P. Xing, L.C. Peng, Y. Xu, C.B. Liu and C.F. Tian	1952
<b>Testing Technology Research on Actual Effect by Construction Piled Pipes in Buried Pipe System of Ground Source Heat Pump</b> X.H. Xie, Y. Li, Y. Lai and Y. Cao	1957

<b>Picking Robot Camera Calibration System Based on OpenCV</b> H.X. Peng, X.J. Zou, J.T. Xiong, D.Z. Wu, J.H. Shen and Z.X. She	1963
<b>Current Situation Analysis on Soil Erosion Risk Management in Development and Construction Project</b> Q. Wu, L.L. Wang, H.Q. Gao and Y. Chen	1967
<b>Block Mechanism of Microclearance Block Liquid and Lifting Height Calculating</b> Y.N. Gong, J.D. Yin, C. Ai and Y.K. Zhang	1970
<b>Research on Risk Assessment of Reservoir by AHP-Fuzzy Comprehensive Analysis Method</b> L.G. Tian and Z. Liu	1974
<b>Study of the Performance of Practical Magneto-Rheological Elastomers</b> W.B. Feng, X. Yang and Z.Q. Lv	1979
<b>The Simulation and Experimental Study on a Novel Vehicle Active Suspension with Electro-Hydrostatic Actuator</b> F.R. Kou, J. Ma and J.B. Wang	1984
<b>Design of Wireless Temperature Sensor Network Based on nRF905</b> Z.H. Xing, H.W. Wang, X.N. Wang, Q.M. Surong, C.J. Qi and W.K. Zhang	1988
<b>Effect of Rainfall Infiltration on Loess Pitted Courtyard Cave Dwellings Stability</b> J.M. Han and S.Q. Su	1992
<b>Shape Optimization of Lower Control Arm under Typical Road Conditions</b> L.H. Zhao, H. Gu and Q.Q. Hong	1996
<b>Study of the Mathematic Modeling Method of the Center Distance Minimum for Gear Set of Spur Gear</b> X.S. Wang and Y. Chen	2000
<b>Numerical Simulation of the Three Component Coefficients of Bridge</b> Y.F. Huang and J.X. Yang	2004
<b>Liquid-Phase Oxidation Modification of Carbon Fiber Surface</b> W.B. Lu, C.G. Wang, H. Yuan and X.Y. Hu	2008
<b>Study on the Evaluate Methods of Comparative Test</b> X. Yu	2013
<b>Numerical Simulation of Radiation Heat Transfer in a One-Dimensional Graded Index Sphere</b> L. Zhang, S.Y. Wang and G.L. Niu	2017
<b>Application System Based on the Combination of Touch Screen and PLC</b> H. Zhang, W.F. Wu, Z. Liu, H.D. Fu, Y. Wang and X.W. Li	2021
<b>Research on Embedded Numerical Control System Software Based on ARM Microprocessor</b> Y. Wang and J.Y. Zhang	2026
<b>Duct Cleaning Robot Comprehensive Kinematics Modeling and Analysis Considering the Complex Terrain</b> B.Q. Wu, W. Sun and M.H. Ouyang	2032
<b>An Investigation of GFRP Bar Reinforced Light Weight Concrete (LWC) Bridge Deck</b> J.W. Huang	2037
<b>Constant Acceleration Control of Valve-Control-Cylinder System Based on Neural Network</b> J.G. Ma and X.Y. Shang	2041
<b>The Application of Anchor in the Urban Underground Engineering</b> C.S. Luo	2046
<b>Rolling Bearing Fault Diagnosis Based on Fractal Dimension</b> M. Li	2050
<b>Fault Diagnosis of Gearbox Based on ICA and Envelope Analysis</b> B. Li, Y. Guo, T.W. Liu and Y. Gao	2054
<b>The Discuss about the New Approach of the Structural Layout of Belt Type Sintering Machine</b> X.J. Wang, M.H. Bai, S.B. Ren and J.W. Chen	2058
<b>The Inquiry about the Application of the LED and High Pressure Sodium Lamp in the Universities Sports Teaching Venue</b> S.F. Li	2062
<b>Sustained Casing Pressure Calculation of A Annulus Induced by Downhole Operation Load</b> Z. Zhi, T.P. Xiao, Z.M. Chen and T.H. Shi	2067

<b>Structure Optimization for Backrest Frame of CRH Seat Based on DOE Analysis</b> L.H. Zhao and Y.L. Tao	2071
<b>The Field Study of the Remediation of Mud-Pumping</b> H.L. Fu, K. Li, Y.W. He and X.Z. Zhu	2079
<b>Oil-Soluble DRA Development and Application</b> Z.J. Long, Y.R. Fu, D.Q. Li and Y.H. Cai	2083
<b>Mechanism Study of Arch Dam</b> Y. Xia, Z.Q. Zhang, S.K. Ma and X.L. Zhao	2087
<b>Investigation on Microstructure and Mechanical Property of the A7N01 Aluminum Alloy Welding Joint</b> S.L. Yang, B. Luo, R.Y. Lv, L.C. Meng and Q.L. Lin	2091

**Chapter 1:**  
**Advanced Materials Science**

## **Effect of a novel phosphorus and silicon system on flame retardancy and thermal degradation of PC**

Wei Zhao<sup>a</sup>, Bin Li<sup>b</sup>

Key Lab of Bio-based Material Science and Technology (Northeast Forestry University), Ministry of Education, Harbin 150040, P. R. China.

<sup>a</sup>zhaowei426@163.com, <sup>b</sup>libinzh62@163.com (corresponding author)

**Keywords:** Flame retardant, Polycarbonate, Phosphine, Silicon resin.

**Abstract.** The novel phosphine was used with a silicon resin to impart flame resistancy to polycarbonate. Combustion behaviors and thermal degradation properties of flame retardancy PC have been assayed by limiting oxygen index, vertical burning test and thermogravimetric analysis. Dynamic rheological of FR-PC was also examined. Flame retardant consisted of 80 wt.% PPPO and 20 wt.% silicon resin possesses excellent flame retardancy for PC. LOI value of FR-PC is 33.0% and passes UL-94 V-0 rating. SEM revealed that the char yield as well as char properties have direct effects on the flame retardancy.

### **Introduction**

Polycarbonate (PC), a widely used engineering plastic, has outstanding properties including good hardness, impact strength, transparency, dimensional stability, and thermal stability. Therefore, it is widely used in the fields of optical equipment, construction, automobiles, electrical and electric devices, and so on [1-3]. PC by itself shows a limiting oxygen index (LOI) of approximate 28% and V-2 rating in the vertical burning test (UL-94). But more stringent flame retardant performance is required in application of electrical and electric devices [3].

Phosphines have good thermal stability and solvent resistance [4]. Moreover, they are preferred to flame retardant [4, 5]. The compounds can take place in vapour phase by a radical mechanism to interrupt the exothermic processes and to suppress combustion. They can also act in condensed phase. The compounds incorporated polymer materials act like acid precursors and acids participate in char formation. And then a protective layer is formed to prevent further burning. Some phosphines were used to enhance flame retardancy to polymer materials. [6, 7].

In this work, a novel aromatic phosphine phenylene phenyl phosphine oligomer (PPPO) was used to impart flame retardancy to PC. Because silicon compounds can enhance flame retardant properties of polymer, a new flame-retardant system, PC/PPPO/silicon resin system is developed. Effects of oligomer on flame retardancy, thermal degradation and dynamic rheological properties of FR-PC systems were investigated.

### **Experimental**

**Materials.** PPPO was synthesized in our laboratory. Titanic oxide (TiO<sub>2</sub>), molecular sieve (4A) and montmorillonite (MMT) were purchased from Sanding Chemical Co. (Zhejiang, China). A silicon resin (DY-MQ102) was obtained from Dayi chemicals industry Co. Ltd. (Shandong, China). PC 2805 was provided by Bayer Germany and was dried in the oven at 120 °C for 6 h before use.

**Preparation of samples.** PC, PPPO and fillers were mixed in a RM-200A rheometer (HAPRO, Haerbin, China) at a temperature of 250 °C and a rotor speed of 50 rpm for 8 min. The samples were pressed on a curing machine at 190 °C for 3 min into sheets of suitable thickness and size.

**Measurements.** The LOI values were measured at room temperature on a JF-3 oxygen index meter (Jiangning Analysis Instrument Company, China) according to ISO4589-1984 standard. The dimensions of all samples are 130 mm × 6.5 mm × 3 mm. Vertical burning tests were carried out on a CZF-2-type instrument (Jiangning Analysis Instrument Company, China) with the dimension of 130 mm × 13 mm × 3 mm according to UL-94 test standard. UL-94 testing results are carried out by burning ratings V-0, V-1, or V-2. V-0 rating presents the best flame retardancy of polymeric materials. The rheological measurements were carried out on a rotational rheometry (AR 2000ex, TA, America) at 250 °C with parallel plate geometry of 20 mm in diameter. The frequencies were from  $10^{-1}$  to  $10^2$  s<sup>-1</sup>. TGA data were conducted using a Perkin Elmer Pyris 1 Thermal Analyser. A heating rate of 10 °C·min<sup>-1</sup> was used. Samples (2-4 mg) were contained in a standard platinum pan and heated from 50 to 800 °C. The sample compartment was purged with pure nitrogen at 20 ml·min<sup>-1</sup> during analysis. Morphological studies on the residual chars were taken using a FEI QUANTA-200 (USA) scanning electron microscopy at an acceleration voltage of 15 kV.

## Results and discussion

**Flame retardancy.** Results of LOI values and UL-94 rating with different loadings are presented in table 1. LOI of PC was 28.1%. With increase of PPPO contents LOI values increase for all FR-PC. The sample with 5 wt.% PPPO has a high LOI value of 32.4%. Addition of 5 wt.% PPPO does not help with flame retardancy well. The sample was classified as V-2 rating because of its drips during the UL-94 measurement. It was reported that mineral filler and silicon compound could obviously improve the combustion behavior [8, 9]. In order to pass V-0 rating, several kinds of fillers were selected. When 1 wt.% TiO<sub>2</sub>, 4A molecular sieve and MMT were added into the sample, value of LOI decreased compared to PC/5 wt.% PPPO. UL-94 rating kept V-2 and dripping occurred. Co-addition of silicon resin drastically changed the combustion performance of PC. Combination of 4 wt.% PPPO and 1 wt.% silicon resin provided a V-0 rating and 33.0% of LOI.

Table 1 Flame retardancy of PC/PPPO/ filler systems

Samples	LOI	UL-94 rating	Dripping
PC	28.1	V-2	Yes
PC/1%PPPO	28.6	V-2	Yes
PC/3%PPPO	30.2	V-2	Yes
PC/5%PPPO	32.4	V-2	Yes
PC/4%PPPO/1%TiO <sub>2</sub>	29.6	V-2	Yes
PC/4%PPPO/1%4A	28.9	V-2	Yes
PC/4% PPPO/1%MMT	31.4	V-2	Yes
PC/4%PPPO/1Si resin	33.0	V-0	No

Melt viscosity of FR-PC system was evaluated using complex viscosity ( $\eta^*$ ) of dynamic rheological analysis. As figure 1 shown, the shear thinning behavior exists for all samples with increase of frequency. This is a general characteristic of polymer melts. From  $10^{-1}$  to  $10^2$  s<sup>-1</sup>, flame retardants increase the viscosity of system in comparison to PC and the curves become smooth. It means that the FR-PC become insensitive to shear. When 1 wt.% silicon resin was added, complex viscosity of the system increased dramatically even in low frequency. As the melt viscosity of FR-PC system increased to a certain extent that was enough to hang over the char layer, it was considered that the dripping disappeared.

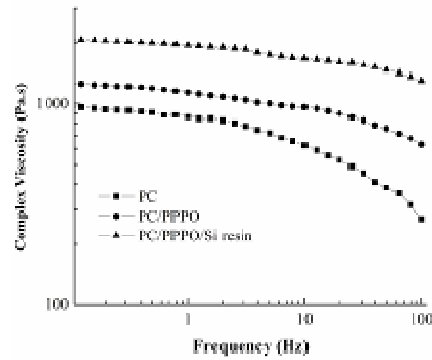


Fig. 1 Complex viscosity  $\eta^*$  for PC and FR-PC at 250 °C

**Thermal properties of composites.** TGA and DTG curves for FR-PC system are shown in figure.  $T_{\text{initial}}$  is defined as the temperature at which 5% weight loss occurs and  $T_{\text{max}}$  is defined as the temperature at maximum weight loss rate. Thermal decomposition data are presented in table 2.

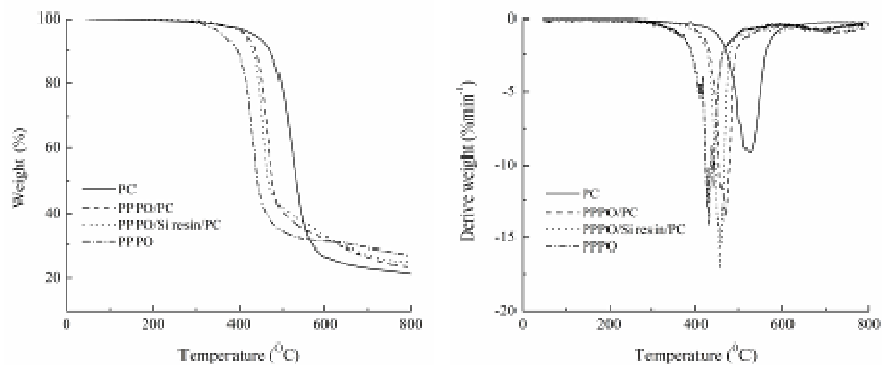


Fig. 2 TGA and DTG curves of FR-PC system under a  $N_2$  atmosphere  
Table 2 TGA data of PPPO and FR-PC systems under a  $N_2$  atmosphere

Samples	$T_{\text{initial}}$ (°C)	$T_{\text{max}}$ (°C)	The char residues at 800 °C(%)
PPPO	363.2	429.2	26.5
PC	433.9	523.9	21.3
PC/5 wt.% PPPO	415.3	469.8	23.1
PC/4 wt.% PPPO/1 wt.% silicon resin	395.1	455.1	24.7

From the TGA curves, it can be seen that thermal decomposition behaviors of all samples mainly undergo in one step process. PPPO does not show any significant weight loss at temperatures below 350 °C. However, it undergoes rapid weight loss between 400 and 500 °C. The  $T_{\text{initial}}$  and  $T_{\text{max}}$  of the PPPO were 363.2 °C and 429.2 °C, respectively. Residues of PPPO at 600 °C and 800 °C in nitrogen atmosphere are 31.2% and 26.5%, respectively, indicating that PPPO has very effective charring ability.

Addition of PPPO to PC at 5 wt.% leads to a critical advance in the thermal degradation processes of PC.  $T_{\text{initial}}$  recorded decreases from 433.9 to 415.3 °C.  $T_{\text{max}}$  decreases from 523.9 to 469.8 °C and residual char yield slightly increased by 8.5%. A small amount of PPPO influenced strongly the thermal degradation of PC. Additions of PPPO and silicon resin influence the thermal degradation of PC effectively and degradation temperatures decrease.  $T_{\text{initial}}$  and  $T_{\text{max}}$  drops to 395.1 °C and 455.1 °C, respectively. And the residual char yield enhances to 24.7%.

**SEM analysis.** Figure 3 showed the SEM of the char layer from combustion. There existed bulky and loosen porous structure on the surface of PC (figure 3 a). This structure cannot provide a good barrier to the transfer of heat and prevent the underlying PC from degradation and combustion. A

very distinct difference in appearance was observed on the charred FR-PC. The surface of the sample of PC/5 wt.% PPPO system was covered by continuous and protective char layer (shown as figure 3 b). As silicon resin was added into PC/PPPO system, the surface of char from PC/4 wt.% PPPO/1 wt.% silicon resin was tight, indicating a dense char structure (shown in figure 3 c). A high-quality char can effectively form a protected layer to stop the propagation of heat and oxygen to melt polymer matrix during combustion.

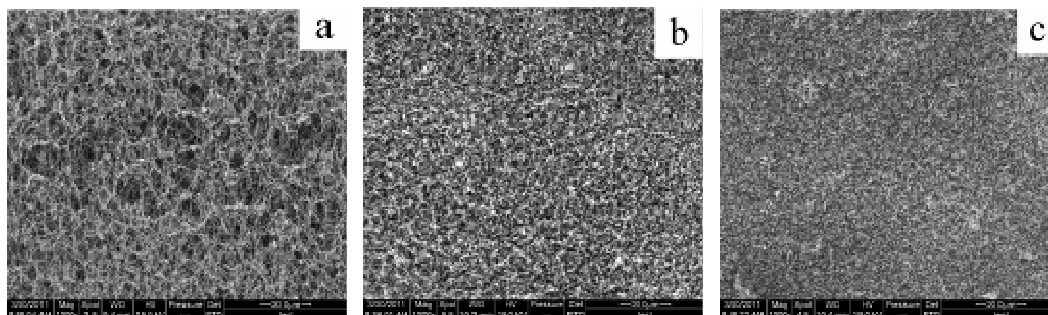


Fig. 3 SEM of the char layer (a): PC, (b): PC/5 wt.% PPPO (c): PC/4 wt.% PPPO/1 wt.% silicon resin

## Conclusions

A novel phosphine oligomer PPPO was successfully synthesized, using organolithium reagents reactions with DCPD and the chemical structure was confirmed. PPPO has good thermal stability and can be used as an efficient flame retardant for PC. The LOI value of PC/5 wt.% PPPO system reached to 32.4%. Combination of PPPO with silicon resin helps to produce a significant flame retardant effect in PC. PC shows V-0 rating and 33.0% of LOI in the presence of 4 wt.% PPPO and 1 wt.% silicon resin, based on experimental results of flame retardancy. Effects of PPPO and silicon resin could accelerate decomposition and char formation, which was proved by thermal analysis, dynamic rheological analysis, the morphology of the char and cone calorimeter test. Mechanical properties data indicated that the effect of flame retardants on mechanical properties of FR-PC systems was not significant.

## References

- [1] J.B. Wang and Z. Xin: *J. Appl. Polym. Sci.* Vol. 115(2010), p. 330
- [2] K.H Pawlowski and B. Schartel: *Polym. Inter.* Vol. 56(2007), p. 1404
- [3] W.C. Zhang, X.M. Li, X.Y. Guo and R.J. Yang: *Polym. Degrad. Stab.* Vol. 95(2010), p. 2541
- [4] G. Ribera, L.A. Mercado, M. Galià and V. Cádiz: *Appl. Polym. Sci.* Vol. 99 (2006), p. 1367
- [5] M. Shau, P.F. Tsai, W.Y. Teng and W. Hsu: *Eur. Polym. J.* Vol. 42(2006), p. 1899
- [6] K. Faghihi and K. Zamani: *J. Appl. Polym. Sci.* Vol. 101(2006), p. 4263
- [7] M.J. Alcón, G. Ribera, M. Galià and V. Cádiz: *Polym.* Vol. 44(2003), p. 7291
- [8] B.N. Jang and C.A. Wilkie: *Polym. Degrad. Stab.* Vol. 9(2005), p. 2933
- [9] A.B. Morgan: *Polym. Degrad. Stab.* Vol. 14(2006), p. 206

## Effect of Long-Term Aging on the Tensile Properties of Nickel-Based Superalloy

Liwei Xu<sup>1,a</sup>, Huabing Li<sup>2,b</sup>, Qifeng Ma<sup>2,c</sup>, Zhouhua Jiang<sup>2,d</sup>

<sup>1</sup>Taiyuan Iron & Steel (Group) Co. Ltd., Taiyuan 030003, PR China

<sup>2</sup>School of Materials and Metallurgy, Northeastern University, Shenyang 110004, PR China

<sup>a</sup> 13303519730@163.com, <sup>b</sup> lihb@smm.neu.edu.cn, <sup>c</sup> kylvnm@126.com, <sup>d</sup> jiangzh@smm.neu.edu.cn

**Keywords:** Ni-Based superalloy, Long-term aging, Tensile properties, Deformation behavior

**Abstract.** The influence of microstructure evolution of a nickel-based superalloy after long-term aging on the tensile properties and deformation behavior was investigated. The results shows that the aging time exhibits a significant effect on the strength of alloy under low strain rate and the elongation decrease with increasing the aging time, but the aging time has no obvious effect on the strength of the alloy and elongation is affected significantly by aging time. During deformation under high strain rate, the dislocation motion is blocked and the dislocation can not release in time, the strengthening phase peak size effect does not appear in the aging time ranging from 0h to 1000h, so the influent of aging time on the strength of the alloy is not obvious. After long-term aging, no precipitation appear in both sides of the grain boundary which leads to the coordination ability of plastic deformation of grain boundaries reducing, so the ductility of the alloy decreases rapidly in a short aging time.

### Introduction

With the rapid development of the aerospace industry, the service environment of nickel-based superalloy is becoming more increasingly complex[1]. In order to obtain the high hot-strength in high-temperature service, the alloying degree of nickel-based superalloy is increasing which leads to the decreasing the stability of microstructure during the high-temperature and long-time service, and even a lot of TCP precipitation phase at the grain boundaries which leads to the appearance of the brittle failure in a large number of caused by catastrophic the phenomena of disastrous brittle failure[2]. The alloy used as the critical rotating parts such as turbine blades and turbine disks always bears dynamic loads and services under high temperature and high strain rate[3]. So the deformation behavior under dynamic loads is very important to use safety of nickel-based as the rotating parts under harsh service conditions[4, 5]. The present research focuses on the effect and mechanism of microstructure evolution of nickel-based superalloy used widely as aviation, aerospace, nuclear and petrochemical field after long-term aging on the tensile properties.

### Experimental Material and Method

The experimental alloy was produced by vacuum induction melting method, and forged into 80 mm × 160 mm billet and then hot-rolled into 80mm rods. The main chemical composition of alloys were (wt%): C 0.04, Fe 16.77, Cr 24.43, Al 0.89, Ti 1.92, Nb 3.15, Mn 0.02, P 0.001, S 0.001, B 0.004, Ni bal. After standard heat treatment, the materials were aged for 0h、100h、200h、500h and 1000h at 780°C. And then the tensile deformation tests were performed using the MTS 810 material testing machine under the strain rate of  $10^{-2} \text{ s}^{-1}$ 、 $10^{-1} \text{ s}^{-1}$  and  $10^0 \text{ s}^{-1}$  respectively. The change of microstructure and the tensile fracture morphology were observed by OLYMPUS GX71 optical microscope and JEOL 7001 scanning electron microscope. The microstructure near the tensile fractures was analyzed by TECNAI G<sup>2</sup> 20 transmission electron microscopy.

## Experimental Results

**Microstructure evolution during long-term aging.** The precipitation phases of the alloy vary with the aging time as shown in Fig.1. The microstructure of the alloy after long-term aging has an obvious change. The spherical precipitation by standard heat treatment changes into disc-shaped. Another strengthening phase  $\gamma'$  is spherical during 1000h aging time, and its size does not change obviously after 200h aging. When increasing the aging time to 1000h, the  $\gamma'$  phase grows slightly.

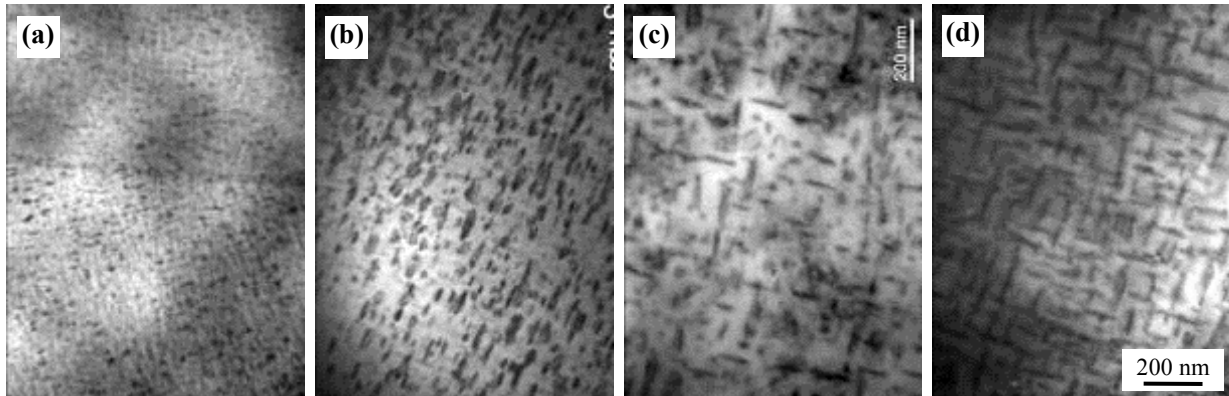


Fig.1 Morphology of precipitation phase after different aging time:  
(a) 0h, (b) 200h, (c) 500h, (d) 1000h

**Influence of long-term aging on tensile properties.** The changes of yield strength and elongation with aging time are shown in Fig.2. The phenomena can be observed clearly that the strength of the alloy becomes higher when increasing the strain rate under the same aging time. For three different strain rates, the influence of aging time on alloy strength is consistent. At low strain rate, the yield strength and tensile strength firstly increase and then decrease with extension of aging time. The yield strength and tensile strength essentially keep unchanged at  $10^0 \text{ s}^{-1}$  strain rate.

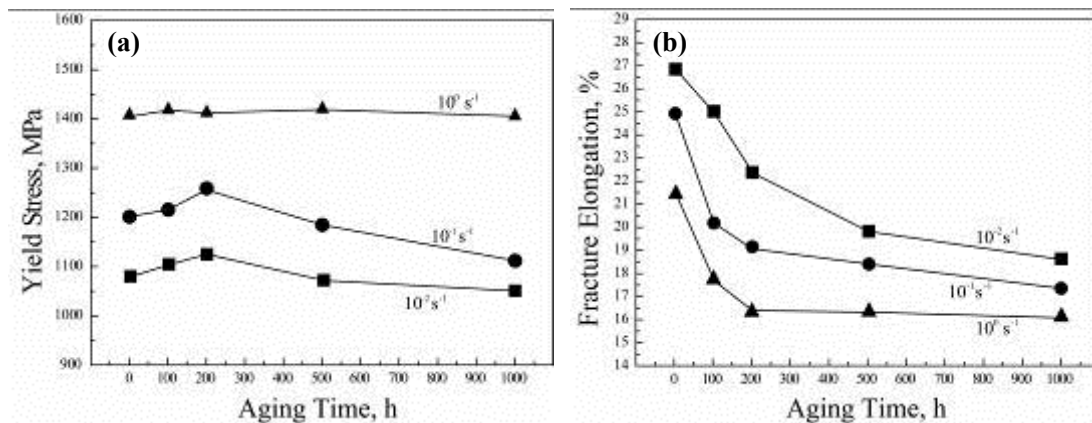


Fig.2 Change of the tensile properties of alloy with aging time:  
(a) yield strength (b) fracture elongation

The elongation of the alloy for same aging time decreases with increasing strain rate. After tensile deformation at three different strains rate conditions, the elongation decreases with increasing aging time. The reducing rate of plasticity of the alloy aging 100h increases with increasing the strain rate, the fracture elongation rapidly decreases, and then do not change at  $10^0 \text{ s}^{-1}$  strain rate.

**Influence of long-term aging on the morphology of tensile fracture.** The change of morphology of the tensile fracture fiber area with aging time is shown in Fig.3. A large number of dimples exist in tensile fracture without aging treatment. After aging treatment, the fluctuation of fracture increases and the size of dimples become no uniform, and secondary cracks can be observed at tensile fracture after 1000h aging, and intergranular fracture is obvious. At high strain rate, secondary cracks can be

observed at tensile fracture after 200h aging, and extend and increase with increasing aging time. When increasing aging time to 1000h, the fracture exhibits obvious sugar-like characteristics, and the toughness area decreases.

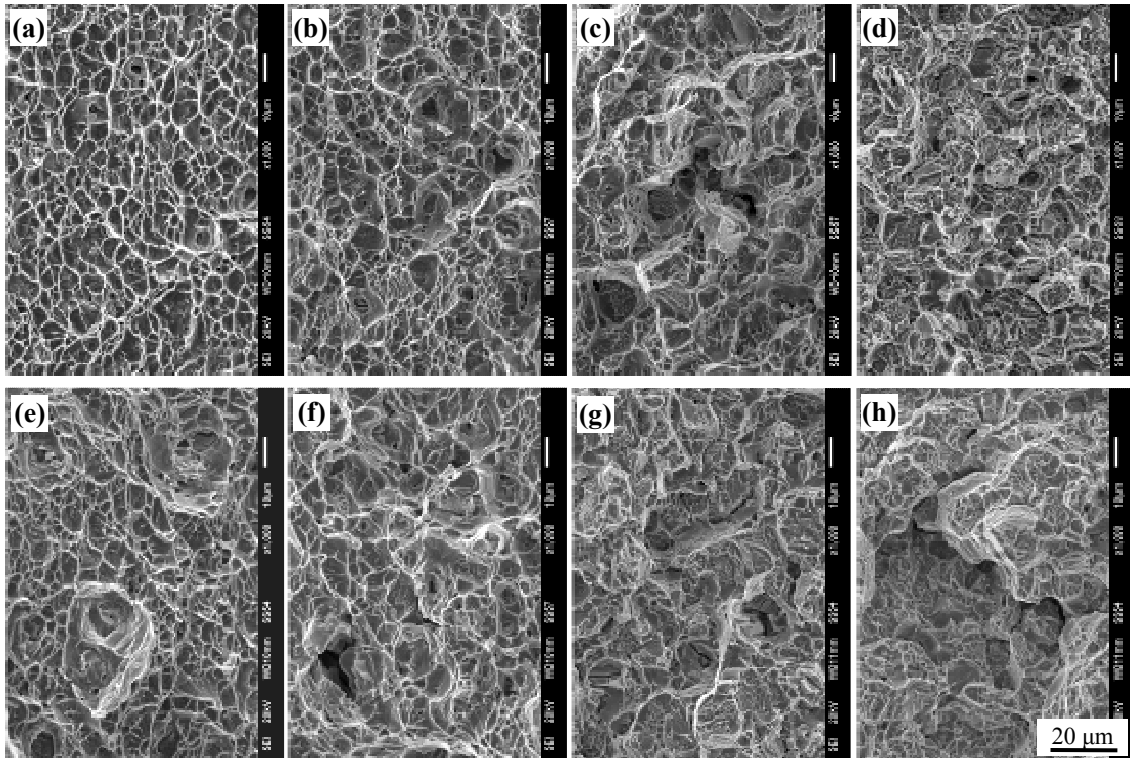


Fig.3 Change of morphology of of the tensile fracture with aging time under different strain rate:

- (a)  $\dot{\epsilon}=10^{-2} \text{ s}^{-1}$ , 0h; (b)  $\dot{\epsilon}=10^{-2} \text{ s}^{-1}$ , 200h; (c)  $\dot{\epsilon}=10^{-2} \text{ s}^{-1}$ , 500h; (d)  $\dot{\epsilon}=10^{-2} \text{ s}^{-1}$ , 1000h;  
 (e)  $\dot{\epsilon}=10^0 \text{ s}^{-1}$ , 0h; (f)  $\dot{\epsilon}=10^0 \text{ s}^{-1}$ , 200h; (g)  $\dot{\epsilon}=10^0 \text{ s}^{-1}$ , 500h; (h)  $\dot{\epsilon}=10^0 \text{ s}^{-1}$ , 1000h

## Discussion

At low strain rate, deformation resistance first increase then decrease with prolonging aging time. At this time, alloy still has good uniform plastic deformation ability. But the plasticity decreases with increasing aging time. But at high strain rate, after aging treatment and elastic deformation, the uniform plastic deformation process is very short. With increasing strain, the stress-strain curve rapidly enter the stage of non-uniform plastic deformation until fracture, and aging time does not significantly affect the stress-strain curve.

For superalloy the strengthening effect of precipitation phase mainly depends on hindering from dislocation motion[6]. When the percentage content of strengthening phase is the same, with increasing average size, dislocation motion changes from the cut-off mechanism into the bypass mechanism, the role of strengthen has peak value[7]. With increasing aging time, the size of precipitations increase, and strengthening effect first increases then decreases. So under the same strain, the deformation resistance firstly increases and then decreases, but the alloy still has good uniform plastic deformation. With increasing aging time, the precipitations at grain boundary worsen plasticity obviously, and plasticity decreases.

At high strain rate, the change of tensile properties with aging time is obvious which should have a relationship with dislocation motion mechanism. At low strain rate, multiple slip systems simultaneously activate at tensile fracture without aging treatment and the level of dislocation tangles is low as shown in Fig. 4. When aging time increases to 200h, the density and tangles of dislocation increase. With prolonging aging time, the density and tangles of dislocation decrease, but the characteristics of multi-line slip are not observed. At high strain rate, the characteristics of multi-line slip are obvious. When prolonging aging time, the density of dislocation does not change obviously, and multiple slip systems activating can be observed.

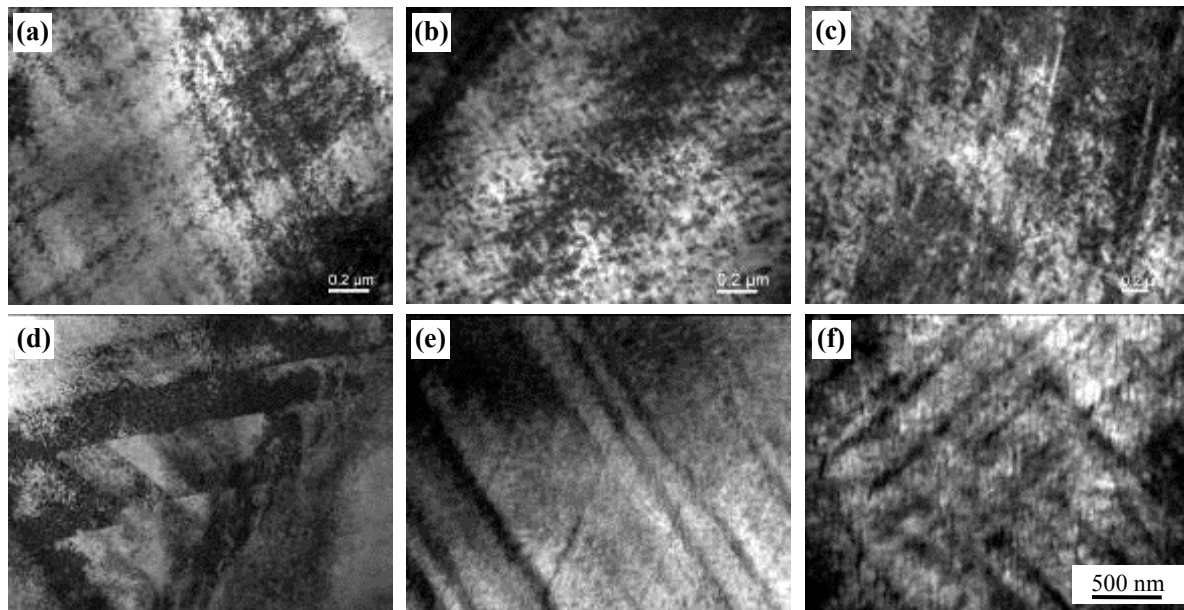


Fig. 4 Morphology of the dislocation near tensile fracture with different aging time:  
 (a)  $\dot{\epsilon}=10^{-2} \text{ s}^{-1}$ , 0h; (b)  $\dot{\epsilon}=10^{-2} \text{ s}^{-1}$ , 200h; (c)  $\dot{\epsilon}=10^{-2} \text{ s}^{-1}$ , 1000h; (d)  $\dot{\epsilon}=10^0 \text{ s}^{-1}$ , 0h;  
 (e)  $\dot{\epsilon}=10^0 \text{ s}^{-1}$ , 200h; (f)  $\dot{\epsilon}=10^0 \text{ s}^{-1}$ , 1000h

In the process of plastic deformation of metal crystals, the dislocation motion is blocked, releases through decomposition or climb, and the process takes some time to complete [8]. When the size of precipitation phase is small, the role of hindering dislocation motion is not strong, multiple slip systems activate at the same time, and the plastic deformation is good. After long-term aging treatment, the precipitation phases become bigger which increases the role of hindering dislocation motion and the interaction mechanism of dislocation movement changes at different strain rate. At low strain rate, dislocation movement is blocked and tangled, but releases by the decomposition and climb of dislocation. In the process of deformation at low strain rate and before the peak strengthening size of strengthening phase, dislocation cut through the strengthening phase and multi-line slips can be observed. With increasing aging time, the strength of the alloy increases. When the precipitations are larger than those at peak, dislocation decomposition and climb still are able to carry out, and the dislocation bypasses the strengthening phase, the phenomena of multi-line slips activating disappears. Moreover, the strength decreases with increasing aging time.

But during the process of deformation at high strain rate, the dislocation movement is blocked and cannot release by dislocation decomposition and climb due to the higher rate of strain and deformation. With increasing the size of strengthening phases, the phenomena of passing from cutting through to bypassing when the dislocation passes the strengthening phases. So in the process of deformation at high strain rate, after the aging treatment ranging from 0h to 1000h, the peak size effect of strengthening phase does not appear, and the dislocation cuts through strengthening phases. With increasing the strengthening phases, multi-line slips can be observed, and the strength does not change obviously.

The elongation of the alloy decreases rapidly in the aging 200h under high strain rate, the long-term aging leads to the occurrence of degradation phenomena in advance. And the alloy with the shorter aging time shows intergranular fracture characteristic, and exhibits a typical intergranular fracture when increasing aging time to 1000h. The precipitation phases within the grain transform to grain boundaries during the long-term aging, which increase the size of precipitation phases at grain boundaries. The needle-like precipitation phases along the grain boundaries or growing into grain can be observed. So some grain boundaries consist of the interface of precipitation phases and substrate. The needle-like precipitation phases continue to grow, which lead to no significant precipitation brand of strengthening phases between precipitation phases and substrate as shown in Fig.5.

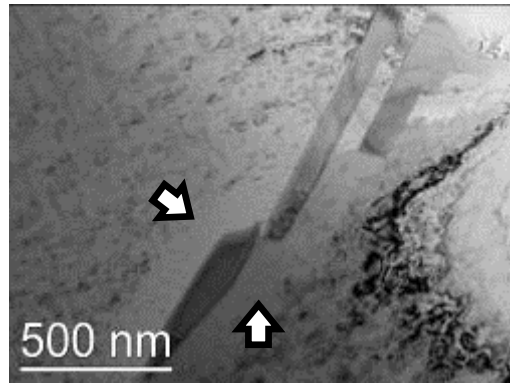


Fig.5 No precipitation band of strengthening phase near the precipitation phase at grain boundary of the alloy aging 500h at 780 °C

When deformation occurs with short aging time and low strain rate, dislocation pile-up and stress concentration existing in the precipitation phases along grain boundaries can release by the way of slip or climb, and the grain boundary has a certain ability to coordinate the plastic deformation[9]. With prolonging aging time, grain boundary precipitation phases continue to grow, the interface of precipitation phases and substrate replace a large number of grain boundaries. No precipitation band of strengthening phases continues to increase, which leads to the degree of dislocation pile-up and stress concentration, so the plastic deformation ability of the alloy decreases significantly.

### Summary

During the range of low strain rate, the strength of the nickel-based alloy firstly increases and then decreases with prolonging the aging time. But in the high strain rate, the alloy strength remains unchanged on the whole and the elongation is more significantly affected by aging time. When deformation of the alloy occurs under high strain rate, the dislocation motion is blocked and cannot release in time, the dislocation cuts through the strengthening phases with the size of strengthening phases increasing, so the strength of the alloy is not affected significantly. During the deformation process under high strain rate, the coordination ability of grain boundary reduces which leads to the plasticity decreasing rapidly after a short aging time.

### References

- [1] R. Sharghi-Moshtaghin and S. Asgari, *J. Mater. Prod. Technol.* Vol. 147 (2004), p. 343
- [2] J. B. Graverend, J. Cormier, P. Caron, S. Kruch, F. Gallerneau and J. Mendez, *Mater. Sci. Eng., A*, Vol. 528 (2011), p. 2620
- [3] G. H. Li, M. J. Wang and R. K. Kang, *Mater. Sci. Tech.* Vol. 18 (2010), p. 824.
- [4] X. Zan, Y. H. He, Y. Wang and Y. M. Xia, *J. Nonferr. Metal. Soc.* Vol. 21(2011), p 45.
- [5] W. S. Lee and C. F. Lin, *Mater. Sci. Eng., A*, Vol. 241 (1998), p. 48.
- [6] Q. Y. Huang and H. K. Li, *Superalloy*, Metallurgical Industry Publishing, Beijing, 2002, p. 246.
- [7] J. Friedel, *Dislocation*. Science Press, Beijing, 1980, p. 165.
- [8] M. A. Meyers, *Dynamic Behavior of Materials*, in: Q. M. Zhang, Y. Liu, F. L. Huang, Z. J. Lu (Eds), National Defense Industry Press, Beijing, 2006, p. 225.
- [9] Z. M. Zhou, *Evolution of dislocation configuration*, Northeastern University Press, Shenyang, 2003, p. 18.

## Effect of Fe doping on the morphology of hydrothermally derived BaTiO<sub>3</sub> crystals

Linlin Yang<sup>1, a</sup>, Yujiang Wang<sup>1, b</sup>, Shunli Huang<sup>2</sup>, Yonggang Wang<sup>\*1, c</sup>

<sup>1</sup>Department of Materials Science and Engineering, Luoyang Institute of Science and Technology, Luoyang 471023, China

<sup>2</sup>Henan Anyang Power Supply Company, Anyang 455000, China

<sup>a</sup>yangll968@yahoo.com.cn, <sup>b</sup>wang\_yu\_jiang@163.com, <sup>c</sup>wangyg968@yahoo.com.cn\*

**Keywords:** Hydrothermal; Fe doping; BaTiO<sub>3</sub> crystals

**Abstract.** Pure phase Fe doped BaTiO<sub>3</sub> crystals have been successfully fabricated at 200°C with 0.7M KOH by a hydrothermal method. The obtained products were characterized by X-ray diffraction (XRD) and transmission electron microscopy (TEM). An obvious morphology evolution from hexagonal shape to sphericity was observed when Fe doping concentration was increased from 0% to 1%, 3%, 6%, and 10%. In addition, the size of the obtained Fe doped BaTiO<sub>3</sub> crystals obviously became smaller. The possible mechanism was also discussed.

### Introduction

Multiferroic materials can exhibit a coexistence of simultaneous ferroelectric and magnetic order parameters, and have drew much attention because of the fascinating fundamental physics studies and offering an additional degree of freedom in information storage [1–3]. However, very few such materials exist in nature because the usual atomic-level mechanisms driving ferromagnetism and ferroelectricity are mutually exclusive [4]. Therefore, the route to obtain ferromagnetism by doping ferroelectric material with transition metal atoms has offered an alternative approach to achieve room temperature ferromagnetism in ferroelectric materials.

It is well known that the properties of nanocrystals are dependent not only on their chemical composition but also on their structure, shape, phase, and size. The preparation of nanocrystals such as nanorods, nanofibers, and nanotubes, etc., has attracted keen interest recently due to their potential applications in various fields of technology compared with their collective optical, magnetic, and electronic properties [5–8]. Barium titanate (BaTiO<sub>3</sub>) has been widely used in multilayer ceramic capacitors (MLCC) [9], chemical sensors, and nonvolatile memories [10], due to its attractive dielectric and ferroelectric characteristics. Various techniques have been developed to synthesize BaTiO<sub>3</sub>, such as electrospinning, sol-gel method, molten-salt route, and solvothermal technique. Up to date, BaTiO<sub>3</sub> crystals with different shapes, such as acicular particles, nanocubes, nanorods, nanowires, and nanofibers, have been obtained [11–15].

In our recent work, our group has successfully synthesized Fe-doped Na<sub>0.5</sub>Bi<sub>0.5</sub>TiO<sub>3</sub> with ferromagnetism at room temperature by a hydrothermal technique [16]. In this paper, we report the hydrothermal synthesis of Fe doped BaTiO<sub>3</sub> hexagonal crystals. We focus on the effect of Fe doping on the morphology of BaTiO<sub>3</sub> hexagonal crystals, which is significant in investigating the correlation between morphology and basic physical properties. Furthermore, the results presented in this paper would be important to widely explore multiferroic materials based on BaTiO<sub>3</sub> crystals. The concentration of Fe is designed as the molar ratio of Fe/(Fe + Ti) in the form of Fe<sup>3+</sup> ions.

### Experimental

The chemical reagents used in the work were bismuth nitrate (Ba(NO<sub>3</sub>)<sub>2</sub>), titanium (IV) sulfate [Ti(SO<sub>4</sub>)<sub>2</sub>], iron nitrate [Fe(NO<sub>3</sub>)<sub>3</sub>•9H<sub>2</sub>O] and potassium hydroxide (KOH). All the chemicals were analytical grade purity and were used as received without further purification. The hydrothermal

process included the following steps: 0.01 mol  $\text{Ti}(\text{SO}_4)_2$  and appropriate amount of  $\text{Fe}(\text{NO}_3)_3$  were dissolved in 30 ml diluted  $\text{HNO}_3$  (10%) to form aqueous solutions. Then,  $\text{KOH}$  solution was slowly added to the above solution to coprecipitate  $\text{Ti}^{4+}$  and  $\text{Fe}^{3+}$  ions by constant stirring and precipitate was formed. The precipitate was filtered, and washed with distilled water to remove  $\text{NO}_3^-$ ,  $\text{SO}_4^{2-}$  and  $\text{K}^+$  ions. Next, the fresh precipitate and equivalent amounts of  $\text{Ba}(\text{NO}_3)_2$  solution were transferred into the stainless-steel autoclave with  $\text{KOH}$  solution for the hydrothermal treatment. The autoclave was sealed and maintained at 200 °C for 6h. Finally, the autoclave was cooled down to room temperature naturally. The products were filtered, washed with distilled water and absolute ethanol for several times, and then dried at 90 °C for 4 h for characterization.

X-ray diffraction was performed on an X-ray diffractometer (D8 Focus, Germany) using  $\text{CuK}\alpha$  radiation. Transmission electron microscope (TEM) images were taken with a JEOL, 200CX TEM by using an acceleration voltage of 160 kV.

## Results and discussion

Fig. 1 exhibits the XRD patterns of the Fe doped  $\text{BaTiO}_3$  samples with different Fe doping concentrations prepared at 200 °C with 0.7M  $\text{KOH}$  concentration by the hydrothermal method. It could be observed that the as-prepared samples are pure phase, well consistent with a perovskite structure, and exclude from any impurities when Fe doping concentration increased from 0% to 10%. A careful comparison on the location of (110) diffraction peaks in the range of 30°–33° [exhibited in Fig.1(b)] reveals that the (110) diffraction peak has a clear shift toward a lower  $2\theta$  value when the Fe doping concentration increases, suggesting that Fe ions have incorporated into  $\text{BaTiO}_3$  host lattice and the lattice parameter  $a$  of  $\text{BaTiO}_3$  was enlarged because of larger radius of  $\text{Fe}^{3+}$  with respect to  $\text{Ti}^{4+}$ . No any iron oxide phase can be found from Fig. 1(a). Therefore, according to the above results, it is reasonable to consider that doped Fe ions have been effectively incorporated into the crystal structure of  $\text{BaTiO}_3$ . Fe doping does not affect the crystalline structure of the parent compound  $\text{BaTiO}_3$  which is important for preserving the ferroelectric properties in Fe-doped  $\text{BaTiO}_3$ .

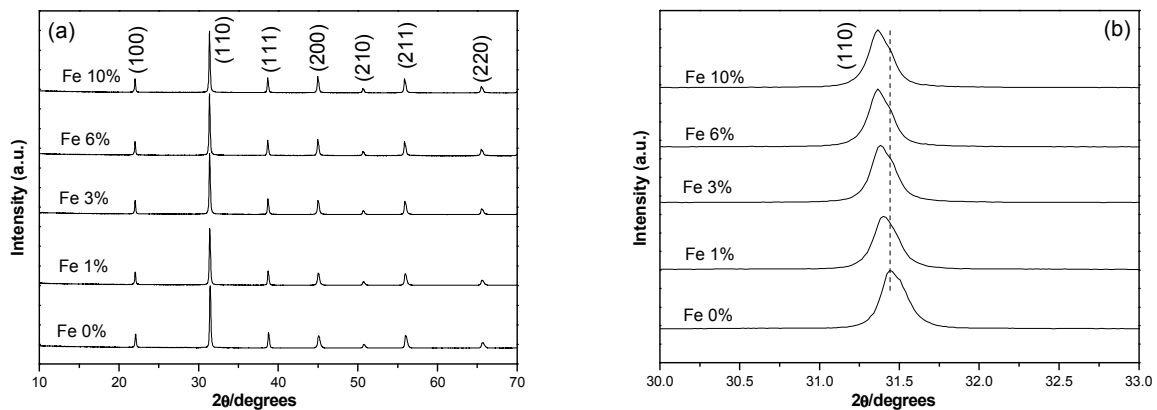


Fig.1 (a) XRD patterns of the as-obtained Fe doped  $\text{BaTiO}_3$  samples with different Fe doping concentration ranging from 0% to 10%, (b) a comparison of (110) diffraction peak positions for the patterns,

The morphology of the as-prepared Fe doped  $\text{BaTiO}_3$  samples were further examined with transmission electron microscope (TEM). A typical image of TEM for the pure  $\text{BaTiO}_3$  samples depicts that well-faceted hexagonal  $\text{BaTiO}_3$  crystals with symmetric corners were formed, and each corner possessed rod-like shape with a length of 200–250 nm and width of 80–120 nm. However, when the Fe doping concentration was increased from 0% to 1%, though the obtained Fe doped  $\text{BaTiO}_3$  crystals still presented hexagonal shape with six corners, the symmetry of six corners was decreased and the length and width of corners were decreased to 100nm and 50nm, respectively. When the Fe doping concentration was further increased from 1% to 3%, the morphology of the

obtained Fe doped  $\text{BaTiO}_3$  crystals changed from hexagonal shape to sphericity with corners, and the size of the ball-shaped crystals was further decreased. When the Fe doping concentration was further increased from 3% to 6% and 10%, crystals with ball shape were obtained, and the diameter of the crystals was further decreased to ca. 150nm. An obvious morphology evolution from hexagonal shape to sphere-like was observed according to the TEM results. The morphology and size variation of the Fe doped  $\text{BaTiO}_3$  crystals indicated that Fe ions have successfully incorporated into the lattice structure of  $\text{BaTiO}_3$  and have a pronounced effect on the crystallization and evolution of  $\text{BaTiO}_3$  crystallites, which is in a good agreement with the above XRD results.

The competition between crystal nucleation and crystal growth determines the size of the products during the hydrothermal process [17]. The crystal size will be small on condition that the rate of crystal nucleation is greater than that of crystal growth. We consider that the rate of crystal growth must be greater than that of crystal nucleation in the case of no addition of Fe, so the nuclei of  $\text{BaTiO}_3$  crystals could grow easily up. However, in the case of Ti sites substituted by Fe cations, the defects in the crystals structure increased inevitably, which might observably decrease the growing speed of  $\text{BaTiO}_3$  nuclei and the size of  $\text{BaTiO}_3$  particles were gradually decreased.

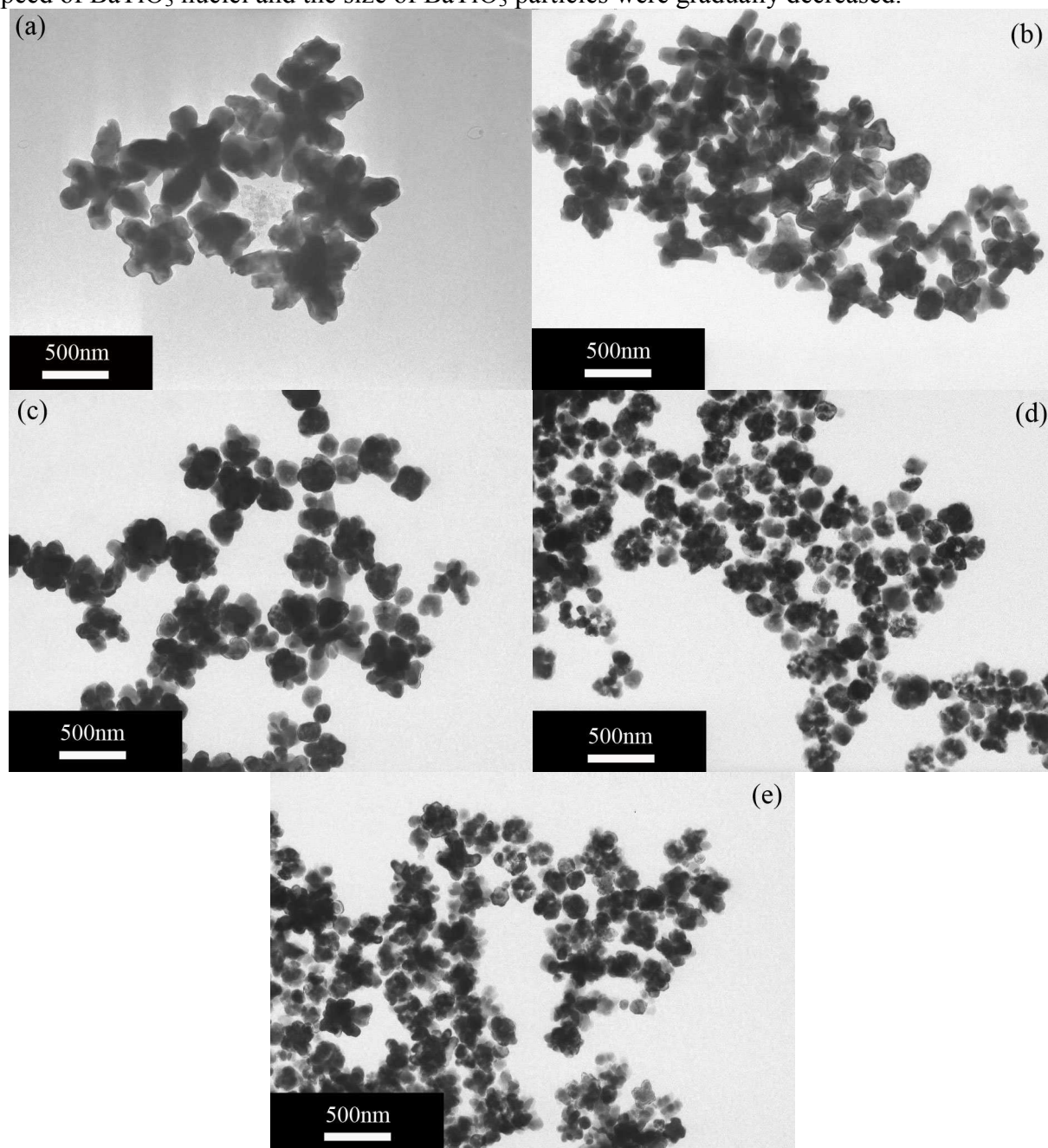


Fig.2 TEM images of the as-obtained Fe doped  $\text{BaTiO}_3$  samples with different Fe doping concentration (a)0%, (b)1%, (c)3%, (d)6%, and (e)10%.

## Conclusions

Fe doped BaTiO<sub>3</sub> hexagonal crystals without any impurities have been successfully synthesized by a hydrothermal method. When the Fe doping concentration increased from 0% to 10%, the morphology of the as-obtained crystals changed from hexagonal shape to sphericity, and the size of the as-prepared crystals became smaller. To obtain more single-phase multiferroic materials, the ferromagnetism and ferroelectricity of the Fe doped BaTiO<sub>3</sub> crystals needs to be further investigated, which will be reported elsewhere.

## Acknowledgment

This work is supported by the Doctor Foundation of Luoyang Institute of Science and Technology (2009BZ05).

## References

- [1] J. Dho, C.W. Leung, J.L. Driscoll, M.G. Blamire, *J. Cryst. Growth* Vol. 267 (2004), p.548.
- [2] T. Kimura, S. Kawamoto, I. Yamada, M. Azuma, M. Takano, Y. Tokura, *Phys. Rev. B* Vol. 67 (2003), p.180401.
- [3] W.M. Zhu, Z.G. Ye, *Ceram. Int.* Vol. 30 (2004), p.1435.
- [4] N.A. Spaldin, M. Fiebig, *Science* Vol. 309 (2005), p.391.
- [5] C. M. Lieber, *Solid State Commun* Vol. 107, (1998), p.607.
- [6] A. M. Morales and C. M. Lieber, *Science* Vol. 279, (1998), p.208.
- [7] X. F. Duan and C. M. Lieber, *Adv. Mater* Vol. 12 (2000), p.298.
- [8] Q. Y. Lu, F. Gao, and D. Y. Zhao, *Nanoletters* Vol. 2 (2002), p.725.
- [9] S. Ghosh, S. Dasgupta, A. Sen, H.S. Maiti, *Mater. Lett* Vol. 61 (2007), p.538.
- [10] S. Venigalla, *Am. Ceram. Soc. Bull* Vol. 6 (1999), p.45.
- [11] Y. Masuda, T. Yamada, K. Koumoto, *Cryst. Growth. Des* Vol. 8 (2008), p.1169.
- [12] J. Miao, C.G. Hu, H. Liu, Y.F. Xiong, *Mater. Lett* Vol. 62 (2008), p.235.
- [13] S.O. Kang, H.S. Jang, K.B. Kim, B. H. Park, M.J. Jung, Y. Kim et al, *Mater. Res. Bull* Vol. 43 (2008), p.996.
- [14] C.L. Jiang, K. Kiyofumi, Y.F. Wang, K. Koumoto, *Cryst. Growth. Des* Vol. 7 (2007), p.2713.
- [15] J.H. Yuh, L. Perez, W. M. Sigmund, J.C. Nino, *Physica E* Vol. 37 (2007), p.254.
- [16] Y.J. Wang, Y.G. Wang, Z. Shu, *Adv. Mater. Research* Vol. 284 (2011), p.2452.
- [17] Y.G. Wang, G. Xu, Z.H. Ren, X. Wei, W.J. Weng, P.Y. Du, G. Shen, G.R. Han, *Ceram Int* Vol. 34 (2008), p.1569.

## Polaron effect on the $D^-$ center at the InP(GaP) Heterointerface in a magnetic field

Xiao-yan Zhang<sup>1,a</sup> and Guo-liang Fan<sup>2,b</sup>

<sup>1</sup> Department of physics, Inner Mongolia University of Technology, Hohhot, 010051, China

<sup>2</sup> Department of physics, Inner Mongolia University, Hohhot, 010021, China

<sup>a</sup> xyzhang66@sina.com, <sup>b</sup> eeguoliangfan@sina.com

**Keywords:**  $D^-$  center, spin-triplet state, binding-energy

**Abstract.** Effect of polaron on the spin triplet state (p-like) of the  $D^-$  center is discussed by means of variational principle and second-order perturbation theory. Numerical results are produced for heterostructures of InP(GaP) in a magnetic field. We find that the polaron correction is very important. The contribution of the polaron is not negligible.

### Introduction

$D^-$  center in semiconductors is the solid-state analogs of  $H^-$  ion where two electrons are bound to a single positive charge. Recently, there has considerable interest in the two dimensional or quasi-two-dimensional  $D^-$  center [1-3], especially in the limit of a strong magnetic field. Although there have been great effects toward understanding the behavior of the  $D^-$  centers in quasi-two-dimension system, very little information is available concerning polaron effects on the properties of the  $D^-$  center in various wells. These effects were found to be important for a shallow donor in this system [4]. Because the binding energy of the  $D^-$  center is much smaller than that of a shallow donor, the relative contribution of the polaron correction is larger. In the photoconductivity measurement [5] for the  $D^-$  centers, the initial state is a bound bipolaron and the final state is a bound polaron and a free polaron, which means that in order to describe these experimental results, one needs knowledge of the polaron effects on the following systems [6-8].

In this paper, we report on a study of the  $D^-$  centers at the heterointerface of InP(GaP). The transition energies have been obtained as function of the magnetic field. In section of theory, we outline the theory used in this work. Our numerical results are summarized in section of results and discussion.

### Theory

We study the energy of a spin triplet state of the  $D^-$  center at the heterointerface (X-Y plane), and the magnetic field is applied parallel to Z axis (perpendicular to the X-Y plane), The Hamiltonian of this system interacting with interface-phonons, including the interface image potential, can be written as:

$$H = H_{D^-} + H_{ph} + H_{I1} + H_{I2} \quad (1)$$

Here

$$H_{D^-}(\vec{r}_1, \vec{r}_2) = H_0(\vec{r}_1) + H_0(\vec{r}_2) + \frac{e^2}{\epsilon|\vec{r}_1 - \vec{r}_2|} + V(z) H_0(\vec{r}_i) = \frac{\vec{p}_i^2}{2m^*} - \frac{e^2}{\epsilon r_i} + \frac{1}{8} m^* \omega_c r_i^2 + \frac{\hbar \omega_c}{2} L_{iz}$$

$$H_{ph} = \sum_q \hbar \omega_s a_q^+ a_q$$

$$H_{I1} = \sum_q [v_q \exp(-q|z_1| + i\vec{q} \cdot \vec{\rho}_1) a_q + h.c.]$$

(2)

$$H_{I_2} = \sum_q [v_q \exp(-q|z_2| + i\vec{q} \cdot \vec{\rho}_2) a_q + h.c.]$$

where  $H_{ph}$  is free phonon Hamiltonian.  $H_{I_1}$  and  $H_{I_2}$  are the interaction Hamiltonian of the electrons with the interface-phonons.  $\vec{q}$  is 2D wave vector of the interface-phonons.  $\vec{\rho}_1$  and  $\vec{\rho}_2$  are the 2D position vectors of the electrons while  $\vec{r}_1$  and  $\vec{r}_2$  the 3D ones

For simplified calculation, the potential is modeled by an infinite barrier potential and can be written as:

$$V(z) = \begin{cases} \infty & z < 0 \\ 0 & z > 0 \end{cases} \quad (3)$$

The electron-IO-phonon interaction constant is defined by

$$v_q = -i \left[ \frac{\pi \hbar \omega_s e^2}{\epsilon' S q} \right]^{1/2} \quad (4)$$

where  $\epsilon'$  is inversely proportional to the coupling constant and is defined by:

$$\frac{1}{\epsilon'} = \frac{2}{\epsilon_{\infty 1} + \epsilon_{\infty 2}} - \frac{2}{\epsilon_{01} + \epsilon_{02}} \quad (5)$$

$$\omega_s = \omega \left[ \frac{\epsilon_{\infty 1} (\epsilon_{01} + \epsilon_{02})}{\epsilon_{01} (\epsilon_{\infty 1} + \epsilon_{\infty 2})} \right]^{1/2} \quad (6)$$

$\epsilon_{01}(\epsilon_{02})$  and  $\epsilon_{\infty 1}(\epsilon_{\infty 2})$  are, respectively, the static and the high-frequency dielectric constants of crystal 1(2).

With the LLP intermediate coupling theory, the first unitary transformation can be chosen as:

$$U_1 = \exp \left[ -i \vec{r} \sum_q \vec{q} a_q^+ a_q \right] \quad (7)$$

The Hamiltonian can be transformed to be

$$\begin{aligned} H' &= U_1^+ H U_1 \\ &= H_{D^-} + \sum_q \left( \hbar \omega_s + \frac{\hbar^2 q^2}{2m} \right) a_q^+ a_q + \sum_{qj} \left[ v_{qj} \exp(-q|z_j|) a_q + h.c. \right] \end{aligned} \quad (8)$$

in which the two phonons term is neglected. The second transformation

$$U_2 = \exp \left[ \sum_{qj} (F_{qj} a_q^+ - F_{qj}^* a_q) \right] \quad (9)$$

brings  $H'$  to

$$\begin{aligned} H^* &= U_2^+ H' U_2 \\ &= H_{D^-} + \sum_{qj} \left( \hbar \omega_s + \frac{\hbar^2 q^2}{2m} \right) (a_q^+ + F_{qj}^*) (a_q + F_{qj}) + \sum_{qj} \left[ v_{qj} \exp(-q|z|) (a_q + F_{qj}) + h.c. \right] \end{aligned} \quad (10)$$

We now start with a variational method to calculate the triplet state energy of the negative donor. We confine ourselves on the zero phonon state (at the low temperature limit). The variational wave function is chosen as

$$|\Phi\rangle = |0\rangle |\Psi(\vec{r}_1, \vec{r}_2)\rangle \quad (11)$$

$|0\rangle$  is the phonon vacuum state, and  $|\Psi\rangle$  is the trial wave function for the donor state.

As an exact solution of the problem posed by Eq.1 is not possible, we have attempted a variational solution, using trial wave functions of the Chandrasekhar type.

$$\Psi(\vec{r}_1, \vec{r}_2) = \frac{1}{\sqrt{2}} [\varphi(\vec{r}_1) \varphi'(\vec{r}_2) - \varphi'(\vec{r}_1) \varphi(\vec{r}_2)] \quad (12)$$

where we adopt the following variational functions for an inner orbital  $\varphi(\vec{r})$  and outer orbital  $\varphi'(\vec{r})$ , according to the YKA approximation:

$$\varphi(\vec{r}) = \left( \frac{2^{-4}}{\pi a_{\perp}^2 a_{\parallel}^3} \right)^{1/2} z \exp \left( -\sqrt{\frac{\rho^2}{4a_{\perp}^2} + \frac{z^2}{4a_{\parallel}^2}} \right) \quad (13)$$

$$\varphi'(\vec{r}) = \left( \frac{2^{-6}}{3\pi a_{\perp}^4 a_{\parallel}^3} \right)^{1/2} z \rho e^{-i\varphi} \exp \left( -\sqrt{\frac{\rho^2}{4a_{\perp}^2} + \frac{z^2}{4a_{\parallel}^2}} \right) \quad (14)$$

where  $a_{\perp}, a_{\parallel}, a'_{\perp}, a'_{\parallel}$  are variational parameters.

The expectation value of the energy is given by

$$E'_{D^-} = \langle \Phi | H^* | \Phi \rangle = E_{D^-} + E_{I1} + E_{I2} \quad (15)$$

$$E_{Ij} = -\sum_q |v'_{qj}|^2 \left[ \hbar\omega_s + \frac{\hbar^2 q^2}{2m} \right]^{-1} \quad (16)$$

## Results and discussion

We have calculated the eigenenergy and the binding energy of the  $D^-$  ion at the heterointerface of InP(GaP) in magnetic fields.

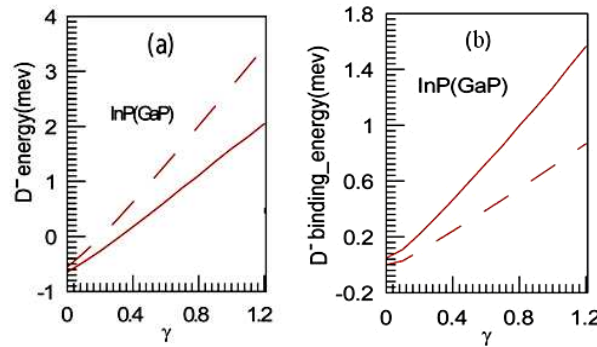


Fig. 1 The eigenenergy (a) and binding energy (b) of the  $D^-$  center at the heterointerface of InP(GaP) as functions of magnetic fields  $\gamma$  with electron-phonon interaction (solid line) and without electron-phonon interaction (dashed line).

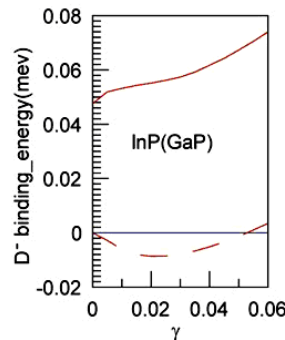


Fig. 2 The binding energy of the  $D^-$  center at the heterointerface of InP(GaP) as functions of magnetic fields  $\gamma$  with electron-phonon interaction (solid line) and without electron-phonon interaction (dashed line). ( $\gamma < 0.06$ )

The influences of the interaction of electron and phonon are obvious. From Fig.1 we can see that the electron-IO-phonon interaction plays an important role in the interface shallow donor states, and it brings down the eigenenergy and raises the binding energy of the  $D^-$  ion. The Fig.2 shows that the spin triplet-state of  $L = -1$  has been shown to form a binding state under the application of magnetic fields  $\gamma \sim 0.053$  without electron-phonon interaction. Owing to the interaction, in the zero magnetic

fields, the spin triplet-state of  $L = -1$  has also formed a binding state. Peeter's study [1] of polaron correction to the  $D^-$  center in a quantum well has also come to an analogous conclusion. For the spin triplet state of  $L = -2$ , it need stronger magnetic field to carry out the translation from non-binding state to binding state. The variational wave functions we adopted are not applicable. Using more elaborate variational wave functions, more theoretical work is necessary.

## References

- [1] J.M.Shi, F.M.Peeters and J.T.Devereese: Phys.Rev. B Vol.51(1995) , p. 7714-7724.
- [2] C.Tomo, N.Jun, and N.Akiko: Rev. B Vol.82(2010) , p. 195201-195210.
- [3] E. Reyes-Go'mez, L.E. Oliveira and M. de Dios-Leyva: Phys. Rev. B Vol.71 (2005) , p. 045316-045323.
- [4] X.Y.Zhang and X.Wang: INT J MOD PHYS B Vol.17 (2003) , p. 6097-6107.
- [5] A.B.Zzyubenko: Phys Lett A Vol.165 (1992) , p. 357-362
- [6] C.Sucismita and A. K. Bhattacharjee: Phys. Rev. B Vol.78 (2008) , p. 195311-195323.
- [7] R. Bardoux, A. Kaneta1, M. Funato1 et al.: Phys. Rev. B Vol.79 (2009) , p. 155307-155313.
- [8] D.M. Larsen: Phys.Rev.B Vol.70 (2004) , p. 085210-085216.

## Effect of Cellulose nanocrystal on Crystallization Behavior of Poly(3-hydroxybutyrate-co-3-hydroxyvalerate)

Houyong Yu<sup>1,a</sup>, Zongyi Qin<sup>1, b\*</sup>

<sup>1</sup>College of Materials Science and Engineering and State Key Laboratory for Modification of Chemical Fibers and Polymer Materials, Donghua University, Shanghai, 201620, China

<sup>a</sup>yuhouyong@mail.dhu.edu.cn, <sup>b</sup>phqin@dhu.edu.cn

**Keywords:** Poly(3-hydroxybutyrate-co-3-hydroxyvalerate), Cellulose Nanocrystals, Crystallization Behavior, Non-isothermal crystallization kinetics.

**Abstract.** The biodegradable nanocomposites of poly(3-hydroxybutyrate-co-3-hydroxyvalerate) (PHBV) with different cellulose nanocrystals (CNCs) contents were prepared by a solvent casting method. The effects of CNCs on the crystallization behavior of PHBV were studied by DSC. The DSC results showed that compared to PHBV, the melt crystallization temperature increased to 92.3 °C for the nanocomposites with 10 wt. % CNCs, which indicated that the crystallization of PHBV became easier with the addition of CNCs. Moreover, the non-isothermal crystallization kinetics study illustrated that overall crystallization rate of PHBV in the nanocomposites was faster than that of neat PHBV, which should be attributed to the strong heterogeneous nucleation of CNCs.

### Introduction

Among all kinds of biodegradable polymers, PHBV produced by a wide variety of bacteria as an intracellular reserve of carbon and energy has attracted much attention as an environmentally degradable resin since it has excellent biocompatibility and suitable physical properties. PHBV has more commercial potential applications to replace the petroleum-based synthetic polymers, and also can be used as various biomedical materials [1,2]. However, PHBV still exhibits several shortcomings to restrict its applications, such as slow crystallization rate, brittleness due to its big spherulites, and poor thermal stability [1]. In order to improve the rate of crystallization and also decrease the spherulitic sizes of PHBV, the effect of various seeding agents, including the organic and inorganic fillers [1-3], on crystallization behaviors, thermal and mechanical properties have been investigated extensively. Recently, more and more attention has been given to the fabrication and the property studies of polymer/CNC nanocomposites due to the high aspect ratio, nanosize in diameter, very low density, and the remarkably enhanced physical properties with a small amount of added CNCs [4-6]. However, to the best of our knowledge, the research on PHBV/CNC nanocomposites has rarely been a concern in the past investigations. In present paper, the effect of CNCs on the crystallization behavior of PHBV was studied in detail by using differential scanning calorimetry (DSC).

### Experimental

PHBV ( $M_n=5.90 \times 10^4$ ,  $M_w/M_n=3.18$ , and  $HV=2.6$  mol %) was supplied from Ningbo Tianan Biologic Material Co., Ltd (Ningbo, China). Commercial microcrystalline cellulose (MCC, particle size about 20  $\mu\text{m}$ ), chloroform (99.0%) and acetone (99.0%) were purchased from Guoyao Group Chemical Reagent CO., LTD. (Shanghai, China). Other reagents and solvents were used as received.

The CNCs were prepared by hydrolysis of 0.02 g/mL MCC in concentrated sulfuric acid at 50°C for 1 h, and the highly dispersed CNC suspension in chloroform (81 mg/mL) could be obtained by a solvent exchange procedure as our previous report [2]. Then PHBV was dissolved in the prepared chloroform suspension of CNCs at room temperature. The suspension of PHBV/CNC in chloroform was ultra-sonicated for 30 minutes and immediately casted on a clean glass plate. The resulting films

were obtained by solvent evaporation at room temperature and dried under vacuum at 40 °C. Different CNC contents of 1, 5, 10, and 20% (w/w) were used to prepare the nanocomposite films on the dry basis. The samples were denoted as PHBV/CNC1, PHBV/CNC5, PHBV/CNC10, and PHBV/CNC20, respectively.

The thermal behaviors of neat PHBV and its nanocomposites were characterized by a differential scanning calorimeter (MDSC TA-2910). About 10 mg of samples were first heated from room temperature to 200 °C at a rate of 20 °C/min and kept at 200 °C for 3 min to eliminate the previous heat history. Then the samples were subsequently cooled to 0 °C at 10 °C/min (the first cooling scan), and then heated to 200 °C (the second heating scan) at a rate of 10 °C/min. The thermal parameters were obtained from the first cooling trace and the second heating trace.

## Results and discussion

**Crystallization and melting behavior.** The first cooling and second heating DSC curves of neat PHBV and its nanocomposites are shown in Fig.1. The thermal parameters including melt crystallization temperature ( $T_{mc}$ ), melt crystallization enthalpies ( $\Delta H_{mc}$ ), melting temperature ( $T_{m1}$ ,  $T_{m2}$ ), melting enthalpies ( $\Delta H_{m2}$ ), cold crystallization temperature ( $T_{cc}$ ), and cold crystallization enthalpies ( $\Delta H_{cc}$ ) are listed in Table 1. In Fig.1 (a), the neat PHBV and PHBV/CNC1 did not show any obvious melt crystallization peaks during the cooling scans, whereas the cold crystallization peaks appeared in the second heating scans. With the increase of the CNC contents, the  $T_{mc}$  values shifted from 89.9 °C to maximum value of 92.3 °C, and then reduced to 57.4 °C for PHBV/CNC20. This result indicated that the crystallization of PHBV/CNC nanocomposites became easier probably because CNCs was an effective nucleation agent for PHBV crystallization. But high CNC contents will induce aggregations to depress nucleation effect for PHBV. As shown in Fig.1 (b), it is observed that the nanocomposites exhibited the double melting peaks ( $T_{m1}$ ,  $T_{m2}$ ) similar to the neat PHBV in the second heating process, which was caused by melting, recrystallization, and remelting during heating [1,2]. At lower melting temperature the less perfect and lower lamella thickness crystals melted, and then they reorganized to higher perfection and remelted at a higher temperature [2]. The double melting peaks of the nanocomposites were clearer than those of neat PHBV. The melting point from the higher temperature endothermic peak was taken as the true melting temperature [1,2]. As the CNC contents increased from 0 to 20wt.%, the melting temperature shifted from 130.7 to 168.3 °C, then decreased to 164.8 °C for PHBV/CNC20. The corresponding melting enthalpy reduced from 44.7 to 68.4 J/g, and then increased to 62.8 J/g, which illustrated that crystal perfection of the PHBV/CNC nanocomposites was improved. In addition, as shown in Fig.1 (b), it must be pointed out that obvious cold crystallization peaks of PHBV and PHBV/CNC1 appeared in the second heating scans. Compared to that of neat PHBV, a slight decrease in the cold crystallization temperature for PHBV/CNC1, but other nanocomposites did not show obvious cold crystallization peaks. This also indicated that the crystallization of PHBV became easier by incorporating well-dispersed CNC, even loading low CNC content (1wt.%).

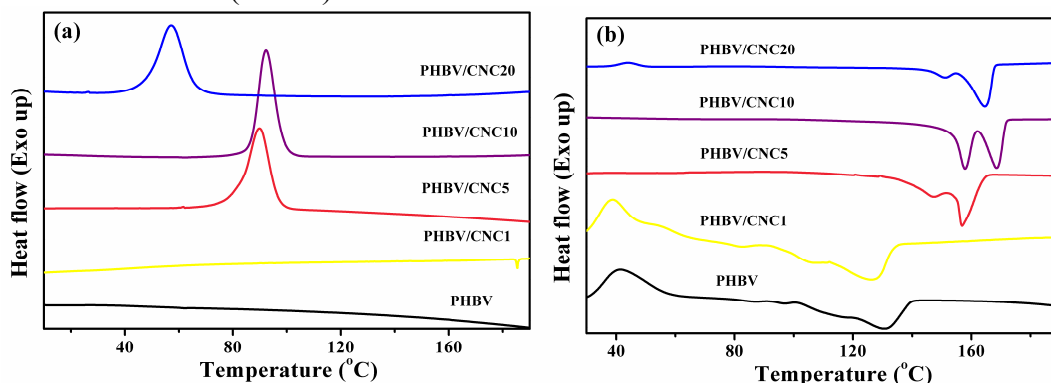


Fig.1 DSC curves of neat PHBV and its nanocomposites (a) first cooling scans; (b) second heating scans

Table 1 Thermal parameters of neat PHBV and its nanocomposites

Sample	First cooling		Second melting			
	T <sub>mc</sub> (°C)	ΔH <sub>mc</sub> (J/g)	T <sub>cc</sub> (°C)	T <sub>m1</sub> (°C)	T <sub>m2</sub> (°C)	ΔH <sub>m2</sub> (J/g)
PHBV	/	/	41.2	111.7	130.7	44.7
PHBV/CNC1	/	/	38.8	107.2	127.7	52.6
PHBV/CNC5	89.9	55.8	/	147.5	156.9	56.6
PHBV/ CNC10	92.3	58.9	/	157.8	168.3	68.4
PHBV/ CNC20	57.4	47.4	/	150.5	164.8	62.8

**Non-isothermal crystallization kinetics.** It is well known that the non-isothermal crystallization kinetic can be studied by Avrami equation, and the corresponding crystallization kinetic parameters can be calculated by following equations [3]:

$$1-X_t = \exp(-kt^n) \quad (1)$$

$$\log[-\ln(1-X_t)] = \log k + n \log t \quad (2)$$

$$t = \frac{T_0 - T}{\theta} \quad (3)$$

$$\log k_c = \frac{\log k}{\theta} \quad (4)$$

$$t_{0.5} = \left( \frac{\ln 2}{k_c} \right)^{1/n} \quad (5)$$

where  $X(t)$  is the relative crystallinity at time ( $t$ ),  $k$  is the crystallinity rate constant,  $n$  is the Avrami exponent,  $\theta$  is the cooling rate,  $k_c$  is corrected crystallinity rate constant (Jeziorny rate constant), and  $t_{0.5}$  is the half-life crystallization time.

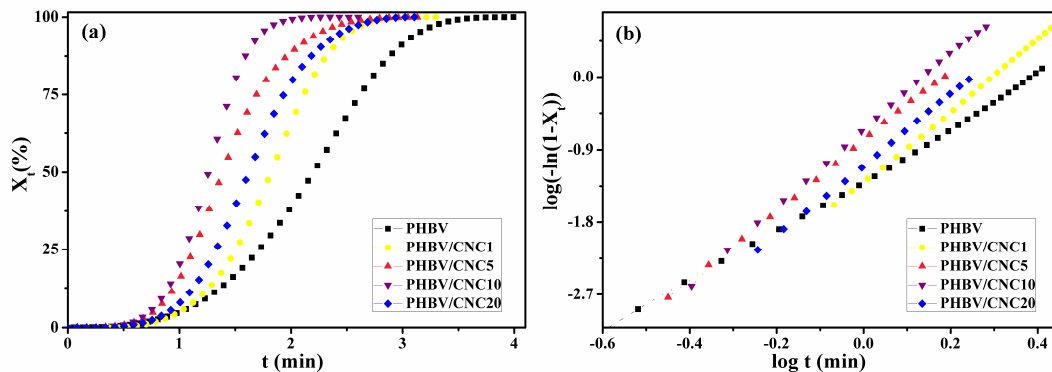


Fig.2 Plots of relative crystallinity (a) and the Avrami plots (b) versus crystallization time for neat PHBV and its nanocomposites at their crystallization temperatures

According to Eq. 1, Eq. 2 and Eq. 3, the plots of  $X_t$  and the Avrami plots versus crystallization time for PHBV and its nanocomposites at their crystallization temperatures are shown in Fig.2, respectively. It is observed that the time for completed crystallization of the nanocomposites was shorter than that for neat PHBV. It is clear that the addition of CNCs enhanced the non-isothermal melt crystallization of PHBV compared with neat PHBV; moreover, the CNC contents with 10 wt.% was more efficient in accelerating the crystallization process of PHBV than the other nanocomposites. The Avrami parameters of neat PHBV and its nanocomposites can be calculated through Eq. 4 and Eq. 5 and summarized in Table 2. It is found that the value of  $k$  and  $k_c$  for the PHBV/CNC nanocomposite was greater than that of PHBV, indicating that CNCs were efficient in enhancing the non-isothermal melt crystallization of PHBV. This result also suggested that the incorporation of CNCs can be used as the heterogeneous nucleation agent to accelerate the overall crystallization process of PHBV in the

nanocomposites as compared with neat PHBV. Furthermore, the values of  $t_{0.5}$  for the nanocomposites were smaller than those of neat PHBV at crystallization temperatures. With the CNC contents,  $t_{0.5}$  decreased from 0.986 to 0.954, and then increased to 0.970. Usually, the crystallization rate can also be easily described by the reciprocal of  $t_{0.5}$  [3]. Such variations indicated the overall crystallization rate of PHBV/CNC10 was the fastest among all the nanocomposites.

Table 2 Crystallization kinetic parameters for neat PHBV and its nanocomposites

Sample	n	$k$	$k_c$	$t_{0.5}$ (min)
PHBV	3.31	0.044	0.731	0.986
PHBV/CNC1	4.27	0.049	0.740	0.983
PHBV/CNC5	4.45	0.166	0.836	0.959
PHBV/ CNC10	4.65	0.224	0.861	0.954
PHBV/ CNC20	4.41	0.098	0.793	0.970

## Conclusions

A series of biodegradable PHBV/CNC nanocomposites with various CNC contents were fabricated with a solution casting method. From the DSC analysis, it can be found that with the CNC contents increased to 10 wt.%, the melting temperature shifted from 130.7 °C for neat PHBV to 168.3 °C for PHBV/CNC10, meanwhile the melt crystallization temperature increased to maximum value of 92.3 °C. This indicated that with the addition of CNC, the crystal perfection of the PHBV/CNC composites was improved and their crystallization became easier with the CNC contents. Further, non-isothermal crystallization kinetics study indicated that the presence of CNCs could accelerate the overall crystallization process of PHBV in the nanocomposites compared with that of neat PHBV, which should be attributed to the strong heterogeneous nucleation of CNCs.

## Acknowledgement

This work was financially supported by the Fundamental Research Funds for the Central Universities, and the Doctorate Innovation Foundation of Donghua University (BC201101).

## References

- [1] Q.S.Liu, M.F.Zhu, W.H.Wu et al.: Polymer Degradation and Stability Vol. 94(2009), p. 18–24.
- [2] Z.Zhou, H.Yu, M.Zhu, et al.: Advanced Materials Research Vol. 284–286(2011), p. 1778–1781.
- [3] A.Buzarovska, G.Bogoeva–Gaceva, A.Grozdanov et al.: Journal of Materials Science Vol. 42(2007), p. 6501–6509.
- [4] L.Jiang, E.Morelius, J.Zhang et al.: Journal of Composite Materials Vol. 42(2008), p. 2629–2645.
- [5] E.Ten, J.Turtle, D.Bahr et al.: Polymer Vol. 51(2010), p. 2652–2660.
- [6] Y.Habibi, L.A.Lucia and O.J.Rojas: Chemical Reviews Vol. 110(2010), p. 3315–3336.

# Preparation and Properties of a Novel Thermosetting Resin based on 4,4'-Bismaleimidodiphenyl Methane and Allyl COPNA Resin

Lei Xiong<sup>1,a</sup> and Qilang Lin<sup>1,b</sup>

<sup>1</sup> College of Materials Science and Engineering, Fuzhou University, Fuzhou 350108, PR China

<sup>a</sup>xionglei\_scut@163.com, <sup>b</sup>linqilang@fzu.edu.cn

**Keywords:** Thermosetting resin; Bismaleimide; Allyl; COPNA resin

**Abstract.** A bismaleimide (BMI) resin system based on allyl condensed polynuclear aromatic resin and 4,4'-bismaleimidodiphenyl methane was prepared in this paper. The chemical structures and rheological properties of the resin prepolymer were characterized by FTIR and viscometer, respectively. DSC was used to study the curing reaction of the resin prepolymer, and TG-DTG was employed to study the thermal behaviors of the cured resin. Moreover, physical properties of the BMI resin, including mechanical and dielectric properties, were studied. The results showed that the BMI resin had good thermo-stability, good mechanical properties and excellent dielectric properties.

## Introduction

The modern aerospace and aeronautic industry urgently needs matrix resin with excellent thermal and mechanical properties and good processing characteristics for advanced composites [1,2]. Bismaleimide (BMI) is one of the most important resins owing to its outstanding thermal properties [3]. The cured resin, however, is extremely brittle due to its high cross-linking density. Presently, one of the most desirable methods is the copolymerization of BMI with allyl compounds. Typical allyl compounds are *0,0'*-diallylbisphenol A, *0,0'*-diallylbisphenol A ether, allylated novolac and allylated xylok [4], which can react with BMI and thus decrease cross-linking density of modified resin [5]. Moreover, Phenyl groups in these allyl compounds can improve heat-resistant property of modified resin.

Condensed polynuclear aromatic (COPNA) resin is as a novel tape of heat-resistant resin [6], which is prepared from the dehydrating reaction of 1,4-benzenedimethanol and condensed aromatic compounds (e.g. anthracene, pyrene, phenanthrene or their mixtures, the pitch materials) under an acid catalysis [7]. COPNA resin has better heat-resistant property than novolac or xylok resin, due to its higher aromaticity. Presently, COPNA resin is often used in production of friction materials, carbon materials, and electronic packing materials for its excellent thermal, mechanical and dielectric properties [8,9]. In this article, we report a novel thermosetting resin system based on 4,4'-methylenediphenyl dimaleimide and allylated COPNA resin.

## Experimental

**Materials.** 4,4'-bismaleimidodiphenyl methane, m.p. 156-158 °C, was purchased from the Fenguang Chemical Co., Ltd. (Honghu, China). Allyl chloride was obtained from the Qilu Petrochemical Co, Ltd. (Zibo, China) and used after distillation. 1-naphthol (CP), p-toluenesulfonic acid (CP), n-butanol (CP) and 1,4-benzenedimethanol (CP) were all obtained from Shanghai Chemical Reagent Corporation (Shanghai, China).

**Preparation of BMI resin.** Allyl condensed polynuclear aromatic resin used was prepared according to the procedure described in our previous study [10], and a scheme for the preparation of allyl COPNA resin was illustrated in figure 1.

For the preparation of the BMI resin, 100 g allyl COPNA resin was heated to 130 °C in a three-necked round bottom glass flask equipped with a mechanical stirring device and thermometer, then 100 g 4,4'-bismaleimidodiphenyl methane was added under stirring and maintained between 120-140 °C until a clear homogeneous melt was obtained. The melt was maintained at 130 °C for additional 30 min, and the resultant liquid was defined as resin prepolymer.

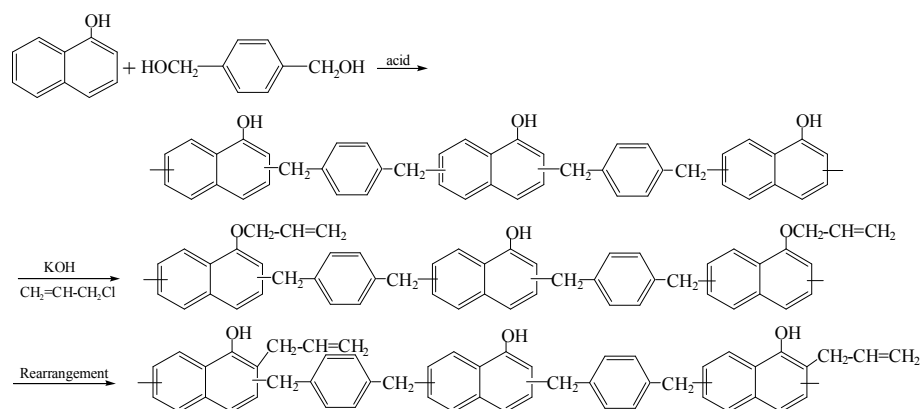


Fig.1 Preparation of the allyl COPNA resin

**Preparation of the specimens for mechanical testing.** The resin prepolymer obtained was degassed in a vacuum oven, and then cast into a steel mold. Curing was carried out by heating at 150 °C for 2 h, 180 °C for 2 h, 200 °C for 2 h, 230 °C for 2 h and 260 °C for 6 h. The specimens obtained were used for mechanical testing.

**Measurements.** FTIR spectra were recorded using the KBr tablet technique on a Nicolet-5700 FTIR spectrometer in the transmittance mode.

The thermal behavior of the resin prepolymers were studied by differential scanning calorimetric analysis (DSC) on a Mettler thermal analyzer.

The viscosity of the resin prepolymers was measured using a Brookfield DV III+ rotational viscometer with 53.57 rpm for apparent viscosity.

Thermal stability of samples was obtained with a Perkin-Elmer thermogravimetric analyzer with a heating rate of 10 °C/min in a nitrogen atmosphere.

Tensile and flexural data were obtained according to GB1451-1483 and GB3356-3382, respectively. In addition, impact strength was determined by GB1843-1880. Heat deflection temperature (HDT) was obtained by GB1634-1679 and density by GB 1033-1086. The value of water absorption was calculated according to ASTM D 570-81. The dielectric properties were measured according to GB1409-78 using wave-guide short circuit method.

## Results and discussion

**FTIR analysis.** FTIR spectra of the allyl COPNA resin and the prepolymer are shown in figure 2. In the FTIR spectrum of allyl COPNA resin, the peaks at  $920\text{ cm}^{-1}$  and  $1640\text{ cm}^{-1}$  confirm the presence of allyl groups [6]. In the FTIR spectrum of the prepolymer, there are no peaks at  $920\text{ cm}^{-1}$  and  $1640\text{ cm}^{-1}$ , revealing that the allyl groups participate in the copolymerization with 4,4'-bismaleimidodiphenyl methane. In addition, the peak at  $1712\text{ cm}^{-1}$  is attributed to carbonyl C=O stretching vibration of imide ring.

**DSC analysis.** DSC is used to establish a reasonable curing cycle for the resin system. Figure 3 shows DSC curves of the prepolymer at a series of heating rates (5, 10, 15, 20 and 25 °C/min). The initial temperature ( $T_i$ ), peak temperature ( $T_p$ ), and finish temperature ( $T_f$ ) are plotted against the heating rate. By extending the  $T-\beta$  curves to  $\beta=0$ , the reference temperatures  $T_i^0$  (178.05 °C),  $T_p^0$  (238.84 °C), and  $T_f^0$  (265.24 °C) are obtained. The results show that the resin system has higher  $T_p$  and  $T_f$ . Therefore, in order to obtain high crosslinking network, it is necessary to cure at some lower temperature for a longer time according to the time-temperature equivalence. We carry out a curing cycle for the resin system by heating at 150 °C for 2 h, 180 °C for 2 h, 200 °C for 2 h, 230 °C for 2 h and 260 °C for 6 h.

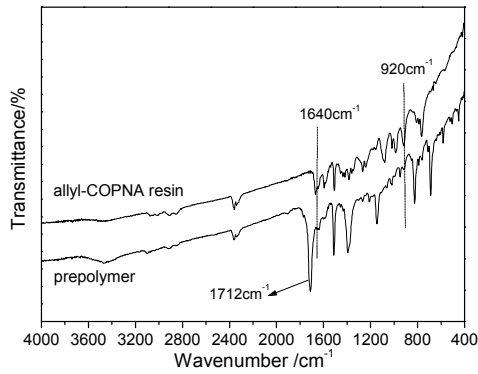


Fig.2 FTIR spectra of ally COPNA resin and prepolymer

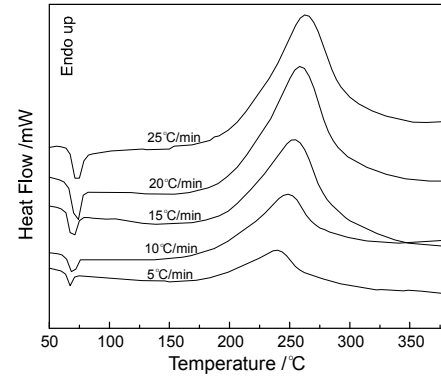


Fig.3 DSC curves of prepolymer

**Rheological properties of resin prepolymer.** Rheologic properties of thermosetting resin are principal parameters for processing. Figure 4 shows viscosity-time curves for the prepolymer over a range of temperatures, illustrating that the rate of cure increases with increasing temperature. The initial viscosity varies inversely with temperature before commencement of curing. Afterwards, the viscosity increases with increasing time at certain temperature, and the viscosity curves cross over due to the higher cure rate at higher temperature. The gel time of the prepolymer at different temperatures is shown in figure 5. It demonstrates longer pot life when held at lower temperature. At 120 °C, a working life of about 380 min is maintained. When the temperature is raised to 150 °C or 170 °C, it gels within 80 min or 40 min, respectively.

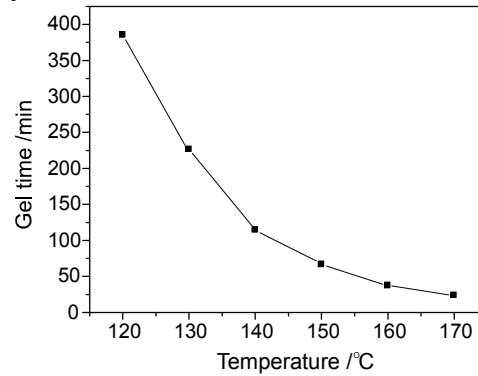
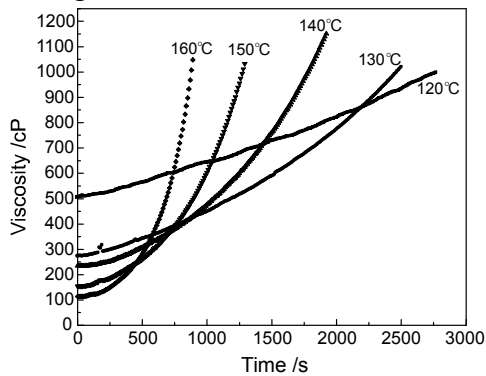


Fig.4 Viscosity-time curves of prepolymer

Fig.5 Gel time-temperature correlations of prepolymer

**TGA analysis.** The TG and DTG curves of allyl COPNA resin, prepolymer and cured resin are shown in figure 6. It can be seen from the figure that the prepolymer and cured resin have better thermo-stability than the allyl COPNA resin. Specially, for the formation of a highly cross-linked network, the cured resin exhibits very excellent thermo-stability, indicated by its initial weight loss temperature of 450 °C and char yield of 53.6% at 800 °C.

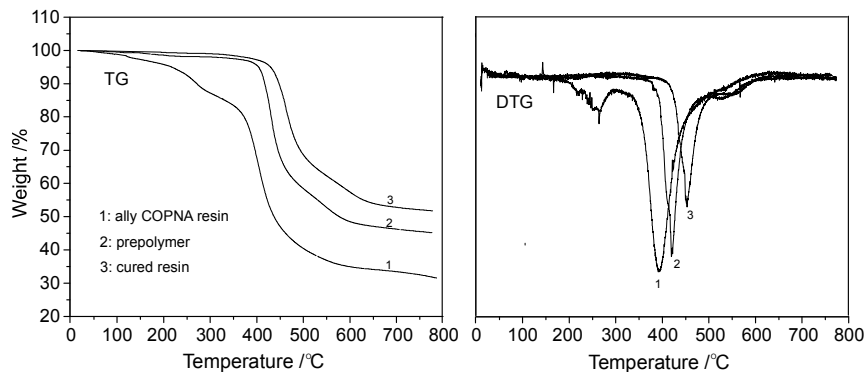


Fig.6 TG-DTG curves of allyl COPNA resin, prepolymer and cured resin

**Properties of the BMI resin.** The properties of the cured resin are shown in Table 1. The resin system has good mechanical properties. In particular, the flexural strength of the resin arrives at 155 MPa, which is higher than most of BMI resins. The reason for this is due to the existence of a great deal of rigid and large naphthyl groups. In addition, the cured resin possesses excellent thermal-stability, which may be attributed to the high aromatic backbone and the high cross-linking density of the BMI resin. Moreover, the BMI resin has good hot-wet resistance, indicated by the water absorption of 2.1%. Furthermore, the cured resin exhibits good dielectric properties, suggested by the dissipation factor of 0.013 and the dielectric constant of 3.16.

Table 1 Physical properties of the BMI resin

Property	Value	Property	Value
Tensile strength [Mpa]	76.8	T <sub>g</sub> [°C]	270
Tensile modulus [Gpa]	3.6	Specific gravity	1.2
Flexural strength [Mpa]	155	Water absorption	2.1
Impact strength [kJ/m <sup>2</sup> ]	11.3	Dissipation factor (1 MHz)	0.013
HDT [°C]	312	Dielectric constant (1 MHz)	3.16

## Conclusions

A novel thermosetting resin was obtained by the reaction of Allyl COPNA resin and BMI. The resin prepolymer has good rheological properties, and its curing reaction can be easily controlled. The cured resin has good thermo-stability. The initial decomposition temperature of the cured resin arrives at 450 °C and resultant char yield reaches 53.6% at 800 °C. Moreover, the cured resin possesses not only good mechanical properties but also excellent dielectric properties.

## Acknowledgements

The authors gratefully acknowledge financial support from the National Natural Science Foundation of China (No.50802015), the Natural Science Foundation of Fujian Province of China (No.2010J01280), the Science and Technology Development Foundation of Fuzhou University (No.0180-826827) and the Talent Foundation of Fuzhou University (No.0460-022213).

## References

- [1] G.Z. Liang, Z.P. Zhang, J.Y. Yang, X.L. Wang, BMI based composites with low dielectric loss, *Polym. Bull.* 59 (2007) 269-278
- [2] Y. Yao, T. Zhao, Y.Z. Yu, Novel thermosetting resin with a very high glass-transition temperature based on bismaleimide and allylated Novolac, *J. Appl. Polym. Sci.* 97 (2005) 443-448
- [3] A.J. Gu, G.Z. Liang, L.W. Lan, A high-performance bismaleimide resin with good processing characteristics, *J. Appl. Polym. Sci.* 62 (1996) 799-803
- [4] A.J. Gu, G.Z. Liang, L.W. Lan, Modification of polyaralkyl-phenolic resin and its copolymer with bismaleimide, *J. Appl. Polym. Sci.* 59 (1996) 975-979
- [5] H.F. Zheng, Z.H. Li, Y.M. Zhu, Bismaleimide modified by allyl novolak for superabrasives, *Chin. J. Chem. Eng.* 15 (2007) 302-304
- [6] K. Katsuki, G. Satoru, M. Shigeharu, Carbon molecular sieving membranes derived from condensed polynuclear aromatic (COPNA) resins for gas separations, *Ind. Eng. Chem. Res.* 37 (1998) 4262-4266
- [7] N. Kazunari, Development of flexible polymer blend films from advanced copna resin and nylon 6, *J. Appl. Polym. Sci.* 61 (1996) 1737-1746
- [8] S. Isamu, K. Kazuhisa, O. Yasushi, K. Masao, Tribological properties of COPNA resin, *Wear* 158 (1992) 171-183
- [9] A.F. Ismail, L.I.B. David, A review on the latest development of carbon membranes for gas separation, *J. Membr. Sci.* 193 (2001) 1-18
- [10] J.B. Zhao, Q.L. Lin, Y. Chen, Y.L. Ke, Synthesis and properties of allyl-COPNA resin, *Polym. Mater. Sci. Eng. (Chin.)* 24 (2008) 51-53

## First-principles Study of the Self-assembly Monolayer on Silicon (100) Surface

Liqui Shi<sup>1, a</sup>, Feng Yu<sup>1</sup>, Xiaoping Hu<sup>1</sup>, Xiaowen Li<sup>1</sup>, Tao Sun<sup>2, b</sup>, Shen Dong<sup>2</sup>

<sup>1</sup> Jiamusi University, Jiamusi 154007, China,

<sup>2</sup> Center for Precision Engineering, Harbin Institute of Technology, Harbin 150001

a. jmsdxshiliqiu@163.com (corresponding author), b. spm@hit.edu.cn

**Keywords:** First principles calculation, Aryl diazonium salts, Silicon (100), monolayer

**Abstract.** The first principles calculation based density functional theory has been employed to investigate the changes of energy, bonds length and bonds angle of aryldiazonium salt Self-assembly monolayer (SAMs) on silicon (100) surface. The steady structure and binding energy can be determined. It is shown that the partial bonds length and bonds angle have been changed obviously before and after self-assembly. The reduced energy of system is -101.95eV, i.e. binding energy, which is emitted energy of Si-C covalent bond coming into being, illuminates that the SAMs can be fabricated easily between aryldiazonium salt and Si (100) surface. The stability of system can be improved and SAMs can firmly stay on Si (100) surface.

### Introduction

The technology of using semiconductor materials silicon wafers as substrate to self-assemble organic functional monolayer is a very promising technology of micro-nano structure preparation. On account of order and high stability at normal temperature of this type of self-assembled monolayer, especially the functional monolayer obtained with nano-scale structures and interfacial properties, it is very popular with researchers. Therefore, it appears particularly important to study the changes of the silicon surface's molecular structure and energy before and after assembly monolayer in the micro-scale and thus to have a knowledge of SAMs' state of stable existence.

In recent years, the rapid development of theory and numerical algorithms makes the first-principles approach based on Density Functional Theory conventional computing research methods in condensed matter physics, quantum chemistry and material science. Calculated results not only can be used to explain the experimental results, but also may reliably predict many properties of materials and bring about some important discoveries of experiments under some circumstances. The theoretical study of the organic monolayer on silicon surface has been reported [8-10], but the calculation study of the self-assembly monolayer of aromatic diazonium salt on silicon surface has not been reported yet. From a theoretical perspective, this chapter adopts first-principles calculation to study assembly behavior of aromatics monolayer (C<sub>6</sub>H<sub>4</sub>NO<sub>2</sub>) prepared on silicon (100) surface based on mechanochemical method in the micro-scale.

### Analog computation

**Method of Calculation.** In accordance with Quantum Chemistry Density Functional Theory (DFT), CASTEP (Cambridge Sequential Total Energy Package) calculation module in Material Studio software of Accelry Company is used to conduct theoretical calculations, and functional adopts Generalized Gradient Approximation (GGA), local functional employs PBE (Perdew-Burke-Ernzerhof functional), Plane wave cutoff energy Ecut is set to 300eV.

**Model Building.** As a result of the excellent optical performance of Si (100) crystal surface, it is widely adopted in manufacture of electronic components. When conducting simulation calculation and mechanochemical experiments, the Si (100) crystal surface are studied in this paper. Si (100)

surface has two dangling bonds that are prone to reconstruct. At present, although the study of Si(100) surface is more, there is no consensus view of the concrete structure of its reconstruction surface. And experimental studies of low-energy electron diffraction (LEED) and He diffraction measurements suggest that Si(100) surface has three reconstructed forms at least in which Si(100)2×1 is the most important reconstruction way, in addition to c(4×2) and p(2×2). Si(100)2×1 reconstruction is that one is equal to 2 times of internal basis vector and the other one is equal to internal basis vector. Many results of theoretical study also demonstrated that Si(100)2×1 reconstruction surface is a more stable model of Si(100) surface reconstruction.

Calculation model establishment's conditions of Si(100) crystal surface: Si(100) section model adopted in the paper is Si(100)2×1 reconstruction surface model. Monocrystal silicon was cut along (100) direction, three Si atoms were adopted, the  $\sqrt{2} \times \sqrt{2}$  original cell was selected as the supercell and vacuum layer thickness is 15Å. In the supercell model that Si(100) lattice plane selected, 27 Si atoms were contained, and the surface contains 9 Si atoms, as is shown in Figure 1(a). This model is a ball-and-stick model (that is, a ball stands for an atom and a stick shows a band that links adjacent atoms). In x, y direction to extend them as needed, a series of simulation boxes in different sizes can be obtained.

Calculation model establishment's conditions of aromatic diazonium salt are that boron tetrafluoride aromatic diazonium salt is connected with the nitro (-NO<sub>2</sub>) on one end, carbon atoms' number of the skeleton is six, and its molecular formula is NO<sub>2</sub>C<sub>6</sub>H<sub>4</sub>N<sub>2</sub>BF<sub>4</sub> which includes two end groups: nitro (-NO<sub>2</sub>) and boron tetrafluoride diazo (-N<sub>2</sub>BF<sub>4</sub>). Thus, more flexible self-assembly can be conducted on the single crystalline silicon surface. As the diazo in the aromatic diazonium salt molecules is prone to take denitrification reaction in solution, what really reacts with the silicon surface in solution is the benzene ring NO<sub>2</sub>C<sub>6</sub>H<sub>4</sub> with nitro connected at one end after breaking triple bond between nitrogen and nitrogen. On account of the calculation software limitations, it is advisable to directly establish the nitro benzene (C<sub>6</sub>H<sub>4</sub>NO<sub>2</sub>) with nitro connected at one end after breaking triple bond between nitrogen and nitrogen when the model is built, as is shown in Figure 1(b). This model is a ball-and-stick model (that is, a ball stands for an atom and a stick shows a band that links adjacent atoms), in Figure 1(b), the gray ball is C atom, the red ball is O atom, and the white ball is H atom.

Model selection of calculating the interaction between C<sub>6</sub>H<sub>4</sub>NO<sub>2</sub> and Si(100) crystal face: middle silicon atoms are selected on the Si(100) crystal face with the structural optimization completed, and then the optimization molecules are rooted in its top.

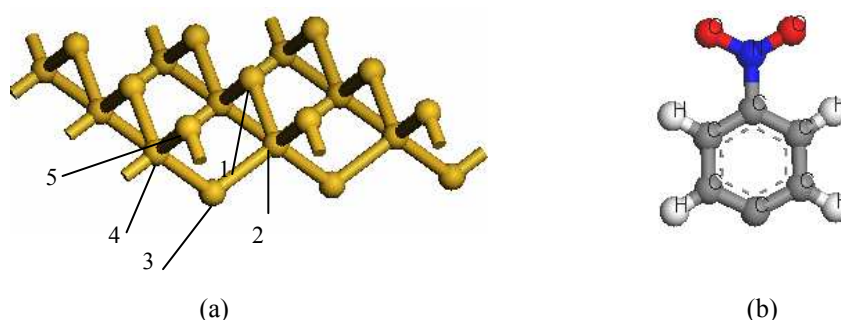


Fig.1 The side views of (a) single crystalline silicon (100) plane and (b) NO<sub>2</sub>C<sub>6</sub>H<sub>4</sub>

Middle silicon atoms are selected on the Si(100) crystal face with the structural optimization completed, and then the two optimization molecules are rooted in its top, and the distance between Si and the benzene ring is about 2.000 Å. As needed, different surface coverage can be obtained by controlling the number of replaced aromatic molecules, due to the limitations of analog computer operation conditions, self-assembly of a single aromatic molecule and silicon surface is selected for the study during the calculation. Finally, the basic unit of the model has been shown in Figure 2-6, the

model includes three layers of Si atoms. In order to improve calculation speed, the following two silicon atoms is fixed when Si(100) crystal plane model calculations and self-assembly aromatic molecule calculations are conducted.

## Results and discussions

**Structural Optimization.** Figure 2 is a side view and a top view of Si(100) crystal surface absorbing an active molecule before and after geometry optimization. Table 1 is the bond angle and bond length data of partial silicon atoms, respectively before and after optimization, and after combining an active molecule  $C_6H_4NO_2$  of the Si(100) crystal surface. It is inferred in accordance with structure theory that each Si in  $sp^3$  hybrid orbitals forms tetrahedral spatial structure in conjunction with the other four Si atoms, Si-Si bond length  $d=2.352\text{\AA}$ , Si-Si-Si bond angle  $109.471^\circ$ . When the crystal is cut along a certain direction to obtain different surfaces, the surface atomic structure of crystals is significantly different from the internal atomic structure, the reason is that each atom in a solid contributes the same number of electrons and forms chemical bonds with the other atoms around, thus to combine atoms together in a solid. However, the atoms on the surface of the solid have extra unpaired valence electrons to form dangling bonds because chemical bonds of one side's atoms are cut off, leading to the difference between the surface structure and the internal structure of crystals. It is acknowledged from Table 1 that the data of bond lengths and bond angles has changed after structural optimization and its data differs from the theoretical values.

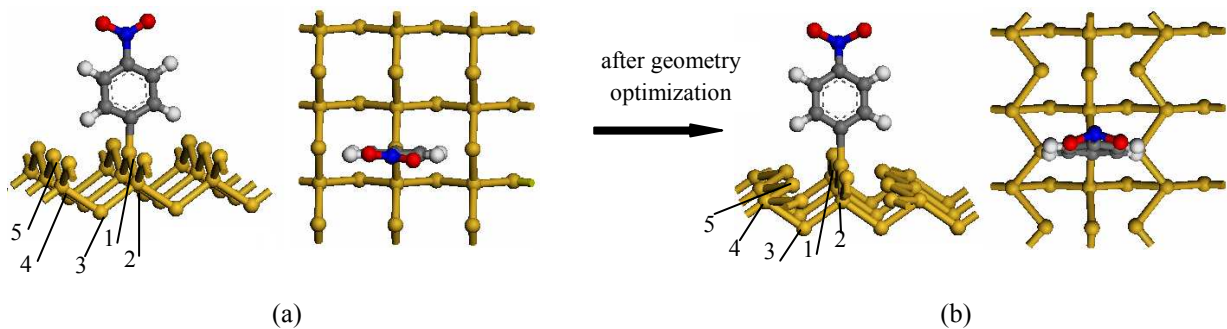


Fig.2 The three views of  $C_6H_4NO_2/Si(100)$  a) before and b) after geometry optimization

Table1 The bond length and angle of Si (100) before/after absorbing  $C_6H_4NO_2$

Planes	bond length (nm)			bond angle ( $^\circ$ )	
	$d_{1-2}$	$d_{2-3}, d_{3-4}$	$d_{4-5}$	$\angle 123$	$\angle 345$
(100)before optimization	0.233	0.233	0.233	109.471	109.471
(100) after optimization	0.232	0.233	0.231	109.203	109.202
(100)- $C_6H_4NO_2$	0.239	0.233	0.253	111.428	63.204

**Absorption Energy Calculation.** Table 2 is total energies of Si (100) crystal surface before and after combining a  $C_6H_4NO_2$ . As a result of the formation of new chemical bonds, the energy of Si atom combining a  $C_6H_4NO_2$  with becomes lower. Absorption Energy can be used to express the size of energy reducing. When the absorption energy value is negative, it shows releasing energy, and the stability of the system increases. The smaller the absorption energy is, the more energy decreases before and after reaction, and it is in more favor of reaction. The total energy of the system reduces after combining a  $C_6H_4NO_2$ , the reduced value is the energy that is released from the formation of

Si-C chemical bond, that is, the absorption energy is -101.95eV, which indicates that the aromatic diazonium salt monolayer can be assembled on (100) plane, the stability of the system increases after self-assembly.

Table 2 Total energies and the absorption energy of a C<sub>6</sub>H<sub>4</sub>NO<sub>2</sub> adsorbed on Si (100) (eV)

Planes	Energy/eV	absorption energy /eV
Si(100)	-2899.48	
Si(100)- C <sub>6</sub> H <sub>4</sub> NO <sub>2</sub>	-5052.53	-101.95

Table 2 reveals that the effect of forming SAMs is not fine as the sample has been immediately taken out from testing box after scribe and the surface content of C1s has a small quantity of augment after rinsing with acetone, anhydrous ethanol and milli-Q water. The content of C1s has been enhanced remarkably with the prolonged assembly time, at the same time, the total trend of the content of O1s descends because the sample has a chance to contact oxygen in the process of cutting and after cutting. The content of Si2p takes on a degressive trend on account of the surface covered with SAMs molecules and the fresh scribed silicon give an impact to it simultaneity. In a word, the assembly time about 12 h will form better films.

## Conclusions

The first principles calculation has been employed to investigate the changes of bonds length, bonds angle and energy before and after self-assembly of silicon (100) surface and aryldiazonium salt. Bonds length and bonds angle between Si atoms have been changed before and after self-assembly, which results from the introduced benzene ring with nitro, the sizes of these changes are factors influence whether self-assembly reacts from the perspective of energy. The total energy of the system reduces after combining a C<sub>6</sub>H<sub>4</sub>NO<sub>2</sub>, the reduced value is the energy that is released from the formation of Si-C chemical bond, that is, the absorption energy is -101.95eV, which indicates that the aromatic diazonium salt monolayer can be assembled on (100) plane, the stability of the system increases after self-assembly, and the stability of the film is better.

## Acknowledgement

It is a project supported by the Colleges and Universities in Heilongjiang Province in 2010 the Backbone of Support for Youth Program (1155G54).

## References

- [1] P.Wagner, S.Nock and J. A.Spudich: J. Struc. Bio Vol. 119 (1997), p.189
- [2] V.Dusastre: Nature Vol. 406 (2000), p.31
- [3] A. W. Brent, J. M.Michael and A. M. Ian: Appl. Phys. Lett Vol. 82 (2003), p. 808
- [4] G. P. Lopinski, D. D. M.Wayner and R. A.Wolkow: Nature Vol. 406 (2000), p.48
- [5] A. B. Sieval, R.Opitz and H. P. A.Maas : Langmuir Vol. 16 (2000), p. 5688
- [6] L. Zhang, A. J.Carman and S. M. Casey: J. Phys. Chem Vol. 107 (2003), p. 8424
- [7] Z. G. Wei, H. X.Zhang and Q. S. Li: Chem J Chinese U Vol. 29 (2008), p.824
- [8] L. N. Travis, G. L.Jiang and Y. L. Yit: Langmuir Vol. 17 (2001), p.5889
- [9] Y. L. Yit, L. N.Travis and M. Reija: Langmuir Vol. 18(2002), p. 4840
- [10] Y. L. Yit, J. F.Jonathan and Y. Li: J. Am. Chem. Soc Vol. 127 (2005), p. 2093

# Li<sup>+</sup> Extraction/Insertion Reaction with MgMn<sub>0.5</sub>Ti<sub>0.5</sub>O<sub>3</sub> Spinel in the Aqueous Phase

Jinhe Jiang

Department of Chemical Engineering, Weifang University 261061, China

Jiangjinhe2012@126.com

**Keywords:** Extraction/insertion reaction, Inverse Spinel-type metal oxides, Ion-exchange mechanism, MgMn<sub>0.5</sub>Ti<sub>0.5</sub>O<sub>3</sub>

**Abstract.** Inverse spinel-type metal oxides, magnesium-manganese-titanium oxide(MgMn<sub>0.5</sub>Ti<sub>0.5</sub>O<sub>3</sub>), was prepared by a coprecipitation/thermal crystallization method. The extraction/insertion reaction with this material was investigation by X-ray, saturation capacity of exchange, and K<sub>d</sub> measurement. The acid treatments of MgMn<sub>0.5</sub>Ti<sub>0.5</sub>O<sub>3</sub> caused Mg<sup>2+</sup> extractions of more than 82%, while the dissolutions of Mn<sup>4+</sup> and Ti<sup>4+</sup> were less than 15%.The experimental results have proved that the acid-treated sample has a capacity of exchange 7.6 mmol·g<sup>-1</sup> for Li<sup>+</sup> in the solution.

## Introduction

The inorganic ion-exchange preparation has the advantage of thermo-stability and radiation resistance, synthesis simple and good selectivity etc. Apart from that, it appears the fine speciality in dealing with nuclear waste, gathering and separating of metal ions and chromatogram analysis[1-2].

In this paper, the coprecipitation/thermal crystallization method was used to synthesize the MgMn<sub>0.5</sub>Ti<sub>0.5</sub>O<sub>3</sub> of spinel-type oxide, whose composition and structure are different from those in literature[3-4], The experimental result have proved that the inorganic material has better selectivity and higher capacity of exchange for Li<sup>+</sup> in the solution removed Li<sup>+</sup> previously. Moreover, the cost is cheap and its application prospect is significant.

## Experimental section

**Reagent and Instruments.** MgSO<sub>4</sub>, MnSO<sub>4</sub> and Ti(SO<sub>4</sub>)<sub>2</sub> were all analytical reagents; pure water; D/max-A type X-ray diffraction instrument; Dx-170 type ion chromatogram instrument; AA-670 atom absorption spectrum instrument; Centrifuge 5804 centrifugal separation instrument.

**Synthesis and Identifiable of MgMn<sub>0.5</sub>Ti<sub>0.5</sub>O<sub>3</sub>.** The ammonia was dropped into a standard mixed solution of MgSO<sub>4</sub>, MnSO<sub>4</sub> and Ti(SO<sub>4</sub>)<sub>2</sub> with a Mg/Mn/Ti mole ration of 1:0.5:0.5 at the condition of constant rate churning. After the pH of mother solution reached 11.0, a H<sub>2</sub>O<sub>2</sub> solution was added to the solution to oxidize Mn<sup>2+</sup> to Mn<sup>4+</sup> completely. After reacting fully, centrifugal separating and washing water, the Mg-Mn-Ti coprecipitation was obtained. The coprecipitation was coprecipitated for few hours on electric heating plate, air-dried for 48h at 72°C and crushed. Then the exchanger precursor obtained. The precursor was heat-treated for 4h at 700°C, 800°C, 900°C and 95°C respectively to obtain the Mg-Mn-Ti oxide, whose theoretical formula was MgMn<sub>0.5</sub>Ti<sub>0.5</sub>O<sub>3</sub>, the sample obtained by thermal crystallization treatment of 900°C was designed as MgMnTi-900. Then it was analysed of x-ray diffraction and compared to literature[3].

Composition analysis: A 0.2g portion of sample(MgMnTi-900) was dissolved with acid. The Mg, Mn and Ti contents were determined by atomic absorption spectrometry. The Mn valence was determined by the method in the literature[3] and the MgMnTi-900 composition was calculated from these values.

**The Cation Extraction of MgMnTi Oxide and Acid Modification.** Four 0.200g portions of sample (MgMnTi-900 oxides) were immersed in a HNO<sub>3</sub> solution (50ml) of 0.01M, 0.1M, 1M and 10M respectively with shaking in constant temperature water at 25°C. After 3 days, take the supernatant solution to determine the cation concentration, test its acid proof ability and the extraction ration of Mg<sup>2+</sup>, Mn<sup>4+</sup>, Ti<sup>2+</sup>.

A 5g portion of sample (MgMnTi-900) was immersed in a 1M HNO<sub>3</sub> solution (500mL) with intermittent shaking in constant temperature water at 25°C. After 7 days, remove the supernatant solution and add new HNO<sub>3</sub> solution. Repeating that for twice, then the initial sample was transformed to H-type sample, washed with water and air-dried. The sample obtained by thermal crystallized at 900°C and acid modified was designated as MgMnTi-900 (H), X-ray diffraction was carried out to compare their stabilization of structure. The composition was determined by the method referred in 1.2, and the H content was calculated by subtraction method.

**Saturation Capacity of Exchange.** Weigh five 0.5g portions of MgMnTi-900(H), then each portion was immersed in a 0.1M solution (10mL), containing Li<sup>+</sup>, Na<sup>+</sup>, K<sup>+</sup>, Rb<sup>+</sup> and Cs<sup>+</sup> respectively, diluted to 100mL, shaken in constant temperature water at 25°C. After saturation exchanging (namely, after 10 days by literature[9,13,15]) the solutions were filtered by subminiature aperture sieve, and the cation concentration was determined. At the same time, do vacant experiment. Last, the inorganic exchanger saturation capacity of exchange for alkali-metal-ions obtained by decrease quantity.

**Distribution Coefficient (Kd).** After weighing four 0.100g portions of MgMnTi-900(H), each portion of sample was immersed in a 0.05M mixed solution (0.200mL) containing Li<sup>+</sup>, Na<sup>+</sup>, K<sup>+</sup>, Rb<sup>+</sup> and Cs<sup>+</sup> (Cl<sup>-</sup>/OH<sup>-</sup> ratios are different in each solution, C(Cl<sup>-</sup>)+C(OH<sup>-</sup>)=0.1M, C= Li<sup>+</sup>, Na<sup>+</sup>, K<sup>+</sup>, Rb<sup>+</sup> and Cs<sup>+</sup>). The alkali-metals ions total concentration all was 1.0×10<sup>-3</sup>M by adding 9mL distilled water. After the samples were shaken for 7 days in constant temperature water at 25°C and were filtered, cation concentrations in each samples were obtained.

## Results and Discussion

**Compound and Appraisalment of MgMn<sub>0.5</sub>Ti<sub>0.5</sub>O<sub>3</sub>.** The X-ray diffraction pattern of compound metal oxide (MgMn<sub>0.5</sub>Ti<sub>0.5</sub>O<sub>3</sub>), crystallized at different temperatures, was shown in figure 1. The pure spinel-type phase is formed in a temperature range between 700°C and 950°C. The diffraction peaks become higher and sharper with an increase in the temperature. The structure of compound metal oxide MgMn<sub>0.5</sub>Ti<sub>0.5</sub>O<sub>3</sub> crystallized at 900°C was much perfect.

We know from chemical analysis, the composition of MgMnTi-900 is Mg<sub>1.20</sub>Mn<sub>0.51</sub>Ti<sub>0.49</sub>O<sub>3.20</sub>, whose chemical component is basically corresponded with the composition of spinel-type metal oxides.

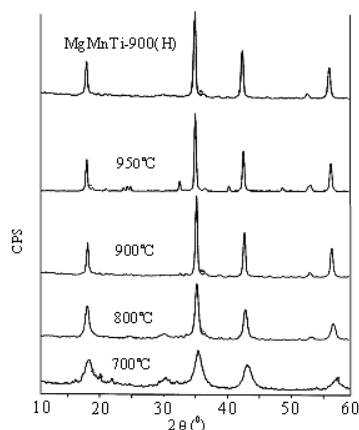


Fig.1 The powder's X-ray figures of different crystal temperatures

**Cation Extraction of Compound Oxide MgMnTi and Acid Modification.** The extraction ration of Mg<sup>2+</sup>, Mn<sup>4+</sup> and Ti<sup>4+</sup> from MgMnTi-900 in different concentration HNO<sub>3</sub> solution is shown in figure 2. we know from figure 2, the extractabilities of Mg<sup>2+</sup> are 41%~82%, Mn<sup>4+</sup> are 6.9%~

15.8%, and  $\text{Ti}^{4+}$  are 2.4%~8.2%. Those indicate that the extractabilities of  $\text{Mg}^{2+}$  are higher than those of  $\text{Mn}^{4+}$  and  $\text{Ti}^{4+}$  when exchanger was immersed in 1M acid solution, corresponding with the exchanger condition was better. (1N,  $\text{Mg}^{2+}$  74%,  $\text{Mn}^{4+}$  10.2%,  $\text{Ti}^{4+}$  6.2%)

X-ray diffraction of  $\text{MgMnTi-900(H)}$ , which is the acid modification product, is shown in figure 1. As shown, the structure of  $\text{MgMnTi-900(H)}$  is nearly constant, which is inverse spinel oxide type too. It indicate that the exchanger is steady. The analysis indicate the composition of  $\text{MgMnTi-900(H)}$  was  $\text{H}_{1.43}\text{Mg}_{0.24}\text{Mn}_{0.49}\text{Ti}_{0.48}\text{O}_{3.24}$ , whose component of 72%  $\text{Mg}^{2+}$  transformed to  $\text{H}^+$  compared with the composition  $\text{Mg}_{1.20}\text{Mn}_{0.51}\text{Ti}_{0.49}\text{O}_{3.20}$  before acid-treated. Then the specific  $\text{Mg}^{2+}$  of exchanger were extracted fulfill basically and remained the H-type identified with initial type.

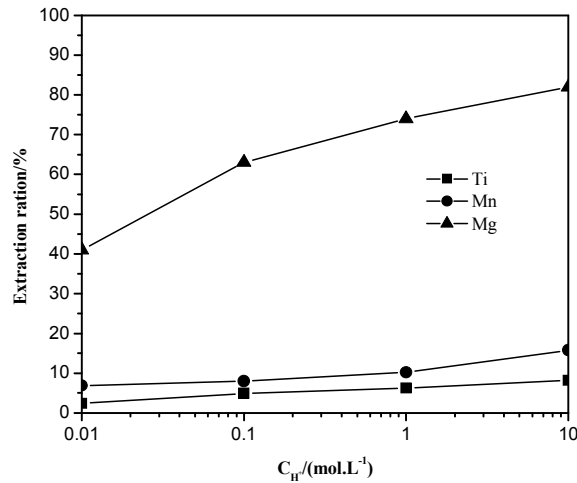


Fig.2 Extraction ratio of cations from  $\text{MgMnTi-900}$  in nitric acid solution

**Saturation Capacity of Exchange.** The relation between radius and saturated ion exchange capacity of  $\text{MgMnTi-900(H)}$  for alkali was shown in figure 3. Known from figure 3, the capacity of exchange for  $\text{Li}^+$  was much higher than those for other alkali ions. The capacity for  $\text{Li}^+$  is  $7.6 \text{ mmol} \cdot \text{g}^{-1}$ , which is much higher than the register of literature [9,12-15]. It proved that the ion exchange synthesized has higher capacity of exchange, and better remembering of exchange for  $\text{Li}^+$ . The effect factors of saturation capacity of exchange of  $\text{MgMnTi-900(H)}$  are: 1) The  $\text{Mg}^{2+}$  in exchange solution must be removed previously, because  $\text{Mg}^{2+}$  exchange with exchanger vacancy site when existing too much  $\text{Mg}^{2+}$ ; 2) The experimental results shown that the exchange capacity of ion exchanger for  $\text{Li}^+$  is much higher than those for other alkali ions in thin solution, which indicate that the ion-exchange reaction is carried out between and bare ions. That verified that the bare ions diameter of  $\text{Mg}^{2+}$  is nearly close to that of  $\text{Li}^+$ ; 3) At the time of exchange, a  $\text{Mg}^{2+}$  was replaced by one  $\text{H}^+$ .  $\text{Li}^+$  not only entered the vacancy site of  $\text{Mg}^{2+}$  but also exchange with the  $\text{H}^+$  of surface. Therefore,  $\text{MgMnTi-900(H)}$  has a higher exchange capacity for  $\text{Li}^+$ .

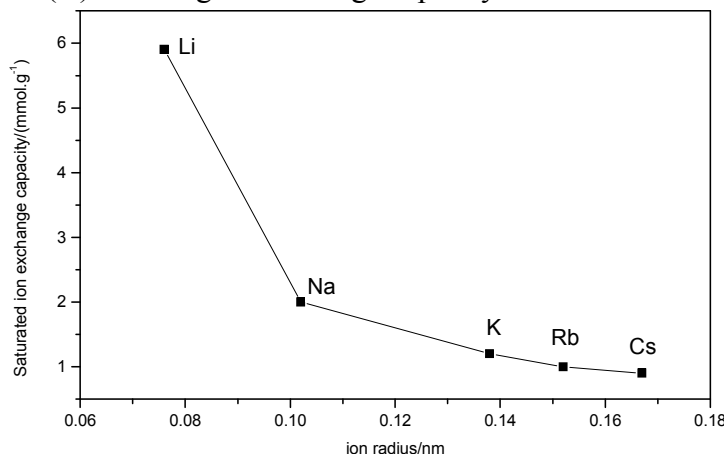


Fig.3 Relation between ion radius and saturated ion exchange capacity of  $\text{MgMnTi-900(H)}$  for alkali ions

**Distribution coefficient(Kd).** Kd values can be the token of exchange selectivity of MgMnTi-900(H) for correlate ions. Shown in figure 4, Kd values of MgMnTi-900(H) for alkali ions are larger and larger with an increase pH over the pH region studied. The selectivity sequence of MgMnTi-900(H) for alkali metal ions as follows:



It indicates that MgMnTi-900(H) has a better ion selectivity for  $Li^+$ . Ion-exchange reaction is reversible reaction. The reaction of  $H^+$  in ion-exchanger with alkali metal ions in solution as follows(example for  $Li^+$ ):

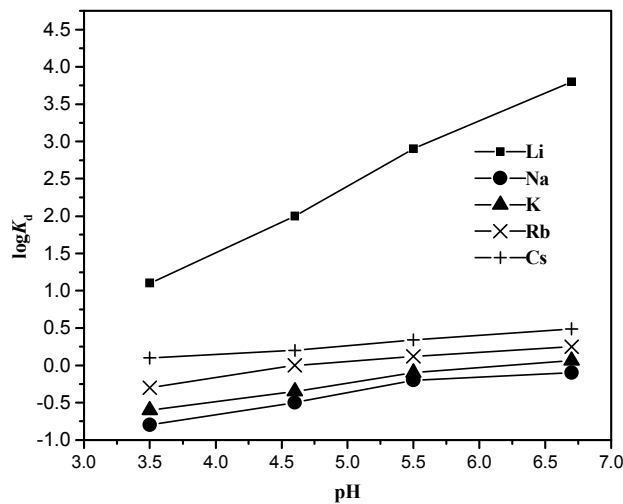


Fig.4 Distribution coefficient of MgMnTi-900(H) for alkali ions

## Conclusions

The comprehensive results indicate that the  $MgMn_{0.5}Ti_{0.5}O_3$  of inverse spinel-type metal oxide show a capacity extraction/insertion of  $Li^+$  in the aqueous phase, mainly by an ion-exchange mechanism. The  $Li^+$ -extracted samples show a high selectivity and a large capacity for  $Li^+$  among alkali metal ions.

## References

- [1] J.H.Jang, D.Q.Dong, G.H.Cheng, J.Q.Liu, J.Li:  $Li^+$  extraction/insertion reaction with  $Mg_2Mn_{0.5}Ti_{0.5}O_4$  inverse spinel in the aqueous phase, J. Rare Metal, 2007,26(6),121
- [2] Z.Peng: S.Synthesis and electrochemical studies on spinel phase  $LiMn_2O_4$  cathode material prepared by different proceses, J. Rare Metal, 1999,18(2),143
- [3] Y.F.Liu, Q.F, Kenta Ool: The synthesis and ion-exchange property of  $Li^+$  memorized spinel  $LiAlMnO_4$ ,J.Ion Exchange and Adsorption.1995,11(3),216
- [4] J.H.Jiang, D.Q.Dong, J.L: Li Synthesis of  $Li_4Mn_{0.5}Ti_{0.5}O_4$  and its selectivity to  $Li^+$  exchange, J.Chinese Journal of Applied Chemistry.2006,23(4),357

## Phase Composition and Microstructure of $\text{Ca}_{1-3x}\text{Ln}_{2x}\text{TiO}_3$ (Ln=La, Nd, Sm) Ceramics

Bingliang LIANG<sup>1, a</sup>, Yunlong AI<sup>1, b</sup>, Xinghua ZHENG<sup>2, c</sup>, Deping TANG<sup>2, d</sup>,  
and Fei HE<sup>1, e</sup>

<sup>1</sup>College of Materials Science and Engineering, Nanchang Hangkong University, No.696 South Fenghe Road, Nanchang, Jiangxi, 330063, P.R. China

<sup>2</sup>College of Materials Science and Engineering, Fuzhou University, No.2 Xueyuan Road, Fuzhou, Fujian, 350108, P.R. China

<sup>a</sup>lbl@nchu.edu.cn, <sup>b</sup>ayunlong@126.com, <sup>c</sup>brook76@163.com, <sup>d</sup>dptang@fzu.edu.cn,  
<sup>e</sup>hefei0792@hotmail.com

**Keywords:**  $\text{Ca}_{1-3x}\text{Ln}_{2x}\text{TiO}_3$ ; Microstructure; Average Electronegativity Difference; Tolerance factor

**Abstract.**  $\text{Ca}_{1-3x}\text{Ln}_{2x}\text{TiO}_3$  (Ln=La, Nd, Sm;  $x=0.13, 0.20$ ) ceramics were investigated systematically to discuss the influences of sintering temperature, compositions,  $\text{Ln}^{3+}$  ions on its sintering property, crystal structure and microstructure. The results show that the dense ceramics were obtained in the sintering temperature range of 1300~1350 °C and the relative density reached over 97%. Sintering temperature was 50~150 °C lower than previous reports. Single orthogonal perovskite structure phase was formed except that a little secondary phase  $\text{Sm}_2\text{Ti}_2\text{O}_7$  was detected by XRD analysis when  $x=0.20$  and Ln=Sm. The growth pattern of  $\text{Ca}_{1-3x}\text{Ln}_{2x}\text{TiO}_3$  grains was terracing growth.

### Introduction

With the tremendous development of modern communication technology such as mobile communication, satellite broadcasting and ultra-high speed wireless LAN, the demands for microwave dielectric resonators, filters and antennas increase rapidly. As a result, microwave dielectric ceramics, the key materials for manufacturing these components, were investigated widely in recent years. A combination of high dielectric constant ( $\epsilon$ ), low dielectric loss (i.e. high  $Qf$ -value) and near zero temperature coefficient of resonant frequency ( $\tau_f$ ) in microwave dielectric ceramics is necessary to reduce the size of devices, ensure spectral purity at microwave frequencies and ensure high stability of devices, respectively. With typical  $\text{ABO}_3$  type perovskite structure,  $\text{CaTiO}_3$  ceramic possesses high dielectric constant ( $\epsilon \sim 170$ ), however, not high enough  $Qf$ -value ( $Qf \sim 3600\text{GHz}$ ) and huge positive temperature coefficient of resonance frequency ( $\tau_f \sim +800 \times 10^{-6}/^\circ\text{C}$ ) [1], consequently, can not satisfy the requirements of practical application. Therefore, researchers conducted a series of research to enhance  $Qf$ -value and reduce  $\tau_f$  of  $\text{CaTiO}_3$  ceramic. For instance, after  $\text{Ca}^{2+}$  ions were replaced by trivalent  $\text{Ln}^{3+}$  (Ln=La, Nd, Sm) ions, respectively,  $\tau_f$  and dielectric loss of  $\text{CaTiO}_3$  ceramic decreased observably, moreover,  $\epsilon$  still maintained at  $\sim 110$ . From the study of Kim et al [2],  $\epsilon$  and  $\tau_f$  decreased with increasing  $x$  value in  $(1-x)\text{CaTiO}_3-x\text{La}_{2/3}\text{TiO}_3$  ( $0.1 \leq x \leq 0.96$ ) system. Meanwhile,  $Qf$ -value increased rapidly at the onset and linearly rose when  $x > 0.3$ .  $\epsilon = 90$  and  $\tau_f = +190 \times 10^{-6}/^\circ\text{C}$  when  $x = 0.96$ . However, Huang et al [3] reported that the peak value of  $Qf = 17600\text{GHz}$  appeared when  $x = 0.4$  in  $\text{Ca}_{1-x}\text{La}_{2x/3}\text{TiO}_3$  ( $0.1 \leq x \leq 0.9$ ) system. The structure and microwave dielectric properties of  $\text{Ca}_{1-x}\text{Nd}_{2x/3}\text{TiO}_3$  ( $0 \leq x \leq 1$ , CNT) ceramics were investigated by Yoshida et al [4]. The results shown that CNT belonged to  $\text{GdFeO}_3$  type orthorhombic perovskite structure ( $0 \leq x \leq 0.69$ ) and  $\text{La}_{2/3}\text{TiO}_3$  type double perovskite structure ( $0.78 \leq x \leq 0.93$ ),  $\epsilon$  and  $\tau_f$  decreased,  $Qf$ -value increased remarkably and reached the maximum of  $17200\text{GHz}$  when  $x = 0.39$  and then decreased with the increasing  $x$  value. In addition, Fu et al [5] considered the crystal structure of  $\text{Ca}_{1-x}\text{Nd}_{2x/3}\text{TiO}_3$  ( $x = 0.30, 0.39, 0.48$ ) as orthorhombic perovskite structure. The structure of  $\text{Ca}_{1-x}\text{Sm}_{2x/3}\text{TiO}_3$  ( $0.0 \leq x \leq 0.8$ ) transformed from orthorhombic perovskite structure ( $x = 0$ ) to tetragonal perovskite structure ( $x = 0.6$ ) [6]. With the increasing  $\text{Sm}^{3+}$  content, the amount of vacancy at  $A$ -site of CST increased, accompanying by the

decrease of microwave dielectric loss.  $Qf$ -value reached the maximum (14900GHz) when  $x=0.6$  and decreased due to the appearance of  $\text{Sm}_2\text{Ti}_2\text{O}_7$ . Yoon et al [7] discussed the influence of octahedral-site bond valence on the microwave dielectric properties of  $\text{Ca}_{1-x}\text{Sm}_{2x/3}\text{TiO}_3$  ( $0.0 \leq x \leq 0.6$ ) ceramics. As  $\text{Sm}^{3+}$  content increased, vacancy concentration at  $A$ -site increased, which probably reduced the anharmonic vibration in crystal lattice, consequently, dielectric loss was lessened and  $Qf$  increased.

However, according to previous reports, crystal structures and microwave dielectric properties of  $\text{Ca}_{1-3x}\text{Ln}_{2x}\text{TiO}_3$  ceramics were not so identical researched. In the present work,  $\text{Ca}_{1-3x}\text{Ln}_{2x}\text{TiO}_3$  ( $\text{Ln}=\text{La}, \text{Nd}, \text{Sm}; x=0.13, 0.20$ ) ceramics were investigated systematically to discuss the influences of sintering temperature, compositions,  $\text{Ln}^{3+}$  ions on its sintering property, crystal structure and microstructure.

## Experimental procedures

The conventional solid-state preparation route was used to synthesize  $\text{Ca}_{1-3x}\text{Ln}_{2x}\text{TiO}_3$  ( $\text{Ln}=\text{La}, \text{Nd}, \text{Sm}; x=0.13, 0.20$ ) specimens from  $\text{CaCO}_3$  (99.8%),  $\text{La}_2\text{O}_3$  (99.9%),  $\text{Nd}_2\text{O}_3$  (99.9%),  $\text{Sm}_2\text{O}_3$  (99.9%) and  $\text{TiO}_2$  (99.5%). According to the composition of  $\text{Ca}_{1-3x}\text{Ln}_{2x}\text{TiO}_3$ , stoichiometric starting powders were ball milled together in polyethylene jar with  $\text{ZrO}_2$  media for 12 h in distilled water. The mixtures were dried and calcined at 1200 °C for 3 h in air. And then the calcined powders were pressed into disks under a pressure of 98 MPa with suitable amount of 5 wt.% solution of polyvinyl alcohol (PVA) as the binder. Then the disks were sintered at 1300~1350 °C in air for 3 h.

The densities of the sintered pellets were measured by Archimedes method. The phase identification of the present ceramics was carried out by X-ray diffractometer (XRD, Rigaku D/max Ultima III) with  $\text{Cu-K}_\alpha$  radiation ( $\lambda=0.15406$  nm). The microstructure observation was performed on thermal etched specimens using environmental scanning electron microscope (ESEM, Philips XL30 ESEM-TMP).

## Results and discussion

The apparent density of  $\text{Ca}_{1-3x}\text{Ln}_{2x}\text{TiO}_3$  ceramics as a function of composition was shown in Fig. 1. The dense ceramics were obtained in the sintering temperature range of 1300~1350 °C and the relative density reached over 97%. Sintering temperature was 50~150 °C lower than 1400 °C [2-4] or 1450 °C [6, 7] according to previous reports. On the one hand, the volume of unit-cell ( $V_u$ ) decreased with the decreasing  $\text{Ln}^{3+}$  radius as listed in Table 1. On the other hand, the weight of unit-cell increased because the atomic weight of  $\text{Ln}^{3+}$  ions increased in turn of  $\text{La} \rightarrow \text{Nd} \rightarrow \text{Sm}$ . As a result, the density of  $\text{Ca}_{1-3x}\text{Ln}_{2x/3}\text{TiO}_3$  ceramics increased with the decreasing ionic radius or increasing atomic weight of  $\text{Ln}^{3+}$  ions after  $\text{Ca}^{2+}$  ions were replaced by  $\text{Ln}^{3+}$  ions. In addition, as the content of  $\text{Ln}^{3+}$  ions increased, density increased obviously due to the fact that the atomic weight of  $\text{Ln}^{3+}$  ions are much greater than that of  $\text{Ca}^{2+}$  ion.

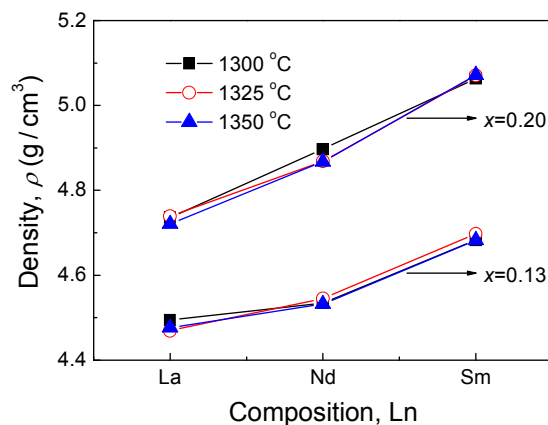


Fig. 1 Density of  $\text{Ca}_{1-3x}\text{Ln}_{2x}\text{TiO}_3$  ceramics

From the XRD patterns of  $\text{Ca}_{1-3x}\text{Ln}_{2x}\text{TiO}_3$  ceramics (as shown in Fig. 2), the diffraction peaks shifted rightwards in the turn of  $\text{La} \rightarrow \text{Nd} \rightarrow \text{Sm}$ , which indicated that the crystal lattice constants reduced gradually according to the Bragg equation (as listed in Table 1). The lattice constants ( $a$ ,  $b$ ,  $c$ ,  $V_u$ ) of orthogonal perovskite structure calculated by the least square method from the main diffraction peaks of the XRD patterns were listed in Table 1. As the radius of  $\text{Ln}^{3+}$  ions decreased,  $a$ ,  $b$ ,  $c$  and  $V_u$  decreased in turn. Nevertheless, the lattice constants increased in different degree when the content of  $\text{Ln}^{3+}$  ions increased. This trend was reported by Fu et al [5] without relevant interpretation.

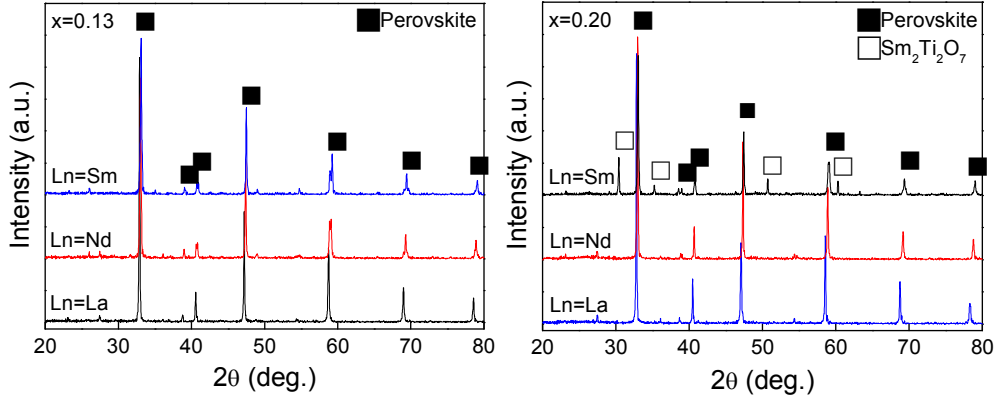


Fig. 2 XRD patterns of  $\text{Ca}_{1-3x}\text{Ln}_{2x}\text{TiO}_3$  ceramics (1325 °C, 3 h)

Table 1 Lattice constants of orthorhombic perovskite phase in  $\text{Ca}_{1-3x}\text{Ln}_{2x}\text{TiO}_3$  ceramics

Composition	$x=0.00$ [8]			$x=0.13$			$x=0.20$		
	$\text{CaTiO}_3$	$\text{Ln}=\text{La}$	$\text{Ln}=\text{Nd}$	$\text{Ln}=\text{Sm}$	$\text{Ln}=\text{La}$	$\text{Ln}=\text{Nd}$	$\text{Ln}=\text{Sm}$	$\text{Ln}=\text{La}$	$\text{Ln}=\text{Nd}$
$a$ (0.1nm)	5.3827	5.4383	5.3960	5.3903	5.4514	5.4263	5.4140	5.4514	5.4263
$b$ (0.1nm)	5.4537	5.4407	5.4363	5.4298	5.4560	5.4279	5.4185	5.4560	5.4279
$c$ (0.1nm)	7.6551	7.6935	7.6648	7.6467	7.7168	7.6755	7.6583	7.7168	7.6755
$V_u$ ( $10^{-30}\text{m}^3$ )	224.72	227.64	224.84	223.81	229.52	226.07	224.66	229.52	226.07

Generally, the lattice constants of substitutional solid solution depend on effective ionic radius, average electronegativity difference and lattice defects. When coordination number equal to 12, the effective ionic radius of  $\text{Ca}^{2+}$ ,  $\text{La}^{3+}$ ,  $\text{Nd}^{3+}$  and  $\text{Sm}^{3+}$  were 0.134 nm, 0.136 nm, 0.127 nm and 0.124 nm [9], respectively. As the radius of  $\text{Ln}^{3+}$  ions decreased, the lattice constants of  $\text{Ca}_{1-3x}\text{Ln}_{2x}\text{TiO}_3$  decreased in the turn of  $\text{La} \rightarrow \text{Nd} \rightarrow \text{Sm}$  when the  $x$  value unchanged.

The concept of “electronegativity” was derived by Pauling [10] in 1932, taking ionization energy and electron affinity into account. The larger average electronegativity difference means the more stable crystal structure, conversely, the combination of ions becomes loosely. The average electronegativity difference of  $\text{Ca}_{1-3x}\text{Ln}_{2x}\text{TiO}_3$  can be calculated from Eq. 1 [11] (as listed in Table 2):

$$e = [(1-3x)\chi_{\text{Ca-O}} + 2x\chi_{\text{Ln-O}}] / (1-x) \quad (1)$$

where  $\chi_{\text{Ca-O}}$  and  $\chi_{\text{Ln-O}}$  are the electronegativity difference of  $\text{Ca}^{2+}$  and  $\text{Ln}^{3+}$  with  $\text{O}^{2-}$ , respectively. As the content of  $\text{Ln}^{3+}$  ions increased, average electronegativity difference decreased. It indicated that the combination of ions became looser after  $\text{Ca}^{2+}$  ions were replaced by  $\text{Ln}^{3+}$  ions, i.e., lattice constants trended to increase.

With the similar ionic radius to  $\text{Ca}^{2+}$  ion,  $\text{Ln}^{3+}$  ions replaced  $\text{Ca}^{2+}$  ions into  $A$ -site of the orthogonal perovskite crystal lattice. Meanwhile, to keep the balance of electrovalence, vacancies in  $A$ -site were introduced. Furthermore, the amount of vacancies increased with the increasing  $\text{Ln}^{3+}$  ionic concentration. Defect reaction equation can be written as Eq. 2:



The lattice constants trend to decrease due to the introduction of vacancies in  $A$ -site.

In a word, lattice constants of  $\text{Ca}_{1-3x}\text{Ln}_{2x}\text{TiO}_3$  depended on effective ionic radius, average electronegativity difference and vacancies in  $A$ -site. The variation trend of lattice constants with the content of  $\text{Ln}^{3+}$  ionic concentration rested with the competitive relationship among the three factors. In more specific terms, as the  $\text{Ln}^{3+}$  ionic concentration increased, the influence of the average electronegativity difference on lattice constants was dominated, therefore, the lattice constants of  $\text{Ca}_{1-3x}\text{Ln}_{2x}\text{TiO}_3$  increased. On the other hand, when  $x$  value unchanged, lattice constants influenced principally by effective ionic radius, consequently, decreased in the turn of  $\text{La} \rightarrow \text{Nd} \rightarrow \text{Sm}$ .

As shown in Fig. 2, the diffraction peaks of  $\text{Ca}_{1-3x}\text{Ln}_{2x}\text{TiO}_3$  coincide with single orthogonal perovskite structure except that a little  $\text{Sm}_2\text{Ti}_2\text{O}_7$  was detected by XRD analysis when  $x=0.20$  and  $\text{Ln}=\text{Sm}$ , i.e., the orthogonal perovskite structure was not stable any more. It indicated that the solid solution limit of  $\text{Ca}_{1-3x}\text{Sm}_{2x}\text{TiO}_3$  was less than 0.20, which was different from the reports of Kim et al [6],  $\text{Sm}_2\text{Ti}_2\text{O}_7$  appeared until  $x=0.27$ .

On the other hand, besides average electronegativity difference ( $e$ ), the tolerance factor ( $t$ ) is another important parameter to evaluate the stability of crystal structure [12]. As to  $\text{ABO}_3$  type perovskite structure, the tolerance factor can be written as

$$t = (R_A + R_O) / [\sqrt{2}(R_B + R_O)] \quad (3)$$

where  $R_A$ ,  $R_B$  and  $R_O$  are the radius of ions in  $A$ ,  $B$ -site and  $\text{O}^{2-}$  according to Shannon [9], respectively.

As listed in Table 2, the average electronegativity difference ( $e$ ) decreased with increasing  $\text{Ln}^{3+}$  concentration. Meanwhile, when  $x$  value unchanged,  $e$  decreased in the turn of  $\text{La} \rightarrow \text{Nd} \rightarrow \text{Sm}$ . It indicated that the chemical bond strength reduced, consequently, the stability of perovskite structure lessened. The variation trend of tolerance factor ( $t$ ) is similar to that of  $e$ , i.e.,  $t$  deviates from 1 increasingly. This also means that the stability of perovskite structure lessened. Both  $e$  and  $t$  of  $\text{Ca}_{0.4}\text{Sm}_{0.4}\text{TiO}_3$  are the minimum. As a result, single perovskite structure can not maintain and the second phase  $\text{Sm}_2\text{Ti}_2\text{O}_7$  appeared.

Table 2 The average electronegativity difference ( $e$ ) and tolerance factor ( $t$ ) of  $\text{Ca}_{1-3x}\text{Ln}_{2x}\text{TiO}_3$

Composition	$x=0.00$ [8]			$x=0.13$			$x=0.20$		
	$\text{CaTiO}_3$	$\text{Ln}=\text{La}$	$\text{Ln}=\text{Nd}$	$\text{Ln}=\text{Sm}$	$\text{Ln}=\text{La}$	$\text{Ln}=\text{Nd}$	$\text{Ln}=\text{Sm}$		
$e$	2.1700	2.1373	2.1318	2.1276	2.1178	2.1089	2.1022		
$t$	0.9639	0.9045	0.8962	0.8935	0.8725	0.8598	0.8556		

The dense ceramics with high relative density ( $>97\%$ ) can be obtained by sintering at the temperature range of  $1300 \sim 1350$  °C. SEM photographs of  $\text{Ca}_{1-3x}\text{Ln}_{2x}\text{TiO}_3$  ceramics are shown in Fig. 3. A large quantity of massive grains and a few granular grains, with intended and ladder-like microstructure even unambiguous interfacial angle are observed, indicating the terracing growth of grains. However, when  $x=0.20$  and  $\text{Ln}=\text{Sm}$ , granular grains increased obviously, probably corresponding to the secondary phase  $\text{Sm}_2\text{Ti}_2\text{O}_7$ .

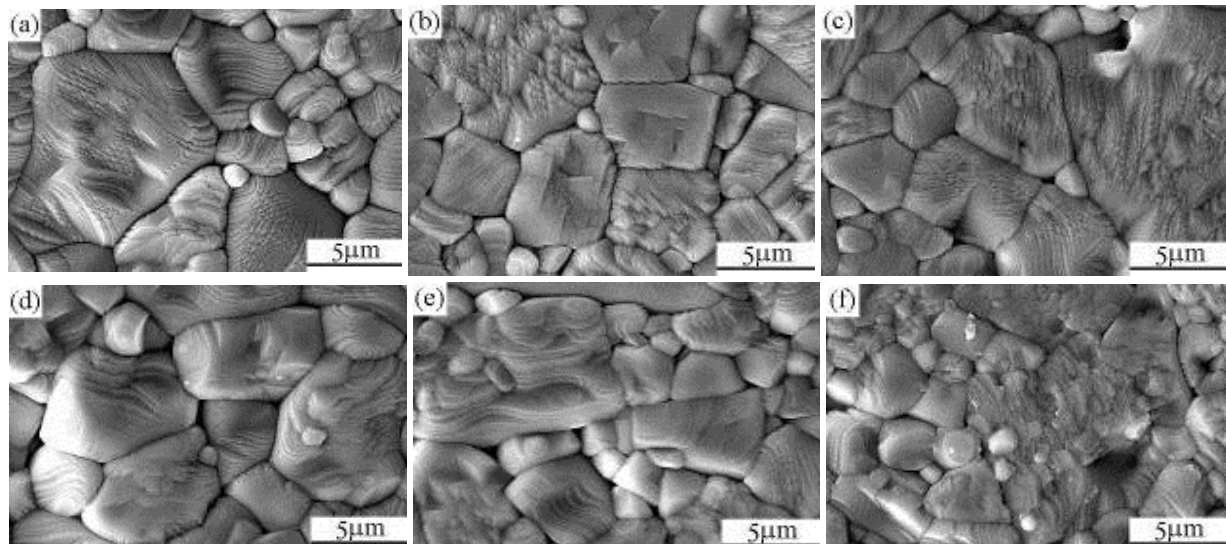


Fig. 4 SEM images of  $\text{Ca}_{1-3x}\text{Ln}_{2x}\text{TiO}_3$  ceramics:  $x=0.13$ ,  $\text{Ln}=\text{La}$ (a),  $\text{Nd}$ (b),  $\text{Sm}$ (c);  $x=0.20$ ,  $\text{Ln}=\text{La}$ (d),  $\text{Nd}$ (e),  $\text{Sm}$ (f)

### Conclusions

1. The dense ceramics were obtained in the sintering temperature range of 1300~1350 °C and the relative density reached over 97%. Sintering temperature was 50~150 °C lower than previous reports.
2. Single orthogonal perovskite structure phase was formed except that a little secondary phase  $\text{Sm}_2\text{Ti}_2\text{O}_7$  was detected by XRD analysis when  $x=0.20$  and  $\text{Ln}=\text{Sm}$ .
3. The growth pattern of  $\text{Ca}_{1-3x}\text{Ln}_{2x}\text{TiO}_3$  grains was terracing growth.

### Acknowledgements

The present work was supported by National Natural Science Foundation of China (51064022), Aeronautical Science Foundation of China (2010ZF56020), Fujian Science Fund for Young Scholars (2005J012), Fujian Key Technologies R&D Program (2005HZ02-03) and Fuzhou University Science Foundation (XJY0413, 2005-XY-01).

### References

- [1] R.C. Kell, A.C. Greenham and G.C.E Olds. *J. Am. Ceram. Soc.*, Vol. 7 (1973), p. 352
- [2] I.S. Kim, W.H. Jung, Y. Inaguma, T. Nakamura and M. Itoh. *Mater. Res. Bull.*, Vol. 3 (1995), p. 307
- [3] C.L. Huang, J.T. Tsai and Y.B. Chen. *Mater. Res. Bull.*, Vol. 3-4 (2001), p. 547
- [4] M. Yoshida, N. Hara, T. Takada and A. Seki. *Jpn. J. Appl. Phys.*, Vol. 11 (1997), p. 6818
- [5] M.S. Fu, X.Q. Liu and X.M. Chen. *J. Eur. Ceram. Soc.*, Vol. 3 (2008), p. 585
- [6] W.S. Kim, E.S. Kim and K.H. Yoon. *J. Am. Ceram. Soc.*, Vol. 8 (1999), p. 2111
- [7] K.H. Yoon, W.S. Kim and E.S. Kim. *Mater. Sci. Eng. B*, Vol. 1-3 (2003), p. 112
- [8] R. Ranjan, D. Pandey, V. Siruguri, P.S.R. Krishna and S.K. Paranjpe. *J. Phys.: Condens. Matter.*, Vol. 10 (1999), p. 2233
- [9] R.D. Shannon. *Acta Crystallographica A*, Vol. 32 (1976), p. 751
- [10] L. Pauling. *J. Am. Chem. Soc.*, Vol. 54 (1932), p. 3570
- [11] X.H. Zheng and X.M. Chen. *J. Mater. Res.*, Vol. 7 (2002), p. 1664
- [12] V.M. Goldschmidt. *Naturwissenschaften*, Vol. 21 (1926), p. 477

## Analysis of Influencing Factors of Ultrasonic Nondestructive Testing with Carbon Fiber Reinforced Plastics

Di Xue<sup>a</sup>, Jinbo Zhang<sup>b</sup>, Caihua Li<sup>c</sup>

College of Mechanical Engineering, Jiamusi University, Jiamusi, 154007, China

<sup>a</sup>444617059@qq.com, <sup>b</sup>Corresponding Author: zhangjinpo9872@sina.com, <sup>c</sup>licaihuaajms@163.com

**Keywords:** Nondestructive testing; Ultrasonic wave; Sensitivity; Carbon fiber reinforce plastics; Composite material

**Abstract.** In order to research the influenced factors of sensitivity of ultrasonic nondestructive testing, the compared experiments using water immersion and contact method were carried out and the experimental results of sensitivities were obtained. The results showed that the limited sensitivities of probes with 1MHz and 2.25 MHz is very low. And the defects of  $\phi 1$ mm, which distance not exceeding 1mm, can be detected by probes of 5 MHz and 10 MHz. The defects of  $\phi 0.5$ mm can be detected by probes of 15 MHz and 20 MHz. The definition of defects appearance will be further improved for the probes with their frequency more than 15 MHz when the scanning step enough small. The distance of probes and defects has little effect on the detecting sensitivity.

### Introduction

In recent years, carbon fiber reinforce plastics (CFRP) was being wide applied to main force bearing structure of all kinds of tools and mechanical components. Advanced composite materials can improve the weight lighting and high performance of components because of its excellent characteristics[1]. The CFRP has been widely applied in many fields because of its excellent mechanical properties[2]. The CFRP is a multiphase system with complicated anisotropy, it has characteristics as follows: quality discreteness, complex molding process, and defects may be produced in the manufacturing process because of environmental control, manufacture engineering and operation[3]. The static load, mechanical damage, fatigue, creep deformation and overheating can lead to structure damage of composite material in the working process[4]. Those defects and damages can reduce greatly service life of structure, even disastrous consequence will be brought to structures of tools and machines[5].

The basic science technology which ultrasonic nondestructive testing technology is applied to CFRP field was discussed in this paper, and this will lay a theoretical foundation for the development of ultrasonic nondestructive testing technology.

### Experiment and discussion of results

This study conducts ultrasonic nondestructive testing of carbon fiber reinforce plastics, using two methods, contact method and flooding method. At the same time, it also studies how step and focus affect the sensitivity in the process of non-destructive testing.

**probes.** The section headings are in boldface capital and lowercase letters. Second level headings are typed as part of the succeeding paragraph (like the subsection heading of this paragraph).

**The properties of the probe.** Straight contact probe and immersion focused probe are the two most commonly used probes in Ultrasonic Testing.

Straight contact probe operates flexible and fast, but it requires the detected parts has shape rules and a relatively smooth contact surface. Due to serious spread of the velocity (Fig. 1), the ratio of the effective area which small defects received in the sound field and the same wave vibration surface area tends to be small, which results in small defects reflected energy and low sensitivity in the defect detection process. In the manual testing process of the three types of CFRP materials system of this study.

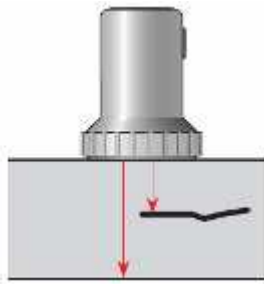


Fig.1 The beam spread schematic diagram of the direct-contact probe

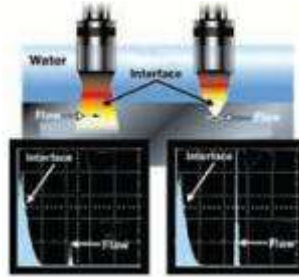


Fig. 2 The sensitivities comparison of above two methods

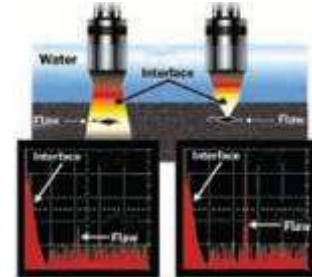


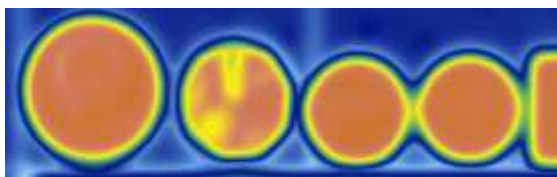
Fig. 3 The sensitivities comparison under the same signal noise ratio conditions

Compared to direct-contact probe, immersion focused probe’s energy in the face detection focused more. Therefore, immersion focused probe has higher sensitivity, shown in Fig. 2.

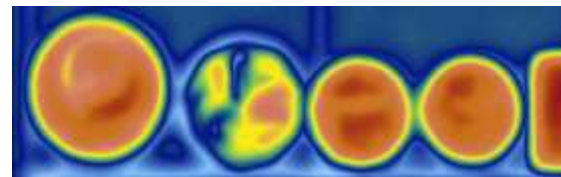
Focus Probe’s sound field diameter in the detection area is adjustable. When the sound focuses on the internal CFRP plate, the beam diameter is less than 1mm. 1mm of the defect can reflect ultrasound energy of the entire beam. Therefore, in the same SNR conditions, it has higher sensitivity, shown in Fig. 3.

**Probe Frequency.** For the same material, the probe of different frequency produce the different wavelengths ultrasonic,  $\lambda=c/f$ , where  $c$  is internal sound velocity in material  $f$  is the frequency of ultrasonic pulse.

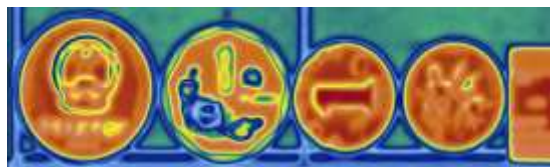
COINS tests: Different frequencies of the probe, to detect a set of coins, shown in Fig. 4 (a), (b), (c), (d), (e), (f).



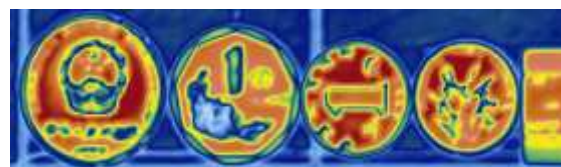
(a) The frequency of probe is 1MHz



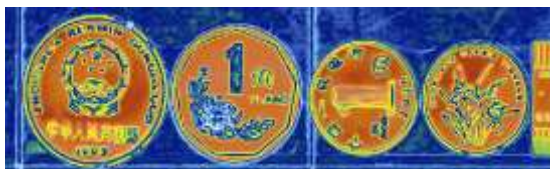
(b) The frequency of probe is 2.25MHz



(c) The frequency of probe is 5MHz



(d) The frequency of probe is 10MHz



(e) The frequency of probe is 15MHz



(f) The frequency of probe is 20MHz

Fig. 4The effect of frequency of probes on the detection results with 0.1mm step

As the results (Fig. 4) of the different frequencies probe ultrasound testing on the coins shown, on the condition of that no impact on the sensitivity, the limits of the sensitivity 1 MHz and 2.25 MHz probe is very low. While 5 MHz and 10 MHz probe has a certain sensitivity detective capacity of small defects. Defects(National Emblem Maximum five-pointed star) can be detected in about  $\phi$ 1mm.but defect spacing of 1mm can not pick out  $\phi$ 1mm defects(as shown in the right side of the ruler scale).  $\phi$ 5mm the size of the defect can be detected by 15 MHz and 20 MHz probe. The probe of 15 MHz can pick out the small defects of 1mm ,while the 20 MHz probe can pick out the small defects of 0.5mm.

CFRP test: Practical CFRP board is tested by the probes of different frequencies.

With the frequency of probe increasing (Fig. 5), there is more and more defects detected on the same CFRP testing area. Although limited by the step 0.5mm, due to the high-frequency ultrasound has strengthened the capacity of reflection. So there are more details of defects displayed in C-scan results. Therefore, on the degree of the SNR can be tolerated, the higher the frequency of probe, the higher sensitivity of detection results.

**Step.** Scanning step decide the display resolution ratio of C-scanning, which influence the instrument ability of detecting tiny defects directly. That is, the minimum value of detection resolution is the scanning step. Via coin ultrasonic inspection and real CFRP ultrasonic inspection and measurement, the effect of scanning step on the detection sensitivity was analyzed by ultrasonic detection experiment with coin and CFRP.

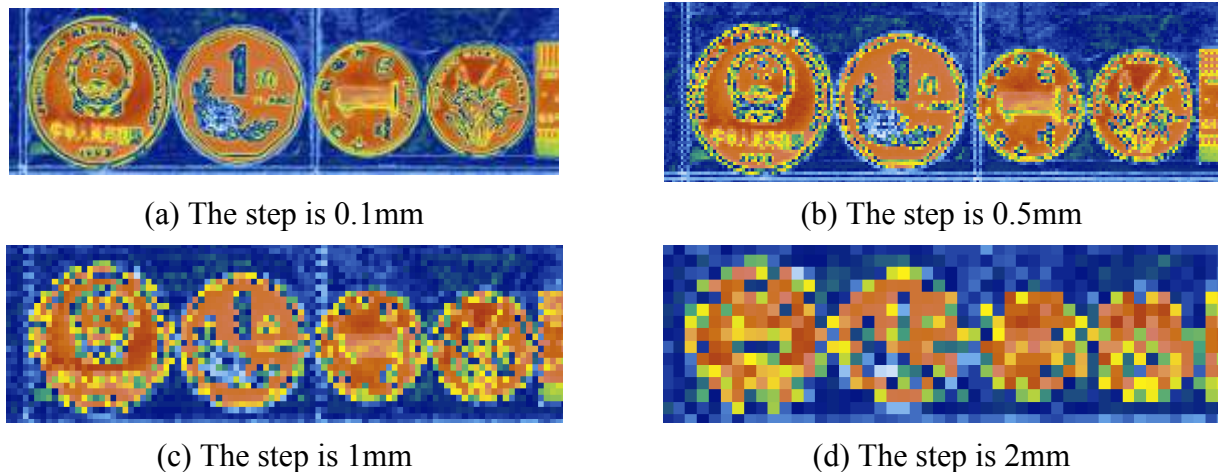
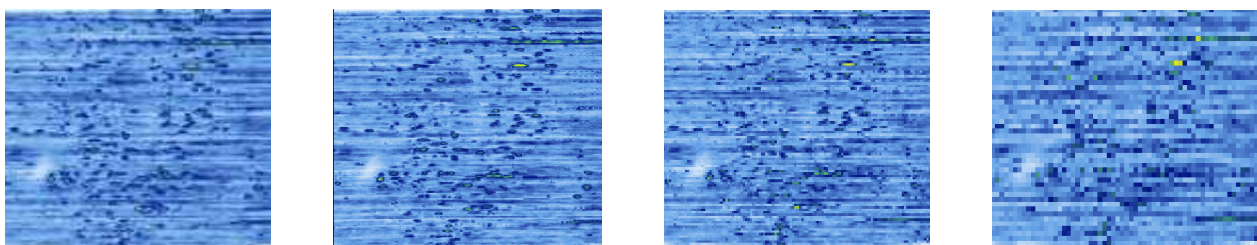


Fig. 6 The effect of step on the sensitivity with the frequency of 15MHz

From detection results (Fig. 6), it was found that the probe which frequency less than 5 MHz, scan step less than 1mm will not cover ultrasound resolution, just has a little difference in smooth of image. When frequency less than 10 MHz, scanning step less than 0.5mm, will not cover ultrasound resolution ratio. But the definition of defects appearance will be further improved for the probes with their frequency more than 15 MHz when the scanning step enough small.

CFRP ultrasonic inspection and measurement experiment: the practical CFRP board was detected by the probe of 10MHz under the condition of changing step(Fig. 7).

According to above results, the scanning step, that is scanning distinguishability, influenced the detection sensitivity, in the scanning process, the step must bigger than limited sensitivity of probe, only in this way, the detection results can not distort.



(a) The step is 0.2mm    (b) The step is 0.5mm    (c) The step is 1mm    (d) The step is 2mm

Fig. 7 The effect of step on the detection result (10MHz)

**Focal length.** Focal length influence acoustic beam diameter of detection surface directly, Hence the energy which influence reflection of defect is called sensitivity. Under the experimental results, choose 0.5mm as scanning step, increasing focal length of 5%, 10%, 20% to research the change of detection sensitivity(Fig.8).

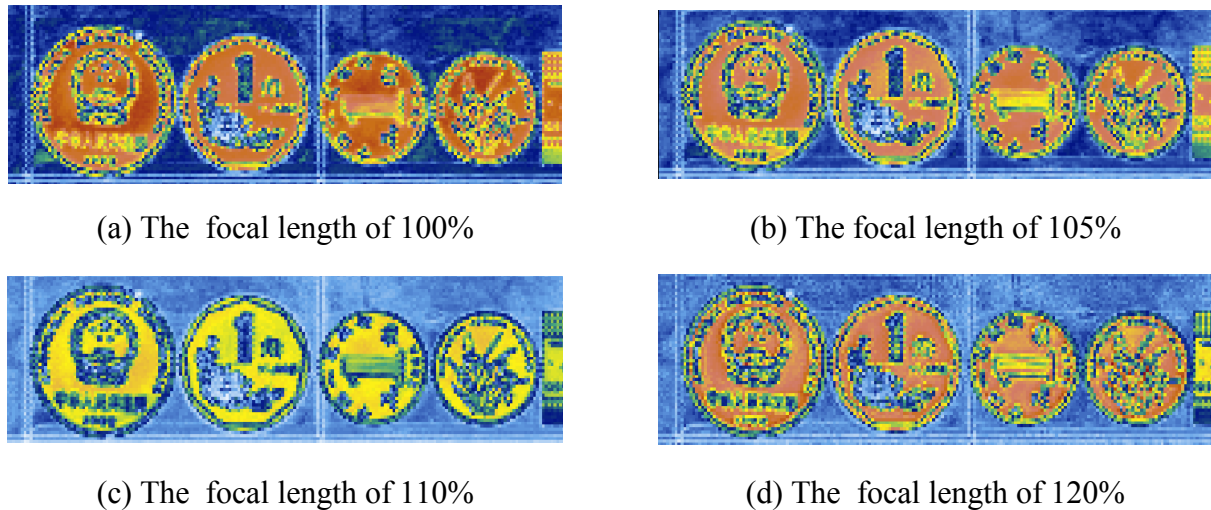


Fig. 8 The effect of focal length on the detection result with the frequency of 15MHz

From the above results (Fig.8), can see that focal length change does not bring big alteration of response rate. This influence become obvious when the size of probe is bigger than 15 MHz.

### Conclusion

The detection limited sensitivities of probes of different frequency as follows: the limited sensitivities of probes with 1MHz and 2.25 MHz is very low. And the defects of  $\phi 1\text{mm}$ , which distance not exceeding 1mm, can be detected by probes of 5 MHz and 10 MHz. The defects of  $\phi 0.5\text{mm}$  can be detected by probes of 15 MHz and 20 MHz.

The probes with their frequency less than 5 MHz can not cover ultrasonic distinguishabilities when the step more than 1mm. The probes with their frequency more than 10 MHz can not cover ultrasonic distinguishabilities when the step more than 0.5mm. But the definition of defects appearance will be further improved for the probes with their frequency more than 15 MHz when the scanning step enough small.

### Acknowledgment

This paper was supported by the research project of Jiamusi University (Grant No. Lq2011-028).

### References

- [1] Huang Xiaoyan, Liu Yuan, Li Xue, Gu Ming: Journal of Agricultural Mechanization Research, 03. (2008). p. 182-185.
- [2] Su Xiaoping: Hi-tech Fiber & Application, 29(5). (2004).p. 34-39.
- [3] Xiaoheng Zhu, Xiaorong Gao, Li Wang, Zeyong Wang, Xiaohong Zhou, Jianping Peng: Modern Electronics Technique, (21). (2010). p.112-116
- [4] Yuntao Liu, Yajing Yang, Guowei Ni, Chunxia Qin: Science and Technology Innovation Herald, (18).119(2010).
- [5] Renjun Wang: Chemical Engineering & Equipment, (04). (2010). p.122-123

## Fabricating TiO<sub>2</sub> Coated ZnO Nanowire Array/Graphene Heterostructure

Yongqiang He<sup>1,2,a</sup>, Siyao He<sup>2,b</sup>, Nana Zhang<sup>3,c</sup>, Wenchao Wang<sup>3,d</sup>,  
Hong Sun<sup>1,e</sup>, Wei Wang<sup>2,3,f</sup> and Haixia Qiu<sup>2,3,g\*</sup>

<sup>1</sup>Department of Applied Chemistry, Yuncheng University, Yuncheng 044000, China

<sup>2</sup> School of Chemical Engineering and technology, Tianjin University, Tianjin 300072, China

<sup>3</sup> School of Science, Tianjin University, Tianjin 300072, China

<sup>a</sup>heyongqiang1985@126.com, <sup>b</sup>siyaohe@163.com <sup>c</sup>naa6576059@163.com,  
<sup>d</sup>waitever09@yahoo.cn, <sup>e</sup>ycxysh@163.com, <sup>f</sup>wangweils@yeah.net, <sup>g</sup>qh@tju.edu.cn

**Keywords:** ZnO, Nanowire array, TiO<sub>2</sub>, Graphene oxide, Composite.

**Abstract.** ZnO nanowire array supported on the graphene surface was fabricated by thermo hydrolysis method. The ZnO nanoparticles (seed crystals) were first deposited on GO surface and then ZnO nanoparticles grew to ZnO nanowire array when the seed crystal side was hung upside down and touched with ZnO precursor solution during the process of thermo hydrolysis. The ZnO nanowire array was then coated with TiO<sub>2</sub> precursor, hydrolyzed and turned to crystalline TiO<sub>2</sub>. The formed ZnO/TiO<sub>2</sub>/graphene composites have different structure depending on the reaction conditions and their morphology was observed with scanning electron microscopy.

### Introduction

Zinc oxide is a unique material that exhibits semiconducting and piezoelectric dual properties, so it is widely applied in industry for many purposes such as optoelectronics, sensors, transducers and biomedical science[1], antireflection coatings, transparent electrodes in solar cell, laser and surface acoustic wave devices, etc[2]. Nano size ZnO is even more attractive and various shapes of ZnO nanocrystals have been prepared[3]. ZnO embedded into a porous template by using the spray pyrolysis method exhibited a broadened dominant excitonic band edge emission and rapidly decreasing deep level emission with decreasing temperature in contrast to ZnO powder[4,5]. The ZnO nano-array can be used as luminiferous materials in laser, light emitting diode and solar cell [6-8]. TiO<sub>2</sub> is another semiconductor. TiO<sub>2</sub>, as one of the most important transition-metal functional oxides, has attracted extensive attention during the past decades for its superior physical and chemical properties. TiO<sub>2</sub> nanowire arrays are widely used in dye sensitized solar cell and photocatalytic degradation of chemical pollutant[9-10]. Heterostructures of two or more components, such as TiO<sub>2</sub> doped/deposited with other semiconductor oxides including ZnO and SnO<sub>2</sub>, sulfides including CdS, PbS and CdSe, or noble metals including Ag, Au, and Pd, have been developed to enhance the separation of photoexcited electron-hole pairs, to provide more surface sites for reactions, and increase the light absorption range[11]. Here, ZnO/graphene and ZnO/TiO<sub>2</sub>/graphene heterostructures were fabricated by thermo hydrolysis method.

### Experimental

The glass slide was firstly treated according to the standard procedure and used as matrix. The glass slide was dipped into 0.01% GO solution for 10 minutes, rinsed with deionized water, flushed with pressed air and dried. Then it was soaked into 0.005mol/L precursor solution of zinc acetate in

absolute ethyl alcohol for 5 minutes, taken out, rinsed with absolute ethyl alcohol and dried at 90°C. The above steps repeated for 10 times, and then the glass slide was put into oven and sintered for 20 minutes at 340°C to obtain ZnO nanoparticles, during which the GO was partly reduced.

Zinc nitrate (0.005mol/L) and hexamethylenetetramine (0.005mol/L) solutions were put into a container. The glass slide was hung inside the container with seed crystal side upside down and touched with the ZnO precursor solution. The container was placed into a high pressure reaction kettle and reacted for 16h at 75°C for ZnO nanowire growth.

The above ZnO nanowire loaded glass slide was soaked into tetraisopropyl titanate (TIPT) solution (0.001mol/L, in absolute ethyl alcohol) for 8h under N<sub>2</sub> atmosphere, taken out and put into water-ethyl alcohol solution (0.0033mol/L) to make tetraisopropyl titanate hydrolyzed, and then soaked into ethyl alcohol aqueous solution (60%) and react for 10h at 160°C in a high pressure reaction kettle. The ZnO nanowire array was observed with scanning electron microscopy (JEOL-6700F ESEM, Japan)

### Results and discussion

The GO nanosheets were prepared in our laboratory by a modified Hummers method[12]. Their aqueous suspension is stable for several months with no precipitation occurring, and this is useful for forming smooth graphene film on the glass slide for growing ZnO nanowires. The ZnO nanowires formed in the early stage is very short, but they are perpendicular to the glass slide as shown in figure 1A. When ZnO nanoparticles were pre-produced and coated on the graphene as seed crystals, the formed ZnO nanowires are not perpendicular to the glass slide (figure 1B). Meanwhile, we found that the solution used to grow ZnO crystals also effect the growth of ZnO nanowires (figure 1C-H). In solution 1 (a mixed solution of 0.01mol/L zinc nitrate, 0.3mol/L ammonia water, 0.005mol/L hexamethylenetetramine, 0.005mol/L polyethyleneimine), the ZnO nanowires do not keep in one direction (figure 1C-D), because they grow too fast. Whereas in solution 2 (a mixed solution of zinc nitrate and 0.005mol/L hexamethylenetetramine), ZnO

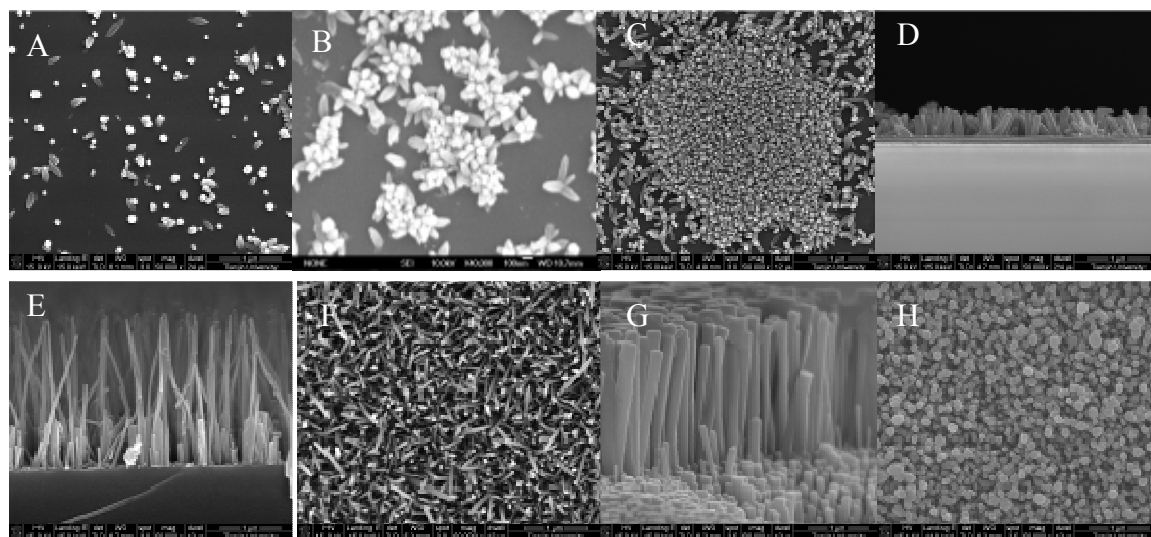


Fig.1 ZnO nanowire arrays grown on the graphene film

nanowires grow slowly, but in one direction (figure 1E-H). Therefore, growing solution 2 was applied to study the effect of its concentration on the ZnO nanowires. The ZnO nanowires raised in high concentration (0.01mol/L) are short but thick. So the ZnO nanowire array is dense and unidirectional (figure 1G-H). On the contrary, ZnO nanowires look thin, so the ZnO nanowire array is comparatively sparse. The long nanowires are too slim to stand straight. The above results indicate that the structure of ZnO nanowire array can be adjusted by changing the concentration of growing solution.

The adhesion of ZnO nanowire array to the GO film is a key point for the following coating of TiO<sub>2</sub> precursor solution. Fig.2A that the adhesion is so strong that the GO film is detached from the glass slide but attached to the ZnO nanowires after thermal treatment. Figure 2B shows the freestanding graphene films with ZnO nanowire array that are layed face-to-face.

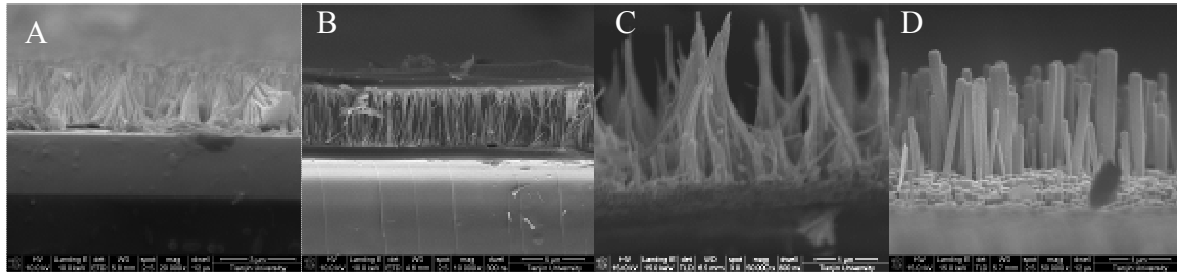


Fig.2 Freestanding graphene film with ZnO nanowire arrays and ZnO nanowire array (Fig.1E and 1G) coated with TiO<sub>2</sub> precursor (C, D)

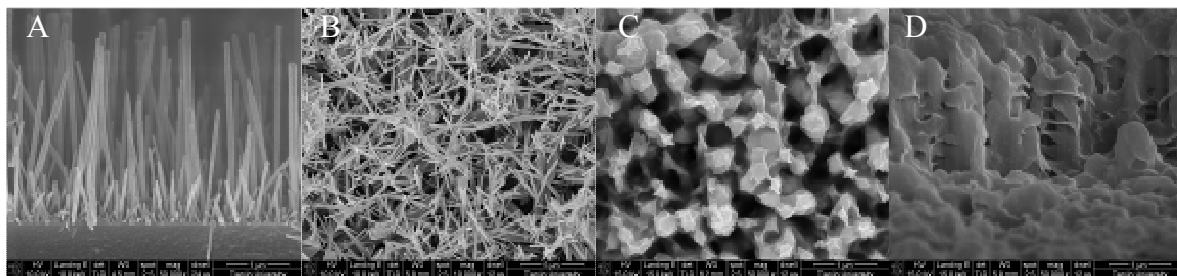


Fig.3 Morphology of TiO<sub>2</sub> grown on ZnO nanowire array in different conditions. (A) 0.0033mol/L TIPT, water; (B) 0.0033mol/L TIPT, 25% ethyl alcohol; (C, D) 0.01mol/L TIPT, 60% ethyl alcohol

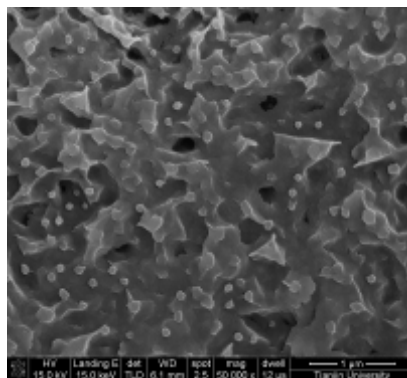


Fig.4 SEM photos of ZnO/TiO<sub>2</sub> after etching

When ZnO nanowire array was coated with tetraisopropyl titanate solution, the nanowire surface became rough (figure 2C, 2D). After thermal treatment for 10h at 160°C, TiO<sub>2</sub> was formed, but the morphology of TiO<sub>2</sub> is different (figure 3). The diameter of the ZnO nanowires in figure 3 increases as compared with the nanowires in figure 1E, indicating that the ZnO nanowires have a TiO<sub>2</sub> shell and ZnO forms the core, or core@shell structure (ZnO@TiO). When TiO<sub>2</sub> grow outside from the side of ZnO nanowires, a new ZnO/TiO<sub>2</sub> structure is formed as shown in figure 3B. This can drastically increase the surface area of the composite and find application in dye sensitized TiO<sub>2</sub> solar cell or photocatalytic degradation of chemicals. When high concentration of TiO<sub>2</sub> precursor is used, the ZnO nanowires are covered by a thick shell of TiO<sub>2</sub> (figure 3C-D). The composite is etched with a mixed solution (3% HF-12% water-85% glycerol) to unveil the ZnO nanowires (figure 4).

## Conclusions

ZnO nanowire array can be grown on the graphene oxide film by thermo hydrolysis. The ZnO nanowires can induce the growth of TiO<sub>2</sub> and creates ZnO/TiO<sub>2</sub> composites of different structure. The ZnO/GO and Zn/TiO<sub>2</sub>/GO heterostructures have potential applications in dye sensitized TiO<sub>2</sub> solar cell and photocatalytic degradation of chemicals.

## Acknowledgements

This work was supported by Tianjin Municipal Science and Technology Commission of P. R. China (09JCZDJC23300) and National Science Foundation of China (No. 21074089).

## Reference

- [1] L.E.Greene, M.Law, J.Goldberger et al: *Angewandte Chemie-International Edition* Vol. 42(2003), p. 3031-3034.
- [2] X.D.Wang, J.H.Song, J.Liu et al: *Science* Vol. 316(2007), p. 102-105.
- [3] L.Ge, X.Y.Jing, J.Wang et al: *Journal of Materials Chemistry* Vol. 21(2011), p. 10750-10754.
- [4] M.Law, L.E.Greene, J.C.Johnson et al: *Nature Materials* Vol. 4(2005), p. 455-459.
- [5] Y.F.Hsu, K.W.Cheah, P.W.K.Fong et al: *Advanced Functional Materials* Vol. 18(2008), p.1020-1030.
- [6] L.E.Greene, J.Goldberger, G.Somorjai et al: *Nano Letters* Vol. 5(2005), p. 1231-1236.
- [7] M.Ladanov, G.Matthews and A. Kumar: *Langmuir* Vol. 27(2011), p. 9012-9017.
- [8] Z.L.Wang and J.H.Song: *Science* Vol. 312(2006), p. 242-246.
- [9] S.I.In, M.G.Nielsen, P.C.K.Vesborg et al: *Chemical Communications* Vol. 47(2011), p. 2613-2615.
- [10] J.J.Qiu, F.W.Zhu, K.Lou et al: *Journal of Materials Chemistry* Vol. 21(2011), p. 5062-5068.
- [11] Y.C.Huang, S.Y.Chang, C.F.Lin et al: *Journal of Materials Chemistry* Vol. 21(2011), 14056-14061.
- [12] W.Hummers and R.Offeman: *Journal of the American Chemical Society* Vol. 80(1958), p. 1339-1340.

## High functional PET sericin composite fabric

Guangxian Zhang<sup>1,a</sup>, Xiaohua Shi<sup>1,b</sup>, Wei Hu<sup>1,c</sup> Fengxiu Zhang<sup>2,d</sup>,

Dayang Wu<sup>1e</sup>

<sup>1</sup> College of textiles and garments, Southwest University, China

<sup>2</sup> School of chemistry and chemical engineering, Southwest University, Chongqing

<sup>a</sup>zgx656472@sina.com, <sup>b</sup>635924043@qq.com, <sup>c</sup>huwei8500397@163.com,  
<sup>d</sup>zhangfx656472@sina.com, <sup>e</sup>Wdy1484@swu.edu.cn

**Keywords:** PET; sericin; composite; function

**Abstract:** Though poly(ethyleneterephthalate)(PET) fabrics have high initial modulus, outstanding creasability and wash-well character, but its hydrophilicity and biocompatibility are very poor. In this paper, the PET fabric was encased sucrose ester at high pressure and high temperature to endue it enough hydroxyl to grafting protein. The sericin was grafted on PET fabric by sucrose ester glycidyl ether (SEGE). The FT-IR spectra showed that sericin was grafted on PET fabric, and the structure of sericin was random coil conformation. X-ray diffraction spectra showed the structure of PET fiber did not changed. DSC showed the thermostability increased a little. After the PET fabric grafted with sericin, the hydrophilicity of PET sericin composite fabric was improved greatly, the cockle elasticity kept well, and the broken strength in creased a little. Certainly, the whiteness and air permeability decreased a little. The PET sericin composite fabric was high functional.

### Introduction

Poly(ethyleneterephthalate)(PET) fabrics have high initial modulus, and outstanding creasability character. Then it is widely used as apparel. But its hydrophilicity and biocompatibility are very poor. Then many papers reported to modify PET fabric to increase its hydrophilicity etc. For example, PET fabric was treated with  $\text{KMnO}_4$  and  $\text{H}_2\text{SO}_4$  to endue PET fabric with  $-\text{COOH}$ , and irritated with ultraviolet and  $\text{O}_3$  to increase the hydrophilicity[1-3], or hydrolyzed to create  $-\text{COOH}$  and  $-\text{OH}$ [4-5].

In this paper, the PET fabric was semi-encased with sucrose ester to endue PET fabric with enough  $-\text{OH}$ . And because sericin has good biocompatibility, the encased PET fabric was grafted with sericin by crosslinkage to endue PET fabric with high functional property.

### Materials and methods

**Materials.** PET fabric was bought from market. hydrochloric acid and NaOH (Chendu Eichlorohydrin, tetrabutylammonium, Chemical agent Company), sucrose ester(Liuzhou Food Additive Company),.

**Synthesizing sucrose ester glycidyl ether(SEGE).** SEGE is a crosslinkage compound which has softening function, because it has hydrophobic hydrocarbon chain. The synthesis method was same as the former paper[6].

**Encasing sucrose ester on PET fabric to endue polyester fabric  $-\text{OH}$ .** The encasing process was at high pressure and high temperature, it was same as the former paper[6].

**Preparing sericin.** The silk was degummed at high pressure and high temperature. The temperature was 130°C, and time 60 min. Then the sericin solution was prepared.

**Grafting sericin on PET fabrics encased sucrose ester.** PET fabrics were immersed into sericin and SEGE solution for 20 min. After immersing, the PET fabrics was dried at 60 °C, and baked at 100 °C for 30 min.

**Analytic Methods.** Differential scanning calorimetry (DSC) measurement was performed by a DSC 2003 F3 Maia instrument. Wide angle X-ray diffraction (WAXD) profile were obtained by a Beijing puxi XD-3 diffractometer. Fourier transform infrared (FT-IR) spectroscopy was measured with a PE FT-IR-Spelmm GX infrared spectrometer.

**Measurement of characteristics of PET sericin composite fabric.** The moisture regain, flexural stiffness, creasability, air permeability, whiteness, broken strength etc. characteristics were measured with standard methods.

## Results and discussion

**Structure.** Fig.1 is FT-IR spectra of PET fabric encased sucrose ester and grafted sericin. The absorption bands at 1700.99cm<sup>-1</sup> is amide I, 1550.42 cm<sup>-1</sup> is amide II, attribute to the  $\beta$ -sheet structure, and 1247 cm<sup>-1</sup> is amide III, attribute to random coil conformation. The amide II is very weak, and amide III is strong, then the structure of sericin on PET fabric is mainly random coil conformation.

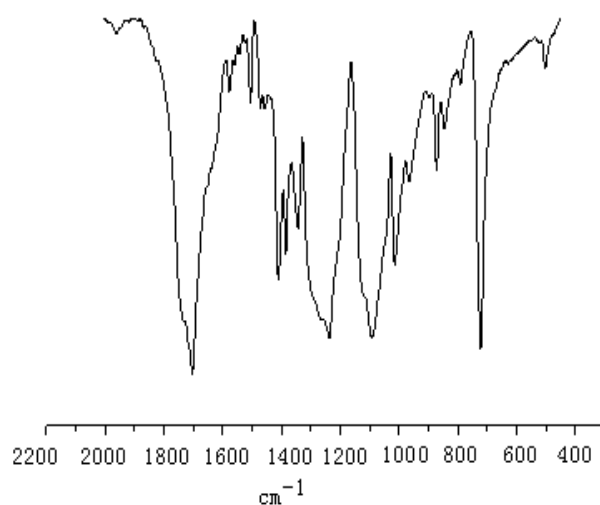


Fig.1 FT-IR spectra of PET fabric grafted with sericin

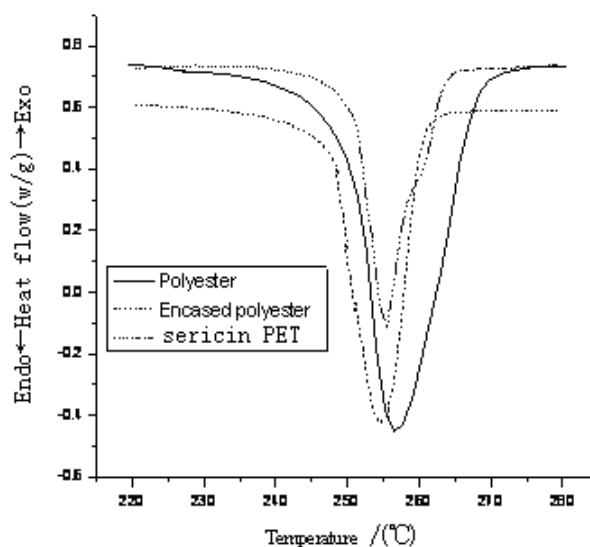


Fig.2 DSC thermograms of PET fabric

Fig.2 is DSC thermograms of PET fabric, PET fabric encased sucrose ester, and PET fabric encased sucrose ester and grafted sericin. From Fig.2, the melt point of PET fabric encased sucrose ester was lower than PET fabric. But the melt point of PET encased sucrose ester and grafted sericin was higher than PET fabric. This showed the thermostability of PET fabric grafted sericin was higher than PET fabric.

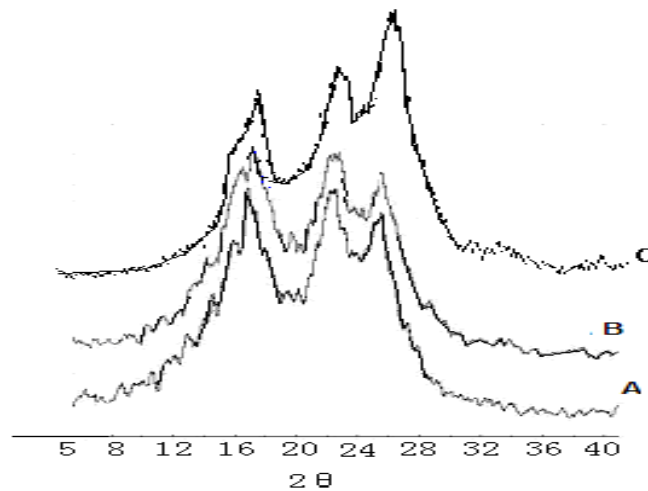


Fig.3 X-ray diffraction spectra of PET fabric

Fig.3 is X-ray diffraction spectra of PET fabric, PET fabric encased sucrose ester, and PET fabric encased sucrose ester and grafted sericin. The three X-ray diffraction spectra were similar, and there was no new diffraction apex, this also showed the structure of sericin on PET fabric was random coil conformation.

### Characteristics of PET fabric grafted sericin

Table 1 showed the wearability and some physical property of PET fabric encased sucrose ester and grafted sericin. With the increase of grafting rate of sericin on PET fabric, the moisture regain increased. When the grafting rate of sericin reached 4.2%, the moisture regain increased 67.5%.

With the increase of grafting rate of sericin on PET fabric, the rapid and cockle elasticity increased firstly, and then decreased a little. In general, with the increase of grafting rate of protein on PET fabric, the cockle elasticity decreased greatly[7]. PET sericin composite fabric only decreased a little when the grafting rate was relative high. This is because the crosslinkage has a hydrophobic hydrocarbon chain, which decreased the interaction of sericin on PET fabric.

Table 1 Characteristics of PET fabric encased sucrose ester and grafted sericin

Grafting rate /(%)	0	0.9	1.5	2.1	3.2	3.8	4.2
Moisture regain/(%)	0.4	0.44	0.52	0.55	0.58	0.58	0.67
Rapid cockle elasticity/(°)	306.12	312.28	311.15	310.46	307.56	304.28	301.37
Slow cockle elasticity/(°)	316.23	324.15	323.18	322.15	318.36	313.23	308.36
Broken strength/(N)	480.12	620.23	618.35	601.23	510.34	650.11	650.08
Whiteness	87.23	80.36	79.26	79.21	75.32	70.18	70.13
Disappearing time of bead /(s)	1805	612	431	305	98	41	20
Contact angle/(°)	170.13	164.21	150.23	142.20	108.15	104.98	95.03
Air permeability/(mm/s)	1609	1605	1592	1463	1365	1365	1306
Spray rating	4	3	2	2	2	1	1

The broken strength of PET fabric grafted sericin not only did not decrease, but also increased a little. This is because the encasing sucrose process did not damage the polyester macromolecule. However, other modification method, such as modified with  $\text{KMnO}_4$ , would break the PET macromolecules.

With the increase of grafting rate of sericin on PET fabric, the whiteness of fabric decreased a little. This is because the sericin solution is not very white.

After the PET fabric grafted sericin, the bead could wet the fabric more easily. The disappearing time of bead on PET fabric could decrease from 1805 second to 20 second. The contact angle decreased from  $170.13^\circ$  to  $95.03^\circ$ , and the spray rating decreased from 4 to 1. These showed the hydrophilicity of PET fabric was improved greatly.

The air permeability of PET fabric grafted sericin decreased a little. This is because the sericin partly jammed the lacune of fabric.

## Conclusions

The FT-IR spectra showed that sericin was grafted on PET fabric, and the structure of sericin was random coil conformation. X-ray diffraction spectra showed the structure of PET fiber did not change. DSC showed the thermostability increased a little. With the increase of grafting rate of sericin, the moisture regain increased, the hydrophilicity was improved greatly, and the whiteness and air permeability decreased a little. The cockle elasticity of PET sericin composite fabric kept well, and the broken strength in creased a little. These showed the PET sericin composite fabric was high functional.

## Acknowledgements

This study was supported by Chongqing science fund(CSTC.2010AA1002), Chongqing natural science fund (CSTC,2008BB4250).

## References

- [1] R.Magalhães, R.Anil KumarP., F.Wena, X.Y Zhao, H. Yub, and L.L Kuleshova: *Biomaterials*,30(2009), P. 4136
- [2] S.L. Fávaro, A.F. Rubira, E.C. Muniz and E. Radovanovic: *Polymer Degradation and Stability*, 92(2007), P. 1219
- [3] Jinho Jang , Youngjin Jeong. *Dyes and pigments*, 69(2005), P.137-143
- [4] Y.X Liu., He T., and C.Y Gao. *Colloids and Surfaces B: Biointerfaces*, 46(2005), P. 117
- [5] C.Chollet, C.Chanseau, B.Brouillaud: *Biomolecular Engineering*, 24(2007), P. 477
- [6] G.X. Zhang, N. Han, W. Hu, F.X. Zhang. *Advanced material research*, 332-334(2011), P.799-803
- [7] M.F.Du, M. Sijia, H.P.Zhang, L.J.Zhu: *Acta Sericologia Sinica*, 33(2007), P. 427-432. In Chinese.

## Study on Nitrogen Shock Absorber Oil

Guangguo Zhang<sup>a</sup>, Zhibin Chang<sup>b</sup> and Longbo Wang<sup>c</sup>

Department of Mechanical Engineering ,Hubei Automotive Industries Institute, Shiyan, Hubei  
Province 442002 P.R.China

<sup>a</sup>qyjxxzgg@sina.com, <sup>b</sup>qyjxxzgg@sohu.com, <sup>c</sup>zhzhangang@126.com

**Keywords:** Shock absorber, Structural design, Nitrogen , Oil

**Abstract.** Liquid shock absorbing system as the primary one, although it can solve the shock absorbing problem, there has been a crash or impact occurs instantaneously when the apparent tilt steering and comfort very poor phenomenon. To this end, a new study of nitrogen gas shock absorber fluid control body height at rated load automatically within the body to adjust to the optimal height designed to improve the car's shock absorber damping effect, making the car more shock absorption system safe and comfortable, with a more stable operational.

### Introduction

Auto automobile shock absorber is one of the key components of suspension rack. Its performance plays a decisive role in the car's carrying capacity, speed, driving stability and comfort. In recent years, with the rapid increase of car ownership in China, people, in addition to car speed, considerate the car's power, economy, emissions, reliability, maneuverability, stability, security. Vehicle suspension shock absorber as an important assembly of suspension system, it can decay auto body vibration, so plays a very important role [1] in the vehicle ride comfort, handling and stability and security. It is positive significance to develop a performance shock absorbers for improvement of the quality of automotive quality and service life of the car.

### Nitrogen-oil fluid's overall design of body height control shock

**Nitrogen – oil fluid structure principle of body height control shock.** Nitrogen – oil fluid structure principle of body height control shock absorber shown in Fig. 1. 1 - piston rod, 2 - pump check valve, 3 - outer cylinder of shock absorber, 4 – up and outside additional chamber, 5 - working cylinder, 6 - guide tube, 7 - outside and under additional cavity, 8 –oil hole , 9 - static and dynamic sealing ring group, 10 – up piston chamber, 11 - oil pump valve, 12 - damping piston, 13 - drain valve hole, 14 - height sensor, 15 – up piston chamber, 16 – fluid shunt.

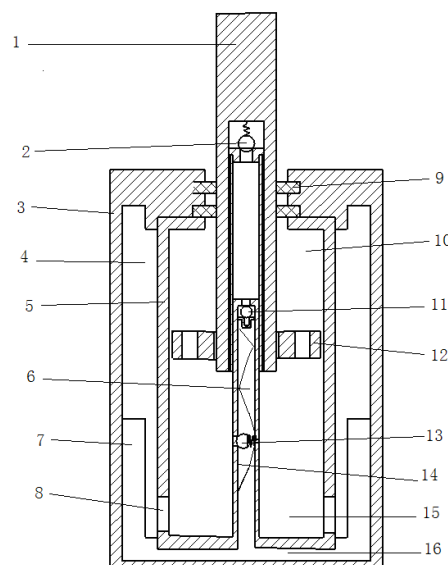


Fig. 1 Nitrogen - Oil damper body height control structure diagram

When shock absorber was stroked by external shocks, the piston rod was in the compression stroke. At this point, the damping piston 12 together with the piston rod 1 runs down. So, up and down the piston cylinder chamber pressure increases, forcing the oil level of piston chamber 15 drops, part of the hydraulic oil from the liquid orifice goes into the guide tube 6, which goes into the next from the guide tube 6 additional external cavity. Also part of the hydraulic oil from the piston chamber 15 goes through the lower orifice of damping group (within the cylinder along the bottom of a set of open orifice) into the outer chamber 4 attached. When the external load was unloaded, piston rod 1 moves upward under nitrogen response elasticity. Excess hydraulic fluid in the outer chamber 4 returns back to the piston 15 from the orifice of the inferior vena group. At this time, there will be a part of the hydraulic oil flows from the pump check valve into guide lubrication chamber, flowing into the piston chamber from the guide lubrication chamber. This completes a cycle of work.

**Nitrogen - oil fluid's overall design structure principle of body height control shock.** Nitrogen - oil fluid's main components and internal structure of body height control shock is shown in Fig. 2. 1 - low-pressure nitrogen, 2 - pump rod, 3 - low-pressure oil, 4 - high-pressure nitrogen, 5 - Oil separator, 6 - hollow rod, 7 - high-pressure oil chamber, 8 - rubber elastic element, 9 - suction tube, 10 - height sensor, 11 - piston valve system, 12 - pump - inlet valve, 13 - control tube, 14 - pump chamber, 15 - pump - oil drain valve.

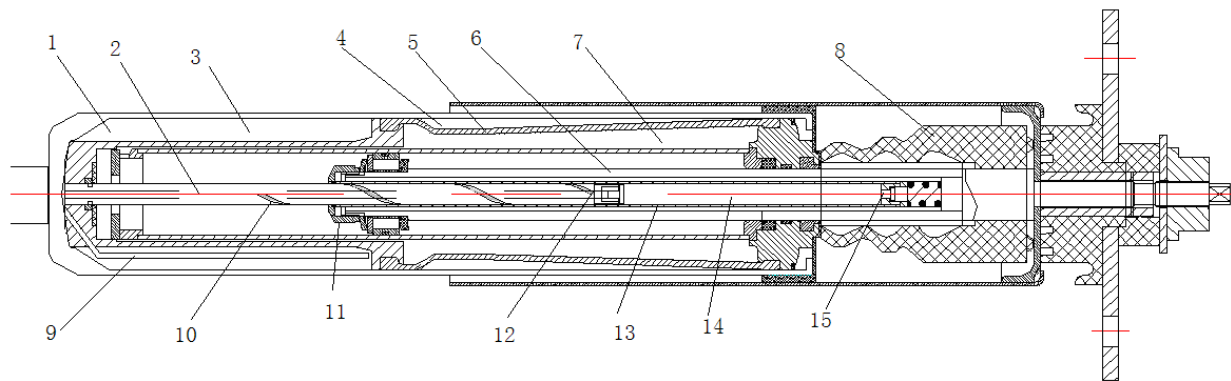


Fig. 2 Nitrogen - a high degree of control of body fluid shock absorber structure

Control sleeve 13 is mounted on the inside of hollow rod 6 and the internal of control sleeve control 13 also is done pump rod 2 and two-way valve, which composes of the pump system. Piston valve system 11 is installed in the lower end of rod 6 (piston side), which moves in the cylinder and produces damping force. Hydraulic oil of high pressure chamber and high pressure gas is separated by oil and gas membrane 5. During the recovery stroke, the volume of the pump chamber 14 varies from small to large and hydraulic oil is drawn from the low-pressure chamber to the pump chamber 14 due to the presence of one-way valve. In the compression stroke of the pump chamber 14 changes from large to small and hydraulic oil from the pump chamber 14 is pumped into the pressure chamber due also to the presence of one-way valve. It is repeating and the pressure of high-pressure chamber is also increasing up to push car body to the best body ride height. Once to the optimum height, the system bypass is opened, the oil runs along s the height of the spiral groove of sensor 10 and the vent hole pump of rod 2, so that fluid pressure circulates in the pump chamber and the high pressure chamber. Car is maintained in the best height.

### Nitrogen - Oil fluid's mathematical model of body height control shock

**Nitrogen - Oil fluid's mathematical model of body height control shock.** Nitrogen - oil fluid's mathematical model of body height control shock is shown in Fig. 3. 1 - sprung mass, 2 - working cylinder, 3 - nitrogen gas springs, 4 - sprung mass, 5 - piston rod, 6 - gas damper, 7 - hydraulic damper, 8 - input signal.

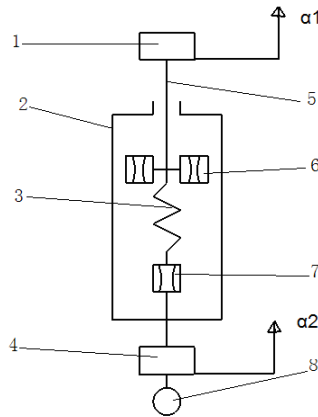


Fig. 3 Physical model of nitrogen damper in cars

For the sprung mass, differential equations is established based on Newton's second law.

$$m_1 a_1 = F_{gas} + F_{gas\_d} - G_1 \tag{1}$$

In the above formula,  $m_1$ - the above-sprung mass.  $a_1$ - the movement acceleration velocity of above-sprung mass.  $F_{gas}$  - elastic force of the nitrogen spring.  $F_{gas\_d}$  - damping force produced by gas damper.  $G_1$  - the gravity of above-sprung mass.

For the sprung mass, a differential equation is established according to Newton's second law.

$$m_2 a_2 = F_s + F_{oil\_d} - F_{gas} - G_2 \tag{2}$$

In the above formula,  $m_2$ - the below-sprung mass.  $a_2$ - the movement acceleration velocity of below-sprung mass.  $F_s = F_A \cos(\omega t)$ .  $F_s$  - exciting force.  $F_A$ -the maximum amplitude of the exciting force.  $F_{oil\_d}$  - damping force produced by gas damper.  $G_2$ -the gravity of below-sprung mass.

For the sprung mass, a differential equation is established according to Newton's second law

**Determination of characteristics of shock absorber damping force.** Damping force generated by oil's passing through throttle is the product of pressure difference on both sides of throttle and pressure area, the pressure is.

$$P = \frac{\rho}{2} \frac{Q^2}{C_d^2 a^2} + \alpha Q \tag{3}$$

$\rho$  - fluid density( $kg/mm^3$ ).  $Q$ -flow passing through the valve( $mm^3/s$ ).  $C_d$  - flow coefficient.  $\alpha$  - coefficient related to orifice shape and fluid viscosity.

**Determination of relative damping coefficient to shock absorber.** After loading, the basic parameters of shock absorber are expressed as the relative damping coefficient, which is.

$$\phi = \frac{\gamma}{2\sqrt{KM}} \tag{4}$$

$\phi$  - the relative damping coefficient.  $\gamma$  - damping coefficient of shock absorber (derivative of damping characteristics).  $K$ -suspension stiffness( $N/mm$ ).  $M$  - sprung mass( $kg$ ).

When the relative damping coefficient  $\phi \geq 1$ , non-periodic domain movement is produced; When  $\phi$  is very large, although it is quickly decay in the resonance area, it increases in the non-resonant excitation region. When  $\phi \geq 1$ , periodic motion is produced and when  $\phi$  is very small, the

resonance amplitude is too large. General relative damping values vary between 0.3 and 0.5 range. Ceiling value should be pick up for the undamped elastic elements, while lower limit should be taken under the condition of existence of flexible components and suspension -oriented mechanism.

In order to rapidly decay vehicle vibration and not to transfer a large road impact to the car body, generally, ,resistance of tensile and compressive of shock absorber is allocated according to the ratio of 8:2 ~ 6:4.

**The choice of shock absorber stroke.** Damper stroke diagram is shown in Fig. 4. The total stroke of damper is consisted of two parts: up-moving stroke and down moving stroke, namely.

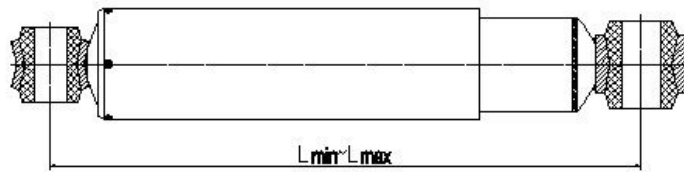


Fig. 4 Schematic diagram of shock absorber stroke

$$S = S_1 + S_2 \quad (5)$$

In forma,  $S_1 = L - L_{\min}$ .  $L$  - center distance of two lugs when a car fully loaded.  $S_1$  -Should be slightly larger than up-stroke when suspension system fully loaded (assuming the buffer block goes off).  $S_2 = L_{\max} - L$ , damper can withstand part of the rebound tension, so  $S_2$  should slightly be larger than the static spring deflection. Bound to the inappropriate choice of  $S_1, S_2$ , shock absorber is not working properly, resulting in pull-off crushed, bashed or broken mounting brackets and so on.

## Conclusion

In this study, oil and gas spring damper physical and mathematical models was established to determine the shock absorber damping characteristics and the calculation as well as the analysis and design of damping characteristics of the damping element.

Body height adjustment and balance power completely come from relative motion between the vehicle body and axle during vehicle moving without any external energy input. So, the real highly integrated, multi-function, zero power and zero emissions is reached.

Application of Nitrogen – oil fluid control of body height fluid shock absorber improves the car's shock absorber damping effect, making the car shock absorber system more safe and comfortable, thus a more stable operational.

## References

- [1] Zhang Taiping, Nonlinear vibration characteristics of oil and gas suspension [D]. Dalian University of Technology, 2007.
- [2] Liu Huihang, Lu Shangyan, Liu Jingbo, Wang Shan. Application and development of nitrogen spring [R]. Xi'an: People's Liberation Army, Institute of 1001 strong spring, 2000:1 1001-9.
- [3] Liu luxiu. Developmental trends on Sachs shock absorber (a) [J]. Automobile and parts, 2006 (7).
- [4] Chen Ji'an, Chen Xiaofeng, Wang Dianfu. Operating characteristic analysis of hydraulic shock absorber [J]. Journal of Harbin Institute of Technology, 1996, 31 (3) :114-117.
- [5] Zhou Changcheng, Liu Ruijun, Zhao Yiqiang. The design method of oil and gas spring valve and its effect on the throttle gap [J]. Ordnance Technology, 2009 (4), 30 (4).
- [6] Cong Lixin. Trial study on the performance of inflatable car shock absorber[D]. Jilin University, a master's degree thesis, 2010.

# The kinetics and activation energy of photocatalytic degradation of phenol by TiO<sub>2</sub> and TiO<sub>2</sub>/ PANI photocatalyst under UV irradiation

Xueyan Li <sup>a</sup>, Qingzhi Luo <sup>b</sup>, Jing An <sup>c</sup>, Desong Wang <sup>d</sup>

(School of science, Hebei University of Science and Technology, Hebei, Shijiazhuang, 050018, china)

<sup>a</sup>xyli06@126.com; <sup>b</sup>lqz2004-1@163.com; <sup>c</sup>anjingsjz@yahoo.com.cn; <sup>d</sup>wangdesong@126.com

**Keywords:** Phenol degradation; Kinetics; Activation energy; TiO<sub>2</sub>/PANI nanocomposites;

**Abstract.** The kinetics and activation energy of photocatalytic degradation of phenol has been studied using the catalytically active TiO<sub>2</sub> and PANI modified TiO<sub>2</sub> nanoparticles. The reaction follows a pseudo-zero-order kinetics. Apparent activation energy of phenol photocatalytic degradation in water was 13.76kJ/mol by TiO<sub>2</sub> and was 12.31kJ/mol by TiO<sub>2</sub>/PANI.

## Introduction

In recent years, extensive research has shown that heterogeneous photocatalysis is a viable alternative to treat pollutions in water and air. More attentions have been paid to degradation of organic pollutions in wastewater using titanium dioxide photocatalyst because titanium dioxide could be used repeatedly without any noticeable deterioration of photoactivity and is non-toxic, photochemical stability and economical [1].

However, photo-generated electrons can recombine with holes very quickly and the wide band gap of TiO<sub>2</sub> (3.2 eV) only allows it to absorb the ultraviolet light (<387 nm). These disadvantages of TiO<sub>2</sub> result in a low efficiency of the photocatalytic activity in practical applications [2]. In recent years, nanocomposites of conductive polymers and inorganic particles have interesting physical properties and many potential applications. Polyaniline, polypyrrole and poly(3-hexylthiophene) modified TiO<sub>2</sub> can effectively improve the photocatalytic activity of TiO<sub>2</sub> catalyst under visible light and sun light [3-5]. Also, Polyaniline modified TiO<sub>2</sub> nanoparticles have higher photocatalytic activity than neat TiO<sub>2</sub> nanoparticles under UV light [6].

The photocatalytic oxidation of phenol is one of the most frequently studied reactions because phenolic compounds are widely used in industry and daily life [7]. How to eliminate phenolics in wastewater effectively has been in urgent demand. In the present paper, the photocatalytic degradation of phenol was chosen as a model reaction to evaluate the photocatalytic activities of TiO<sub>2</sub> and PANI modified TiO<sub>2</sub> catalysts. The apparent activation energies of photocatalytic degradation of phenol by TiO<sub>2</sub> and PANI modified TiO<sub>2</sub> catalysts were calculated.

## Experimental

### Materials

Phenol, ammonium peroxydisulfate and hydrochloric acid with AR grades were obtained from Tianjin Chemical Reagents Company and were used without further purification. Aniline was distilled before used. Nanoparticle TiO<sub>2</sub> was prepared in our laboratory with an average particle size of about 15nm.

### Preparation of TiO<sub>2</sub>/PANI composites photocatalyst

Polyaniline-modified TiO<sub>2</sub> composites were prepared by chemical oxidative polymerization of aniline in the presence of TiO<sub>2</sub> nanoparticles. Nanocrystalline TiO<sub>2</sub> particles were dispersed into HCl aqueous solutions with ultrasonic vibrations for 30min to obtain a uniform suspension. Quantitative aniline was added into this mixture dropwise under vigorously stirring in the ice-water bath, after which ammonium peroxydisulfate (APS) dissolved in HCl aqueous solution was added to the reaction vessel. Then the mixture was allowed to polymerize under stirring for 6h. Finally the polyaniline-modified TiO<sub>2</sub> nanoparticles were filtered and washed, then the nanocomposites were dried at 80 °C till the constant mass was reached. In this way, PANI modified TiO<sub>2</sub> nanocomposites were prepared.

### Degradation test of phenol

To evaluate the photocatalytic activity of photocatalyst, phenol aqueous solution was placed in a quartz photo reactor with 1g L<sup>-1</sup> TiO<sub>2</sub> or TiO<sub>2</sub>/PANI photocatalyst. The suspension was aerated prior and during the reaction (air flow rate  $v=10\text{L}\cdot\text{h}^{-1}$ ). After 30 min aeration the suspension was irradiated with high pressure Hg lamp (500W). The photo flux was about  $(0.20\pm 0.01)\text{kWm}^{-2}$ . The temperature inside the reactor was maintained at ca. 300 K by means of a continuous circulation of water in a jacket surrounding the reactor. Samples of 10 ml were withdrawn from the suspension every several minutes during the irradiation. The photocatalyst were separated from the solution by centrifugation and the quantitative determination of phenol was performed by measuring its absorption at 270 nm with a UV-vis spectrophotometer.

## Results and Discussion

### Effect of Initial Phenol Concentration on Degradation Rate

The mechanism of many photocatalytic reactions have been described in detail in the literatures and many of these are concerned with the degradation of organic and inorganic compounds [8,9]. During the photocatalytic process the catalyst is activated by photons. When the semiconductor, TiO<sub>2</sub>, is irradiated with photons of appropriate energy, the formation of an electron-hole pair occurs, and then these charges can either recombine or participate in different reactions. The dependency of the degradation rate on the concentrations is widely reported by means of the Langmuir-Hinshelwood (L-H) model in a batch reactor for a given light intensity combined with the assumption that the oxygen is adsorbed on different adsorption sites than the other products [10]. In generally, the L-H model is simplified by including the surface coverage of oxygen in an apparent kinetic parameter and by considering the initial degradation rate. Furthermore, the last assumption allows neglecting the intermediates which is difficult to estimate because all the major intermediates and by-products must have been identified. So L-H model expression becomes (1):

$$r = \frac{k_{obs} K_A [A]}{1 + K_A [A]} \quad (1)$$

Where  $k_{obs}$  is an apparent kinetic parameter depending on light intensity, mass and nature of the catalyst, and concentration of the electron carrier. For low concentration,  $K_A [A] \ll 1$ , Eq (1) reduces into  $r_0 = k_{obs} [A]$ , which is first order reaction. For high concentration  $K_A [A] \gg 1$ , the degradation rate is maximal and of order 0 with regard to the initial concentration. This expression is only valid at the beginning of the reaction when the by-products are produced in a negligible amount.

The change in concentration of phenol as a function of irradiation time and its dependence on the initial concentration of phenol is shown in Fig.1(a). It was observed that under experimental conditions the concentration of phenol was changed with linear when the initial concentration of phenol in the range of 0.21-0.85 mmol L<sup>-1</sup> was different. The degradation rate is of zero-order rate law. The rates obey the Langmuir-Hinshelwood relationship, the L-H kinetic equation was:

$$\frac{1}{r} = \frac{1}{kK} \bullet \frac{1}{C_0} + \frac{1}{k} \tag{2}$$

Where  $k$  is the rate constant,  $K$  is the adsorption constant of phenol on  $TiO_2$  from water and  $c_0$  is the initial phenol concentration, the plot of  $r^{-1}$  as a function of  $c_0^{-1}$  should yield a straight line. This hypothesis was verified through the double reciprocal plot shown in Fig.1(b). For the value of  $k$  derived from the intercept, and for  $K$  derived from the slope of the line, we obtained  $k = 0.0237 \text{ mmolL}^{-1} \text{ min}^{-1}$  and  $K = 3.259 \text{ mmol}^{-1} \text{ L}$ , respectively. The high adsorption constant supports the view that phenol is easily adsorbed over  $TiO_2$ .

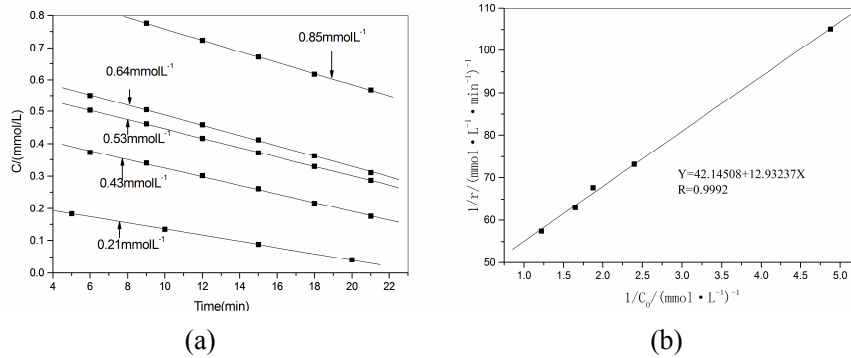


Fig.1 Effect of different initial concentration of phenol on degradation rate (a), linear relationship between reciprocal of initial rates ( $1/r$ ) and reciprocal of initial phenol concentration ( $1/c_0$ ) (b)

**Determination of Apparent Activation Energy**

The dynamics of phenol degradation at different temperature by  $TiO_2$  is shown in Fig. 2(a). It suggests that the decline of phenol concentration is linear relation with the degradation time, and it obeys zero-order reaction kinetics. Generally, the rate constant follows an *Arrhenius* temperature-dependence and increase exponentially with temperature.

$$k = Ae^{-E/RT} \tag{3}$$

Where  $k$  denotes the (temperature-independence) rate constant,  $E$  represents apparent activation energy,  $T$  is the reaction temperature,  $R$  is the gas constant. Results further confirm that raising the temperature increased the chemical reaction rate. It can be concluded the apparent activation energy of neat  $TiO_2$  from Arrhenius equation is  $13.76 \text{ kJ/mol}$ . Generally, the activation energy of chemical reactive is in the range of  $40\text{-}400 \text{ kJ/mol}$ . Therefore, the effect of temperature on reactive rate is very little in the photochemistry reactive.

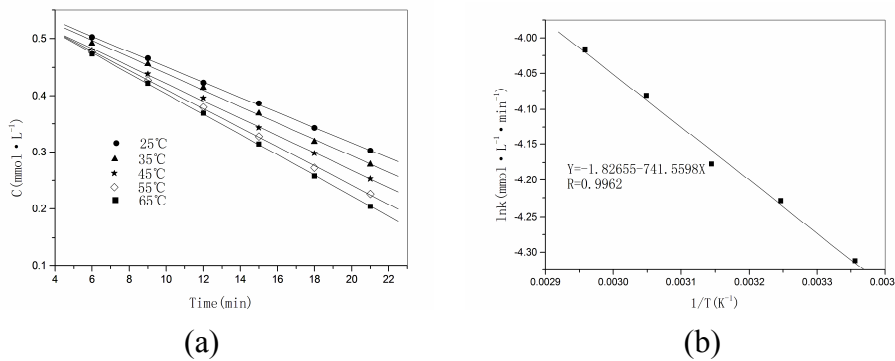


Fig.2 Dynamics of phenol degradation by  $TiO_2$  at different temperature (a), Relationship of degradation rate constants and temperature (b)

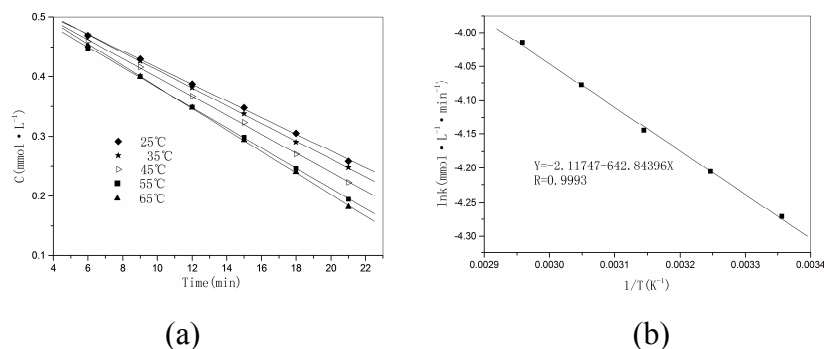


Fig.3 Dynamics of phenol degradation at different temperature by  $\text{TiO}_2/\text{PANI}$  composites(a)  
Relationship of degradation rate constants and temperature(b)

According to our former research, the introduction of about 1% PANI into  $\text{TiO}_2$  nanoparticles enhanced the photocatalytic activity significantly [6]. The optimal initial  $\text{TiO}_2/\text{ANI}$  molar ratio was 100: 1, so  $\text{TiO}_2/\text{PANI}$  composites with initial  $\text{TiO}_2/\text{ANI}$  molar ratio (100:1) was chose to degrade phenol aqueous solution. The dynamics of phenol degradation at different temperature by PANI modified  $\text{TiO}_2$  catalyst is shown in Fig. 3. Also, the apparent activation energy of phenol degradation by  $\text{TiO}_2/\text{PANI}$  composites is 12.31kJ/mol. Compared to  $\text{TiO}_2$ , phenol degradation apparent activation energy is lower about 1.45kJ/mol. So, the degradation rate of phenol by  $\text{TiO}_2/\text{PANI}$  composites improved.

## Conclusion

In this article, PANI modified  $\text{TiO}_2$  nanoparticles were prepared by in situ chemical oxidative polymerization method. The photocatalytic degradation of phenol and its reactive kinetics have been studied using nanoparticulate  $\text{TiO}_2$  and  $\text{TiO}_2/\text{PANI}$  nanocomposites. Results show the reaction follows a pseudo-zero-order kinetics under UV irradiation. Apparent activation energy of phenol phtocatalytic degradation in water by  $\text{TiO}_2$  and by  $\text{TiO}_2/\text{PANI}$  composites are calculated which are 13.76kJ/mol and 12.31kJ/mol respectively.

## Acknowledgement

This work has been supported by the National Natural Science Foundation of China (No.51002044) and the Natural Science Foundation of Hebei Province (No. B2010000846 and No. B2011208006).

## References

- [1] H.H. Huang, D.H. Tseng, L.C. Juang, J. Hazard. Mater. 156 (2008) 186-193
- [2] J F Zhu, Z G Deng, F Chen, et al, Appl. Cataly. B: Environm.62(2006): 329-335
- [3] X. Li, D. Wang, G. Cheng, *et. al.* Appl. Cataly. B: Environm. 81 (2008), 267-273
- [4] D. Wang, Y. Wang, X. Li, *et. al.* Cataly. Commun. 9(2008) 1162-1166
- [5] D. Wang, J. Zhang, Q. Luo, *et. al.* J. Hazard. Mater. 169 (2009) 546 - 550
- [6] X. Li, D. Wang, Q. Luo, J. An, Y. J. Chem. Technol. Biot. 83(2008)1558-1564
- [7] Z. Guo, R. Ma, G. Li. Chem. Enginee. J. 119 (2006) 55-59
- [8] Q. Hu, C. Zhang, Z. Wang, *et. al.* J. Hazard. Mater. 154 (2008) 795-803
- [9] D. Chatterjee, V. R. Patnam, A. Sikdar, *et. al.* J. Hazard. Mater. 156 (2008) 435-441
- [10] S. Brosillon, L. Lhomme, C. Vallet, *et. al.* Appl. Catal. B: Environm. 78 (2008) 232-241

## Effects of SiC Addition on the Properties of MgO-based Castables

Juncong Wei<sup>1,a</sup>, Junbo Tu<sup>1,b</sup>

<sup>1</sup>Hebei Province Key Laboratory of Inorganic Nonmetallic Materials, Hebei United University,  
Tangshan 063009, China

<sup>a</sup>tttwjc@126.com, <sup>b</sup>tujunbo@126.com

**Keywords:** SiC; Magnesia, Castable, Mechanical property, Slag resistance

**Abstract.** The effects of SiC addition on physical properties and slag resistance of MgO-based castables were investigated using magnesia as the main raw and silica micropowder as binder. The result revealed that with increasing SiC addition, dried strength decreased, medium and high temperature strength first increased and then decreased and reached a maximum at 3% SiC addition. The hot modulus of rupture (HMOR) of the materials maximized at 3% SiC addition. The slag penetration resistance of the castables was improved while resistance to slag attack was deteriorated with the increase in SiC addition. The materials exhibited optimum slag resistance at 3% SiC additions.

### Introduction

MgO-based castables, possessing the superior performance of polluting-free from molten steel and basic slag attack resistance, have found applications in metallurgical industry especially in the production of clean steel. However, the castables has some disadvantages such as low strength, high thermal expansion, poor thermal stability and structural spalling due to penetration of molten slag, which largely limit its wide use. To improve the performance of MgO-based castables, some oxides such as Al<sub>2</sub>O<sub>3</sub>, Cr<sub>2</sub>O<sub>3</sub>, ZrO<sub>2</sub>, TiO<sub>2</sub> were introduced to improve the slag penetration resistance, thermal stability and sinterability[1-4]. Some nonoxides, such as Si<sub>3</sub>N<sub>4</sub> and SiC, have low thermal expansion coefficient, good thermal stability and molten slag penetration resistance. Therefore, the properties of MgO-based castables are expected to be considerably improved when the nonoxides are introduced. Here the effects of SiC addition on the behavior of MgO-based castables were investigated.

### Experimental procedures

**Starting materials.** The main starting materials were sintered magnesia (8-5mm, 5-3mm, 3-1mm and 1-0mm respectively), fused magnesia (< 200 mesh), SiC and silica micropowder. Sodium tripolyphosphate was used as a dispersing agent. The chemical compositions of the main starting materials were tabulated in Table 1.

Table 1 Chemical compositions of main starting materials (wt. %)

Starting materials	MgO	CaO	SiO <sub>2</sub>	Fe <sub>2</sub> O <sub>3</sub>	Al <sub>2</sub> O <sub>3</sub>	C	SiC
Magnesia particles	96.51	1.02	0.97	0.70	0.65	-	
Magnesia fines	97.16	0.70	0.63	0.79	0.13	-	
Silica micropowder	0.1	0.2	97.5	0.1	0.4	0.5	
Silicon carbon	-	-	-	0.2	-	0.3	96.89

**Specimen preparation and testing.** The starting materials were weighed according to the predetermined formulas Table 2, dry mixed well, and wet mixed with addition of appropriate water. The mixtures were first formed at a vibrating bench into prism specimens of 160mm×40mm×40mm and then dried at 110°C for 24h, sintered at 1200°C and 1500°C for 3h respectively, and cooled naturally to room temperature.

Prism crucible samples of 70mm×70mm×70mm with a hollow core of 20mm×36mm were prepared by forming the well wet-mixed castables under vibration on a laboratory vibrating bench. The formed castables were cured for 24h in mould and another 24h after demoulding, and then dried at 110°C for 24h.

The permanent linear change, apparent porosity, bulk density, cold crushing strength and modulus of rupture (MOR) of the specimens were tested by national standard. The HMOR at 1400°C for 0.5h of resultant specimens were determined according to national standard GB-T3002-1982.

For crucible slag test, 20g steel slag from tundish was charged in the afore-described crucible, which was heated to 1500°C (3h soaking) in an electric furnace and then cooled naturally. The corroded area and penetrated area of the cut section of these crucibles after test were observed by naked eyes. The chemical analysis of the slag adopted is as follows: CaO 46.13; SiO<sub>2</sub> 16.22; Fe<sub>2</sub>O<sub>3</sub> 23.19; MgO 10.09; Al<sub>2</sub>O<sub>3</sub> 2.24; MnO 3.13.

Table 2 Formulations of specimens (wt. %)

Sample code	S-0	S-1	S-2	S-3	S-4	S-5
97 sintered MgO (8-1mm)	55	55	55	55	55	55
97 sintered MgO (1-0mm)	15	15	15	15	15	15
Electric fused MgO of 200 mesh	27	26	25	24	23	22
silica micropowder	3	3	3	3	3	3
SiC fines	0	1	2	3	4	5

## Results and Discussions

### Effects of SiC additions on the room temperature physical properties of MgO-based castables

**Behavior of the castables dried at 110°C for 24h.** Table 3, Fig. 1 and Fig. 2 show that the influence of SiC additions on permanent linear change, strength, bulk density and apparent porosity respectively. As SiC addition increases, the permanent linear change values gradually increases from negative values to positive values, strength gradually reduces, bulk density reduced and apparent porosity increase. The strength of the castables is mainly provided by the agglomerating and binding of MgO-SiO<sub>2</sub>-H<sub>2</sub>O system. The hydration of MgO to form Mg(OH)<sub>2</sub> also contributes to the strength of the material. When SiC addition increases, MgO content reduces correspondingly. Consequently, Mg(OH)<sub>2</sub> content reduces and the strength of the materials declines. Because the true density of silicon carbide powder is much lower than that of magnesia fines, the bulk density of the castables reduces and apparent porosity increases as the additions of silicon carbide increase.

Table 3 Effects of SiC additions on permanent linear change dried at 110°C for 24h (%)

Sample code	S-0	S-1	S-2	S-3	S-4	S-5
Permanent Linear Change/%	-0.01	-0.01	-0.01	0.01	0.01	0.03

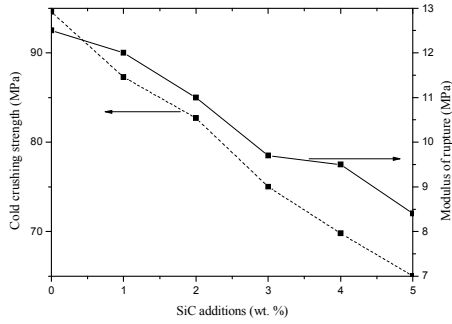


Fig.1 SiC addition vs strength after dried

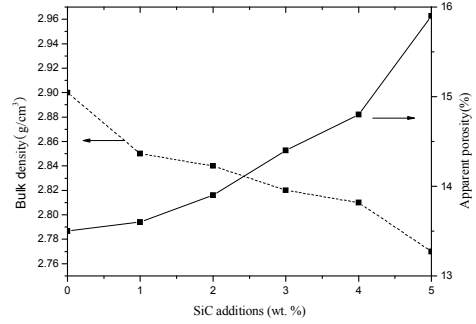
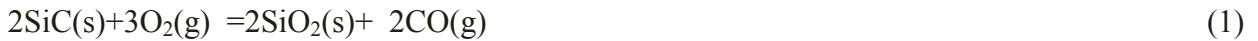


Fig.2 SiC addition vs density and apparent porosity after dried

**Behaviors of MgO based castables fired at 1200°C for 3h.** Table 4, Fig. 3 and Fig. 4 show that the influences of SiC additions on permanent linear change, strength, bulk density and apparent porosity fired at 1200°C for 3h respectively. As the addition of SiC increases, permanent linear change gradually increases, strength first increases and then reduces, bulk density reduces, and apparent porosity first reduces and then increases. The castables possesses greatest strength and least apparent porosity at 3% SiC addition.

During heat treatment at 1200°C, SiC will react with oxygen.



New formed SiO<sub>2</sub> is active and could react with MgO in the castables to form forsterite.



The reaction takes place accompanying a dimensional expansion. With the addition of SiC increases, the material becomes denser and the strength of the material increases. However, further increase in SiC addition would lead to poor sinterability due to the expansion reaction. Therefore, the structure of the material become loose and the strength of the materials begin to reduce.

Table 4 Effects of SiC additions on permanent linear change sintered at 1200°C for 3h (%)

Sample code	S-0	S-1	S-2	S-3	S-4	S-5
Permanent Linear change/%	-0.03	0.01	0.04	0.13	0.21	0.33

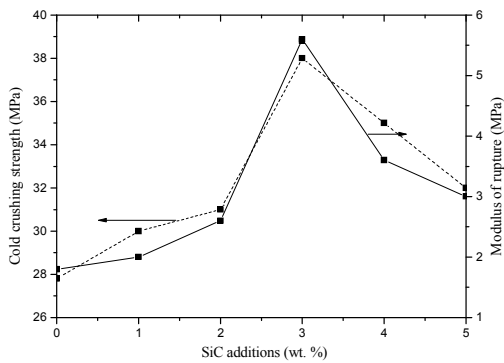


Fig.3 SiC addition vs strength after fired at 1200 °C for 3h

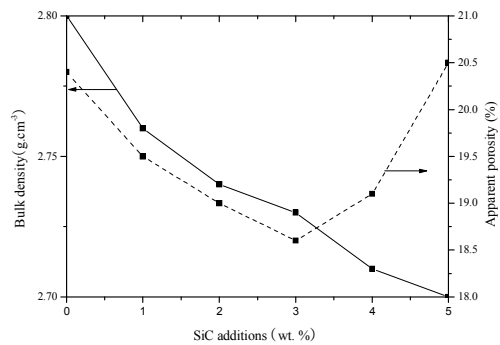


Fig.4 SiC addition vs density and apparent porosity after fired at 1200°C for 3h

**Behaviors of MgO based castables fired at 1500°C for 3h.** Table 5, Fig. 6 and Fig. 7 show the variation of permanent linear change, strength and apparent porosity and bulk density with the increase of SiC additions. As the addition of SiC increases, permanent linear change gradually increases, the strength of the castables first increase and then decrease, the apparent porosity first decrease and then increase.

SiC plays double roles during the sintering process at high temperature. On one hand, silica is formed due to the oxidation of SiC and reacts with MgO to form  $M_2S$ , which contributes to the sintering of the materials. On the other hand, SiC hinders the sintering at high temperature. Take the two factors into considerations, the behavior of the castables fired at 1500°C exhibit the above behaviors.

Table 5 Effects of SiC additions on permanent linear change sintered at 1500°C for 3h (%)

Sample code	S-0	S-1	S-2	S-3	S-4	S-5
Permanent Linear Change/%	-0.48	-0.41	-0.16	0.03	0.24	0.35

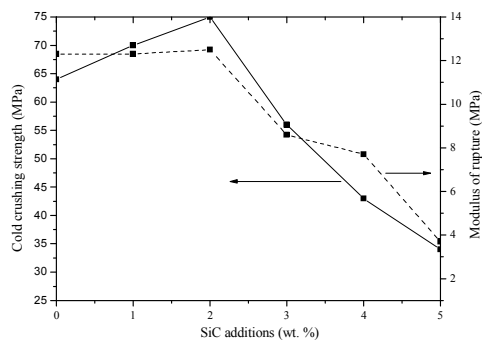


Fig.5 SiC addition vs strength after fired at 1500 °C for 3h

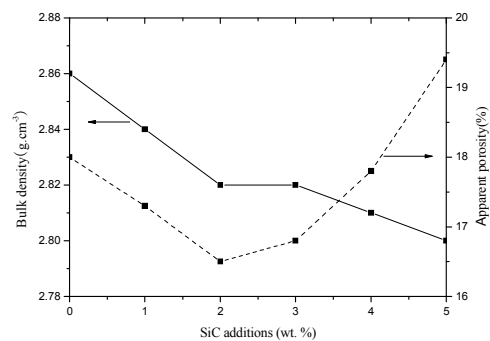


Fig.6 SiC addition vs density and apparent porosity after fired at 1500°C for 3h

**Effect of SiC addition on the hot modulus of rupture of the MgO-based castables.** Table 6 is the HMOR of the castables changes with the increase in SiC addition. The MOR first increased and then decreased and reached a maximum at 3% SiC addition.

Table 6 Hot modulus of rupture of MgO-based castables at 1400°C for 0.5h

SiC(wt. %)	0	1	2	3	4	5
Strength/Mpa	1.27	1.38	1.63	1.85	1.80	1.59

**Effects of SiC addition on the slag resistance of MgO-based castables.** Fig. 7 is the photo of the crucible samples after slag test. It can be observed that as the addition of SiC increases, slag penetration resistance increase while slag attack resistance decreases. This is because silicon carbide reacts with oxygen at high temperature to form viscous protective film of silica over the surface of the specimen, which hinders the penetration of molten slag. The SiC remained in the interior could not wet with slag, which could markedly improved the slag penetration of MgO-based castables. As the addition SiC increases, the slag penetration resistance gradually increases. However, the content of  $M_2S$  formed in the specimen increase, which leads to the reduction of the slag attack resistance. In conclusion, the castables possess the optimum overall slag resistance at 3% SiC addition.

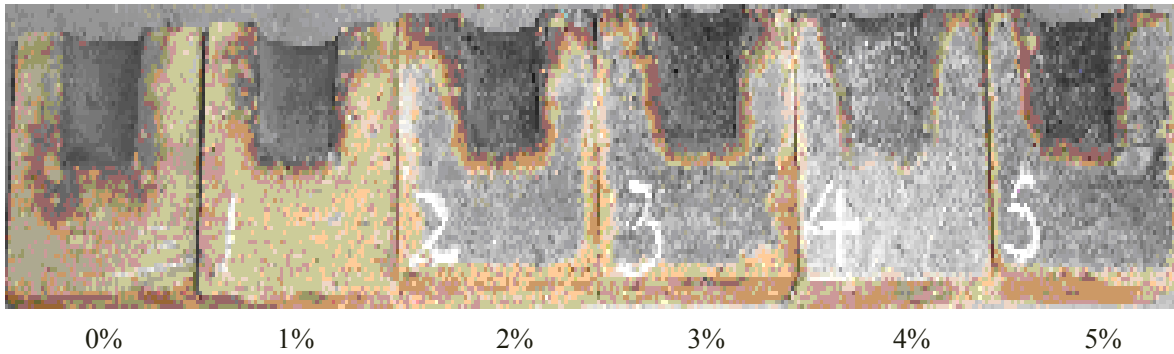


Fig.7 Photo of the specimens of different SiC additions after slag test

### Conclusions

- (1) As the additions of SiC increased, apparent porosity slightly increased, bulk density and strength of the castables dried at 110°C for 24h reduced; The strength of the castables fired at 1200°C and 1500°C first increased and then reduced.
- (2) The hot modulus of rupture at 1400°C for 0.5h first increased and then reduced, and reached a maximum at 3% SiC addition;
- (3) With the increase in SiC addition, the slag penetration resistance of the castables increased while slag attack resistance decreased. The castables possessed optimum slag resistance at 3% SiC addition.

### Acknowledgement

The financial support of the Educational Departement of Hebei Province (No: 2010131) are gratefully acknowledged.

### References

- [1] Junbo Tu, Jialin Sun, Ranruo Hong. Refractories Vol. 39(1) (2005), p.14-6(in Chinese)
- [2] Sanhua Zhang, Zhenyou Bi, Ningsheng Zhou, etc. Refractories Vol. 33(3) (1999), p.150-153(in Chinese)
- [3] Zhigang Li, Fangbao Ye, Xiangchong Zhong. Refractories Vol. 35(6) (2001), p.320-322 (in Chinese)
- [4] Yousheng Li, Nan Li, Yingdong Wang. Refractories Vol. 36(2) (2002), p.86-87(in Chinese)

## Selective Etching of Pressure-Crystallized Bisphenol-A Polycarbonate by Dimethylacetamide at Room Temperature

Jun Lu<sup>1, a</sup>, and Rui Huang<sup>2, a</sup>

<sup>1</sup>Key Laboratory of Advanced Technologies of Materials, Ministry of Education, School of Materials Science and Engineering, Southwest Jiaotong University, Chengdu 610031, Sichuan, P. R. China

<sup>2</sup>College of Polymer Materials Science and Engineering, Sichuan University, Chengdu 610065, Sichuan, P. R. China

<sup>a</sup>junluprc@hotmail.com

**Keywords:** Bisphenol-A polycarbonate, crystal morphology, etching, growth, high pressure

**Abstract.** The high-pressure crystallized bisphenol-A polycarbonate (BAPC) and BAPC / dioctyl phthalate (DOP) blend samples were prepared in a piston-cylinder apparatus, and the recovered specimens were investigated using scanning electron microscopy (SEM). As for the fracture surfaces without etching technique applied, the detailed information of the crystal morphologies of BAPC was not shown, though the outlines of such aggregations as spherulites and cylindrulite were still exposed due to the high-temperature degradation during the long time crystallization. However, the delicate internal structures of these aggregates were revealed clearly by the introduction of a facile etching method. The used etchant, dimethylacetamide, was capable of dissolving only amorphous, but not crystalline BAPC at room temperature. With the employed selective etching technique, BAPC spherulites with fine structures and different characteristics were observed. Spatial dendrites of the polymer were also disclosed in BAPC samples plasticized with DOP after a deep etching process. Furthermore, by controlling the etching process, unique hierarchical structures, composed of nano-structured micrometer-sized crystalline entities of BAPC, was created on the fracture surfaces. The study presented here suggested that selective etching is a more effective route to reveal the inner structures of polymer crystals, as well as to fabricate new surface active materials, such as a super-hydrophobic surface with self-cleaning effect.

### Introduction

There are both scientific and technological reasons for studying the internal morphologies of polymers. A route to provide the information on lamellar organization, widely employed by the community, is the one called etching. Etching is the process of using strong acids or oxidants to cut into the unprotected parts of a polymer surface, which destroys the amorphous region and reveals the crystalline patterns, such as permanganic etchant for polyolefines and orthophosphoric acid for poly (aryl-ether-ether-ketone) [1].

BAPC is an ideal subject for the investigation of polymer crystallization, which has been used as an engineering polymer of high performance, due to its excellent toughness, weatherability and transparency. A procedure has been described which permits the classification of solvents according to their effect on the polymer [2]: class I -dissolve amorphous or crystalline BAPC; class II -dissolve only amorphous BAPC; class III-convert amorphous BAPC to crystalline BAPC; class IV -none of the above.

Achieved by creating the desired crystal morphologies with ideal molecular orientation during the processing, solid phase forming under high pressure is a more effective route to produce polymer products with greatly improved physical and mechanical properties [3, 4]. In this work, a facile etching route was introduced to reveal the morphologies of high-pressure crystallized BAPC samples. Some novel crystal forms were observed by the used etchant, dimethylacetamide, which dissolved only amorphous BAPC at mild temperatures.

## Experimental Procedure

**Materials.** BAPC in pellets was a commercial product supplied by Changfeng Chem. Co., Chongqing, China. The viscosity-average molecular weight, calculated from intrinsic viscosity, was about 27500. An analytical-grade DOP used as a plasticizer was provided by Tianjin Chem. Co., Tianjin, China. By using a Haake Rheocord 90 torque rheometer equipped with a co-rotating twin screw extruder, BAPC and DOP was melt-blended. The temperature profile used for the extruder was 200, 250, 265 and 220°C from hopper to die and the screw rotation was maintained at 30rpm.

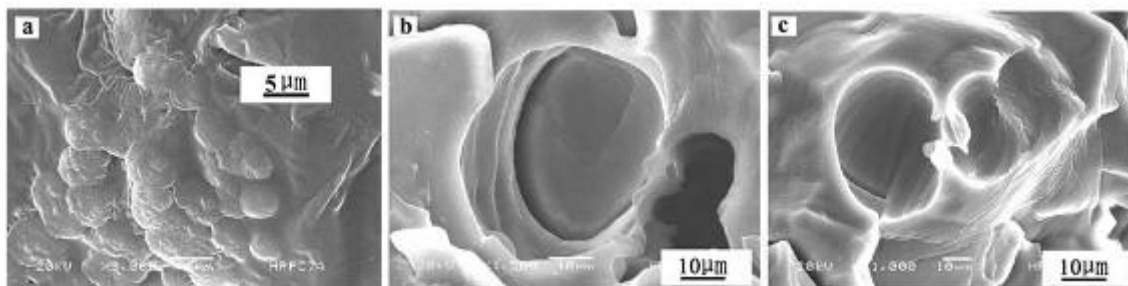


Fig. 1. Secondary electron images of the spherulites in the BAPC sample, crystallized at 200MPa, 300°C for 240h (a), and the cylindrilite in the BAPC sample, crystallized at 200MPa, 300°C for 120h and then annealed at 200MPa, 320°C for 120h (b and c). No etching technique was applied.

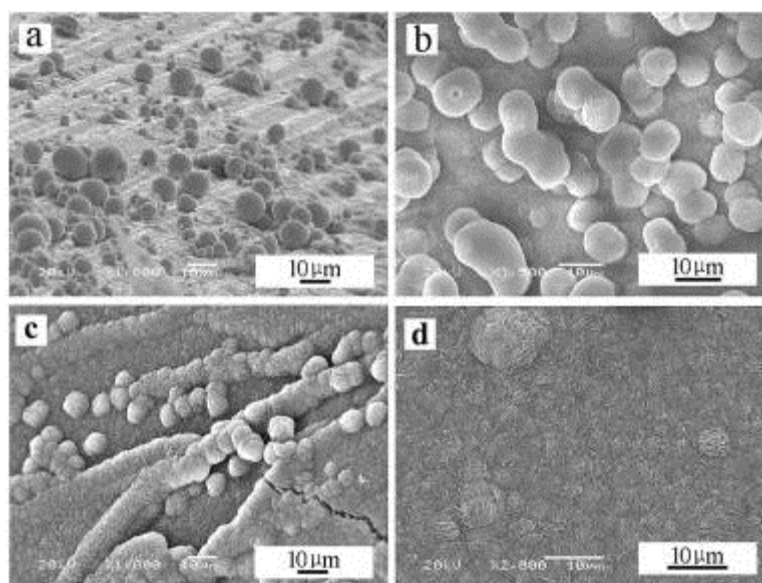


Fig. 2. Secondary electron images of the spherulitic forms in the BAPC sample, crystallized at 200MPa, 300°C for 120h and then annealed at 200MPa, 320°C for 120h: (a) no etching technique was applied; (b-d) the fracture surface was etched by dimethylacetamide at 25°C for different times.

**Sample Preparation.** High-pressure experiments were carried out with a piston-cylinder high-pressure apparatus [4]. The following procedure for crystallization was used. After loading the sample, low pressure (50MPa) was applied and temperature was raised to a predetermined level. After equilibrium was established, the pressure was raised to the desired value. The samples were kept under these conditions for a predetermined time, and then quenched down to ambient condition.

**Characterization.** SEM observations were carried out on a JEOL-JSM-5900LV instrument. The fresh surfaces of the samples were obtained through fracture at liquid N<sub>2</sub> temperature, which were further coated with gold for the detections. Prior to the gold treatment, the surfaces were etched by dimethylacetamide at 25°C for a given time.

## Results and Discussion

Fig. 1a gives out the secondary electron image of the representative spherulitic forms obtained in a pressure-crystallized BAPC sample, which impinged with one another during the growth process and became polyhedral. A cylindrolite was also observed on the fracture surface of another BAPC sample (Fig. 1b), crystallized at somewhat different conditions. The diameter of the cylinder was much larger than that of the mature spherulites grown in the same system. The even top plane of the body could be exposed easily, while most of the lateral surface was embedded in the amorphous matrix. This can possibly indicate that there were more tie-chains between the amorphous part and the cylindrolite along the lateral surface. Some cylindrolites may be stuck on the other surface during the fracture, which resulted in the cylindric holes on the observed surface (Fig. 1c). Although the outlines of such aggregations were still exposed due to the high-temperature degradation during the long time crystallization, the detailed inner structures of the polymer crystals were not revealed at all on such untreated fracture surfaces.

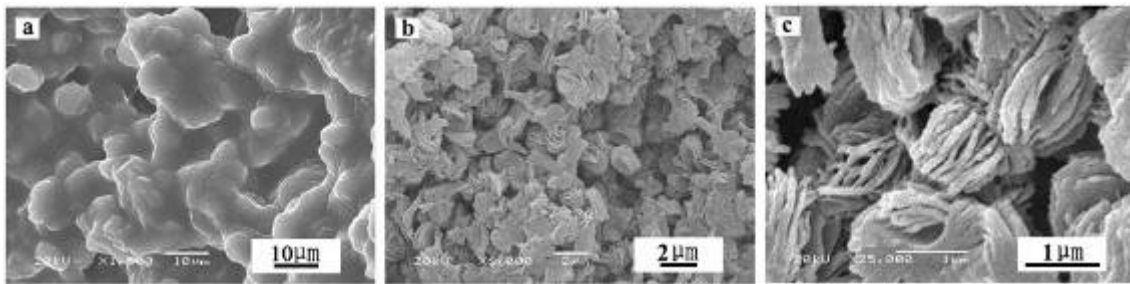


Fig. 3. Secondary electron images of the spherulites grown in the BAPC/DOP (90/10, wt/wt) blend sample, crystallized at 200MPa, 290°C for 24h: (a) no etching technique was applied; (b) the fracture surface was etched by dimethylacetamide at 25°C for 6h; (c) zoom-in view of the spherulitic structures designated in (b).

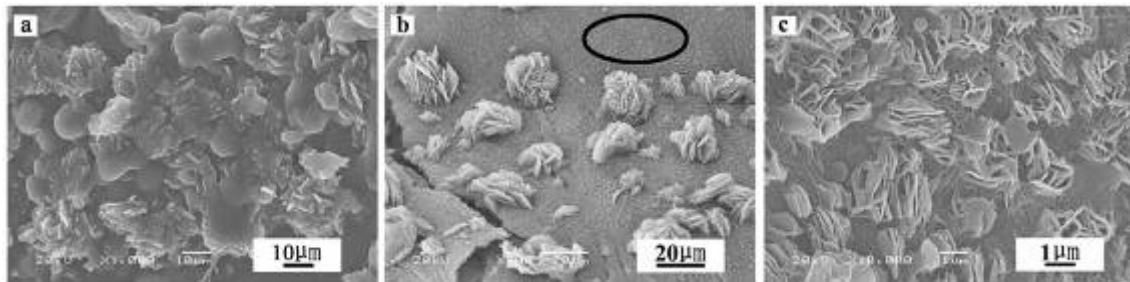


Fig. 4. Secondary electron images of the spherulitic structures formed in the BAPC/DOP (90/10, wt/wt) blend sample, crystallized at 300MPa, 290°C for 24h: (a) no etching technique was applied; (b) the fracture surface was etched by dimethylacetamide at 25°C for 6h; (c) the magnified image of the part highlighted by an elliptic frame in (b).

Fig. 2a displays a secondary electron image of the fracture surface of the BAPC sample crystallized at 200MPa, 300°C for 120h and then annealed at 200MPa, 320°C for 120h. Only global aggregates were observed if no etching technique was applied. However, etched by dimethylacetamide at 25°C to remove the non-crystalline parts, the detailed internal information of the smooth balls was revealed gradually with the etching time increased (Figs. 2b-c). The fine structures of the BAPC spherulites were detected clearly and the observed dense branches indicated that the fibrils within the body diverged frequently during the growth along the radial directions. The growth of BAPC crystals was hastened by the introduction of a plasticizer DOP, and spherulitic structures of the polymer became more open, as shown in Figs. 3 and 4. For the spherulitic forms grown in the BAPC/DOP blend systems, an abundance of information on lamellar organization was provided by the applied selective

etching technique (Figs. 3b and c; Figs. 4b and c), which would otherwise be largely inaccessible (Figs. 3a and 4a). The deep etching by dimethylacetamide at room temperature also disclosed certain novel crystal morphologies. Fig. 5 shows the secondary electron images of the spatial dendrites of BAPC with denser structures and different characteristics, which were induced by DOP at high pressure. Furthermore, the morphologies in Figs. 2d and 4c may give some interesting indications on the design of new surface active materials. As shown, unique hierarchical structures, composed of nano-structured micrometer-sized crystalline domains, were created on the BAPC samples, which were thought to be the basic physical structures of a super-hydrophobic surface with lotus effect [5].

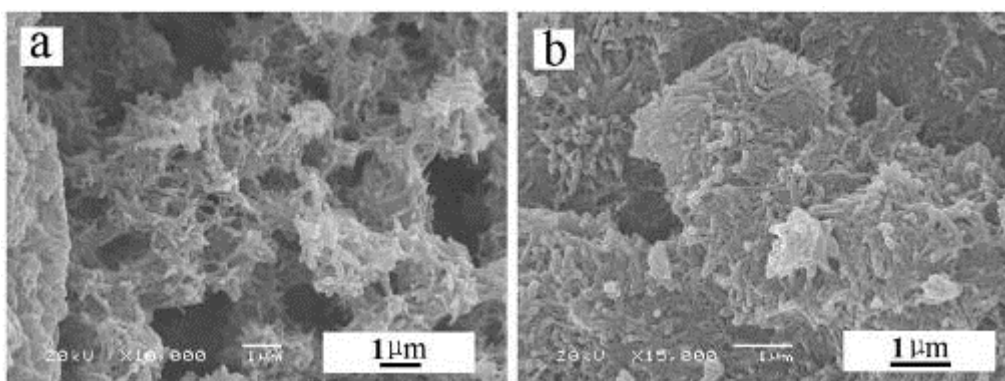


Fig. 5. Secondary electron images of the dendritic crystals in the BAPC/DOP blend samples, crystallized at: (a) 600MPa, 290°C for 24h, 10wt.-% DOP; (b) 200MPa, 250°C for 6h, 20wt.-% DOP. The fracture surfaces were etched by dimethylacetamide at 25°C for 6h.

### Summary

In conclusion, based on the morphological observations by SEM, a facile selective etching method was introduced for BAPC. The new usable etchant, dimethylacetamide, evidently revealed the spherulitic details at room temperature. Novel three-dimensional dendritic crystals with different characteristics were also revealed by a deep etching manner. Furthermore, unique hierarchical crystalline structures, potential for functional applications, were created by controlling the etching process.

The authors gratefully acknowledge the National Natural Science Foundation of China (Grant Number 50973089), the Fundamental Research Funds for the Central Universities (Grant Number SWJTU11CX056), and the Project Sponsored by the Scientific Research Foundation for the Returned Overseas Chinese Scholars, State Education Ministry, for the financial support of this research. The authors extend their gratitude to Professor Liangbin Li, University of Science and Technology of China, for valuable discussions.

### References

- [1] R.H. Olley, D.C. Bassett and D.J. Blundell: *Polymer* Vol. 27 (1986), p. 344
- [2] H.L. Heiss: *Polym. Eng. Sci.* Vol. 19 (1979), p. 625
- [3] J.A. Gonzalez-Leon, M.H. Acar, S.W. Ryu, A.V.G. Ruzette and A.M. Mayes: *Nature* Vol. 426 (2003), p. 424
- [4] J. Lu, R. Huang and I.K. Oh: *Macromol. Chem. Phys.* Vol. 208 (2007), p. 405
- [5] X. Gao, L. Jiang: *Nature* Vol. 432 (2004), p. 36

# Li<sup>+</sup> Extraction/Insertion Reaction with LiTi<sub>1.25</sub>O<sub>3</sub> Spinel in the Aqueous Phase

Jinhe Jiang

Department of Chemical Engineering, Weifang University 261061, China

Jiangjinhe2012@126.com

**Keywords:** Extraction/insertion reaction, Spinel-type metal oxides, Ion-exchange mechanism, LiTi<sub>1.25</sub>O<sub>3</sub>

**Abstract.** Spinel-type metal oxides, lithium-titanium oxide(LiTi<sub>1.25</sub>O<sub>3</sub>), was prepared by a solid state reaction crystallization method. The extraction/insertion reaction with this material was investigation by X-ray, saturation capacity of exchange, and K<sub>d</sub> measurement. The experimental results have proved that the acid-treated sample has a capacity of exchange 5.9 mmol • g<sup>-1</sup> for Li<sup>+</sup> in the solution.

## Introduction

The inorganic ion-exchange preparation has the advantage of thermo-stability and radiation resistance, synthesis simple and good selectivity etc. Apart from that, it appears the fine speciality in dealing with nuclear waste, gathering and separating of metal ions and chromatogram analysis[1-2].

In this paper, the solid state reaction crystallization method was used to synthesize the LiTi<sub>1.25</sub>O<sub>3</sub> of spinel-type oxide, whose composition and structure are different from those in literature[3-4]. The experimental result have proved that the inorganic material has good selectivity and higher capacity of exchange for Li<sup>+</sup> in the solution removed Li<sup>+</sup> previously. Moreover, the cost is cheap and its application prospect is significant.

## Experimental section

**Reagent and Instruments.** Li<sub>2</sub>CO<sub>3</sub> and TiO<sub>2</sub> were all analytical reagents; pure ethanol; D/max-A type X-ray diffraction instrument; Dx-170 type ion chromatogram instrument; XQM planetary ball mill; AA-670 atom absorption spectrum instrument; tubular-furnace.

**Synthesis and Identifiable of LiTi<sub>1.25</sub>O<sub>3</sub>.** The pure ethanol was dropped into a XQM planetary ball mill mixed powder of Li<sub>2</sub>CO<sub>3</sub> and TiO<sub>2</sub> with a Li /Ti mole ration of 1:1.25 at the condition of constant rate churning. After 8 hours, the mixture was mixed Completely. After mixing fully, The mixture was pressed to tablet by tablet press machine. Then the tablet was heat-treated for 4.5h at 775°C to obtain the Li-Ti oxide, the sample was designed as LiTiO-775, whose theoretical formula was LiTi<sub>1.25</sub>O<sub>3</sub>. Then it was analysed of x-ray diffraction and compared to literature[3-4].

Composition analysis: A 0.2g portion of sample was dissolved with acid. The Li and Ti contents were determined by atomic absorption spectrometry.

**The Cation Extraction of LiTi Oxide and Acid Modification.** Four 0.200g portions of sample (LiTiO-775 oxides) were immersed in a HNO<sub>3</sub> solution (50ml) of 0.01M, 0.1M, 1M and 10M respectively with shaking in constant temperature water at 25°C. After 3 days, take the supernatant solution to determine the cation concentration, test its acid proof ability and the extraction ration of Li<sup>+</sup>, Ti<sup>2+</sup>.

A 5g portion of sample (LiTiO-775) was immersed in a 1M HNO<sub>3</sub> solution (500mL) with intermittent shaking in constant temperature water at 25°C. After 7 days, remove the supernatant solution and add new HNO<sub>3</sub> solution. Repeating that for twice, then the initial sample was transformed to H-type sample, washed with water and air-dried. The sample obtained by thermal crystallized at 775°C and acid modified was designated as LiTiO-775(H). The composition was determined by the method referred in 1.2, and the H content was calculated by subtraction method.

**Saturation Capacity of Exchange.** Eight five 0.5g portions of LiTiO-775 (H), then each portion was immersed in a 0.1M solution (10mL), containing  $\text{Li}^+$ ,  $\text{Na}^+$ ,  $\text{K}^+$ ,  $\text{Rb}^+$  and  $\text{Cs}^+$  respectively, diluted to 100mL, shaken in constant temperature water at 25°C. After saturation exchanging (namely, after 10 days by literature[3-4]) the solutions were filtered by subminiature aperture sieve, and the cation concentration was determined. At the same time, do vacant experiment. Last, the inorganic exchanger saturation capacity of exchange for alkali-metal-ions obtained by decrease quantity.

**Distribution Coefficient (Kd).** After weighing four 0.100g portions of LiTiO-775 (H), each portion of sample was immersed in a 0.05M mixed solution (0.200mL) containing  $\text{Li}^+$ ,  $\text{Na}^+$ ,  $\text{K}^+$ ,  $\text{Rb}^+$  and  $\text{Cs}^+$  ( $\text{Cl}^-/\text{OH}^-$  ratios are different in each solution,  $\text{C}(\text{Cl}^-)+\text{C}(\text{OH}^-)=0.1\text{M}$ ,  $\text{C}=\text{Li}^+$ ,  $\text{Na}^+$ ,  $\text{K}^+$ ,  $\text{Rb}^+$  and  $\text{Cs}^+$ ). The alkali-metals ions total concentration all was  $1.0 \times 10^{-3}\text{M}$  by adding 9mL distilled water. After the samples were shaken for 7 days in constant temperature water at 25°C and were filtered, cation concentrations in each samples were obtained.

## Results and Discussion

**Compound and Appraisalment of  $\text{LiTi}_{1.25}\text{O}_3$ .** The X-ray diffraction pattern of compound metal oxide ( $\text{LiTi}_{1.25}\text{O}_3$ ), crystallized was shown in figure 1. The structure of compound metal oxide  $\text{LiTi}_{1.25}\text{O}_3$  crystallized at 775°C was much perfect.

We know from chemical analysis, the composition of LiTiO-775 is  $\text{Li}_{0.97}\text{Ti}_{1.22}\text{O}_{2.95}$ , whose chemical component is basically corresponded with the composition of spinel-type metal oxides.

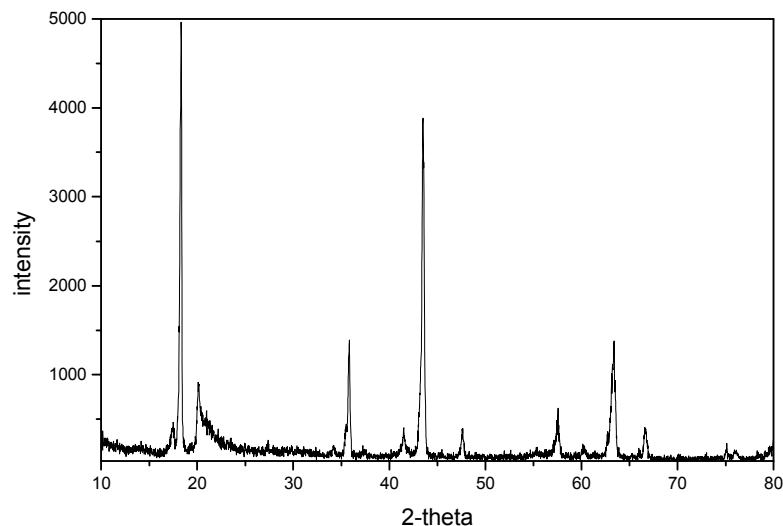


Fig.1 The powder's X-ray figures of  $\text{Li}_{0.97}\text{Ti}_{1.22}\text{O}_{2.95}$  crystal

**Cation Extraction of Compound Oxide LiTiO and Acid Modification.** The extraction ration of  $\text{Li}^+$  and  $\text{Ti}^{4+}$  from LiTiO-775 in different concentration  $\text{HNO}_3$  solution is shown in figure 2. we know from figure 2, the extractabilities of  $\text{Li}^+$  are 49%~91%, and  $\text{Ti}^{4+}$  are 2.6%~6.9%. Those indicate that the extractabilities of  $\text{Li}^+$  are higher than  $\text{Ti}^{4+}$  when exchanger was immersed in 1M acid solution, corresponding with the exchanger condition was better.(1 N,  $\text{Li}^+$  84%,  $\text{Ti}^{4+}$  5.2%)

The analysis indicate the composition of LiTiO-775(H) was  $\text{H}_{0.81}\text{Li}_{0.16}\text{Ti}_{1.16}\text{O}_{2.80}$ , whose component of 84%  $\text{Li}^+$  transformed to  $\text{H}^+$  compared with the composition  $\text{Li}_{0.97}\text{Ti}_{1.22}\text{O}_{2.95}$  before acid-treated. Then the specific  $\text{Li}^+$  of exchanger were extracted fulfill basically and remained the H-type identified with initial type.

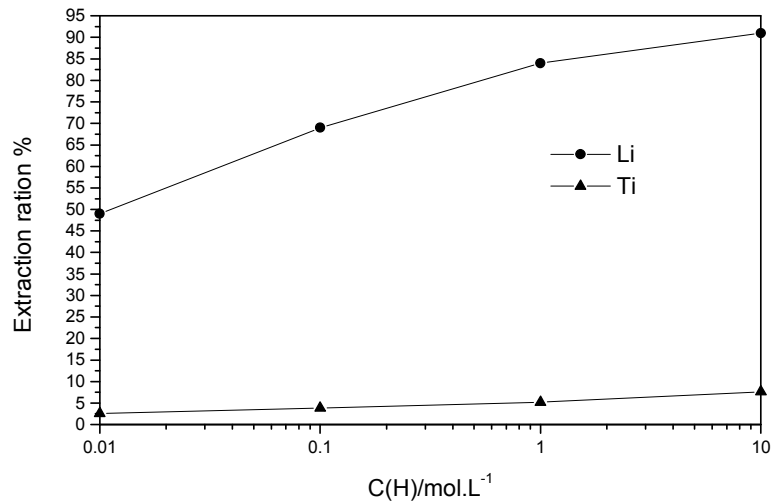


Fig.2 Extraction ration of cations from LiTiO-775 in nitric acid solution

**Saturation Capacity of Exchange.** The relation between radius and saturated ion exchange capacity of LiTiO-775(H) for alkali was shown in figure 3. Known from figure 3, the capacity of exchange for  $\text{Li}^+$  was much higher than those for other alkali ions. The capacity for  $\text{Li}^+$  is  $5.9 \text{ mmol} \cdot \text{g}^{-1}$ . It prove that the ion exchange synthesized has higher capacity of exchange, and better remembering of exchange for  $\text{Li}^+$ . The effect factors of saturation capacity of exchange of LiTiO-775(H) are: 1) The  $\text{Li}^+$  in exchange solution must be removed previously, because  $\text{Li}^+$  exchange with exchanger vacancy site when existing too much  $\text{Li}^+$ ; 2) The experimental results shown that the exchange capacity of ion exchanger for  $\text{Li}^+$  is much higher than those for other alkali ions in thin solution, which indicate that the ion-exchange reaction is carried out between and bare ions; 3) At the time of exchange, a  $\text{Li}^+$  was replaced by one  $\text{H}^+$ .  $\text{Li}^+$  not only entered the vacancy site but also exchange with the  $\text{H}^+$  of surface. Therefore, LiTiO-775(H) has a higher exchange capacity for  $\text{Li}^+$ .

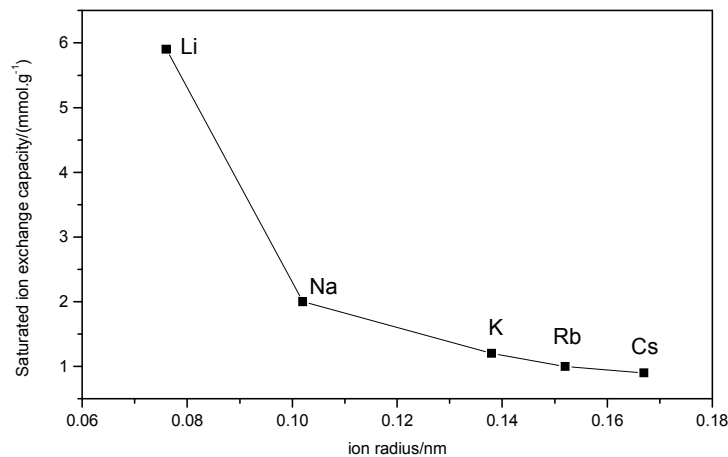


Fig.3 Relation between ion radius and saturated ion exchange capacity of LiTiO-775 (H) for alkali ions

**Distribution coefficient(Kd).** Kd values can be the token of exchange selectivity of LiTiO-775 (H) for correlate ions. Shown in figure 4, Kd values of LiTiO-775(H) for alkali ions are larger and larger with an increase pH over the pH region studied. The selectivity sequence of LiTiO-775(H) for alkali metal ions as follows:

$$\text{Li}^+ > \text{Cs}^+ > \text{Rb}^+ > \text{K}^+ > \text{Na}^+ \quad (1)$$

It indicates that LiTiO-775(H) has a better ion selectivity for  $\text{Li}^+$ . Ion-exchange reaction is reversible reaction. The reaction of  $\text{H}^+$  in ion-exchanger with alkali metal ions in solution as follows(example for  $\text{Li}^+$ ):

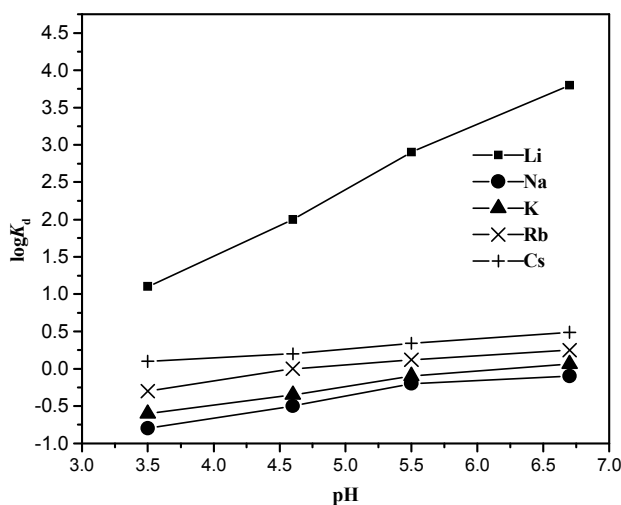


Fig.4 Distribution coefficient of LiTiO-775 (H) for alkali ions

## Conclusions

The comprehensive results indicate that the  $LiTi_{1.25}O_3$  of spinel-type metal oxide show a capacity extraction/insertion of  $Li^+$  in the aqueous phase, mainly by an ion-exchange mechanism. The  $Li^+$ -extracted samples show a high selectivity and a large capacity for  $Li^+$  among alkali metal ions.

## References

- [1] Z.Peng: S.Synthesis and electrochemical studies on spinel phase  $LiMn_2O_4$  cathode material prepared by different proceses, J. Rare Metal, 1999,18(2),143
- [2] Z.S.Peng, Y.S.Yan, C.Y.Jiang, C.R.Wan, H.C.Gao: Advance on extraction lithium from salt lake,.J.Chemistry Online. 1997,(12),11
- [3] Y.F.Liu, Q.Feng, Kenta Ool: Li extraction/insertion reaction with  $LiAlMnO_4$  and  $LiFeMnO_4$  spinels in the Aqueous phase, J.Journal of Colloid and Interface Science . 1994,163(1),130
- [4] H.Zhong: Prpperty of  $H_2TiO_3$  type ion-exchangers and extraction of lithium from brine of natural gas wells J.Chinese Journal of Applied Chemistry.2000,17(3),307

# Sheet single point vibration incremental forming process simulation and analysis of process parameters

Cai Gaipin<sup>a</sup>, Xing Congwen<sup>b</sup>, Jiang Zhihong<sup>c</sup>, Zhang Zhongkai<sup>d</sup>

(School of Mechanical and Electrical Engineering, Jiangxi University of Science and Technology, Ganzhou 341000, China)

<sup>a</sup>cgp4821@yahoo.com.cn, <sup>b</sup>xingcongwen@163.com, <sup>c</sup>jzhee\_mail@163.com

**Keywords:** Incremental forming, simulation forming, metal plastic forming

**Abstract.** The deformation of vibration incremental forming process for sheet metal is in high complexity, theory research is not perfect. This subject using DEFORM simulation software, joined the vibration on the forming process of tool head and simulated the forming process base on different tool radius and vibration parameters. Simulation result indicated that vibration in greatly reduced the stress of the forming tool head. The right vibration parameters smoothed out the forming force largely, reduced sheet metal stress concentration, improved product quality and product yield. That has a higher degree of study and use value.

## 1 Introduction

With the development of society, increased competition in the market, and how business can develop new products quickly, low cost and high quality, changing mold production of large investments, the production of long-period in the past to meet changing market needs for wide variety of products in small batches, be the key to business survival and development. Incremental forming is an advanced means to solve this problem. The technology has broad application prospects and tremendous economic value, in vehicles, aircraft, appliances, and so the development of the industry. [1~3]

Incremental forming based on "layered manufacturing", put pressure on sheet metal part by the point and side-by-layer process of accumulation the deformation to production. It's a new die less mold forming technology. The plastic deformation of materials sheet is complex in deformation process and fundamental research is not perfect. [4] This paper simulated the forming process by simulation software, respectively changing technology such as vibration amplitude and frequency and the tool radius parameter. Results show that the vibration reduced forming force and some forming laws and the appropriate parameters were found.

## 2 Model of single point incremental forming of sheet metal to create

DEFORM simulation software is a powerful software, material flow, and is well suited for large deformation State simulation in the field of research. Because the software does not have the function of three-dimensional modeling, solid model of this subject is built in the PRO/E software and import the software. Solid model is shown in Fig.1.

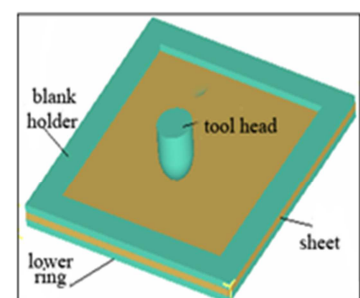


Fig.1 entity model

Model, tools selected for rigid body, alloy steel; low carbon steel 08AL of sheet steel. The mechanical properties are in table 1. Numerical simulation of single point incremental forming process, the tool head configuration rules, using the absolute element mesh, bound in rotational degree; sheet and blank holder shape simple, the relative grid partition, the X, Y direction fixed. [5]

Table 1: Tool head and sheet metal mechanics performance indicators

	density	yield strength	tensile strength	elastic modulus	shear modulus	Poisson's ratio
	Gpa	Mpa	Mpa	Gpa	Gpa	
Sheet material	7850	165.79	290.69	188.78	79.4	0.324
Tool head	7900	785	980	206	80.6	0.3

### 3 Different vibration amplitude and frequency to the influence of the incremental forming

In simulation experiment, set the sheet metal thickness  $h=1\text{mm}$ . Select parameter is: feed content  $\Delta h = 0.25\text{mm/s}$ , the tool radius  $r=5\text{mm}$ , select a different vibration frequencies and amplitudes of parameters to compose 10 experiments. It is shown in table 2.

Table 2: Experiment parameter table

Group		I			II			III			
plan		1	2	3	4	5	6	7	8	9	10
amplitude	A(mm)	0	0.08	0.08	0.08	0.15	0.15	0.15	0.3	0.3	0.3
frequency	F(Hz)	0	30	50	100	30	50	100	30	50	100

Put parameters above previously to the established model, then Operate simulation and get the forming and shaping time relationships fig.2. Plan 1 is the forming force curves without vibration. As a reference curve, it has no change in three charts of Fig.2. Forming force reaches the maximum value from 0N in the 0-5s at the beginning of the forming force, near 1600N, in the 5-10s drop and stabilized at 1400N until end of the simulation.

Compared to plan 1, other plans show that: 1, vibration substantially reduced forming force; 2, which greatly improved the rate of change. Vibration reduces the work pressure forming equipment; tool head deformation of volume declined sharply, former head service life be extended; 3, spring-back of work-piece will also substantially smaller, improves process parts forming of precision; 4, metal flows evenly, prevent rupture of metal, stacked and fold, increase yield and forming quality.

Group I include plan 2, 3, 4 amplitude equal conditions for 0.08mm; group II include plan 5, 6, 7 amplitude equal conditions for 0.15mm; group III include plan 8,9,10 amplitude equal conditions for 0.3mm. Within each group, the vibration frequency change in turn. We can see that after you change the vibration frequency, forming force curve trend in much the same: within the 0-23s forming force rise from zero to the maximum the 600N, in the 23-25s down to 400N, the simulation ends. Within each group, forming force curve smoothness of the change is not obvious, but the higher the frequency, curved smoother trend.

In Fig.2a, 2b, 2c, plan 2, 5, 8 forming force curves is the smoothest, the forming force is maximum, respectively higher than under the same amplitude of vibration frequency curve (except 8). It seems to show us different vibration frequency on forming force has little effect in this simulation. Even so, 30Hz processing of vibration frequency is optimal in this simulation.

Plan 2, 5, 8 have the same vibration frequency as 30Hz; Plan 3,6,9 have the same vibration frequency as 50Hz; Plan 4,7,10 have the same vibration frequency as 100Hz. If to this be grouped, each group have the same frequency and the different amplitude. We can see that after the change in amplitude, in every group, forming force change trend of the curve seem to be the same as follows: curve less volatile, smooth, curve most volatile. So you can see: effect of amplitude on the forming is large, oversize or undersize amplitude will make the forming force have greater change. Processing, suitable amplitude is very important. In this simulation, optimum amplitude is 0.15mm.

Conclusion: changing frequency on forming force is not obvious, changing amplitude will have a greater impact on forming force. Frequency and amplitude form the comprehensive influence on forming force.

Fig.2c, amplitude condition is 0.3mm. Vibration frequency is 100Hz, forming force rate increases and be not suitable for forming, such as plan 10. This phenomenon demonstrates large amplitude is not suitable for machining with high frequency in the incremental forming. During the 7s of beginning processing, plan 9 is much smoother than plan 8. This describes the frequencies of the frequency ratio 30Hz is more conducive to forming than 50Hz; before close of 7s, plan 8 is smoother than plan 9, describes the frequencies of 50Hz is more conducive than that of 30Hz to forming. This shows that in the process of forming the beginning and end, forming force have a more complex change. This phenomenon in figure 2 is well attested. It's the best way to use different frequencies to process at this stage.

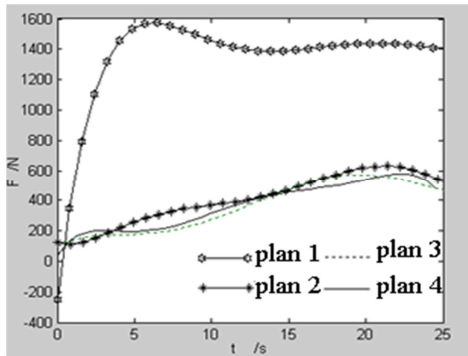


Fig.2a Amplitude 0.08mm different frequency forming force and time diagram

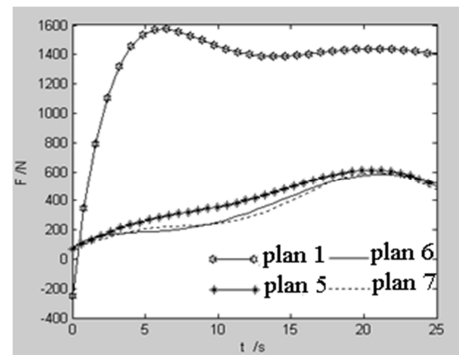


Fig.2b Amplitude 0.15mm different frequency forming force and time diagram

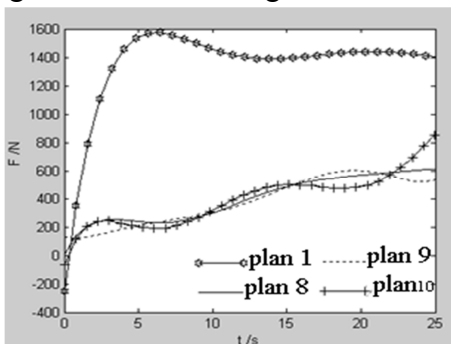


Fig.2c Amplitude 0.3mm different frequency forming force and time diagram

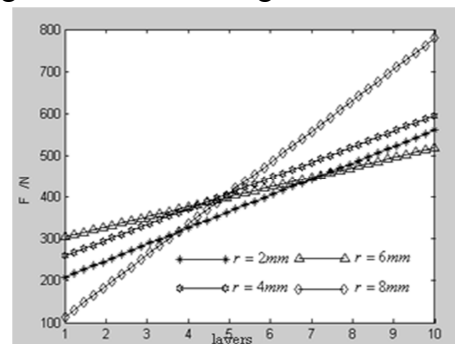


Fig.3a Forming force and layer diagrams under different tool radiuses

#### 4 Different tool radius and revolution speed effect on incremental forming

The radius  $r$  of the tool head is an extremely important process parameter in incremental forming. The uniformity of the machining deformation from consideration, bigger the tool radius, you can make the tool head lower trajectory overlaps part of the increase, thereby enhancing outer surface smooth finish, the better the performance. Instead, the radius  $r$  is undersize, it may cause the cutting phenomena, makes surface finish go wrong, even appear crack. [6]

Other conditions under certain conditions, forming tool Nose Radius  $r$  respectively take to [7]2mm,4mm,6 mm,8 mm and simulate of cylinder-shaped parts forming angle is  $45^\circ$ . Forming forces of different radius is shown in Figure 3. Entire forming process cost 25s and divide it in ten. The tool spent 2.5s on covering a layer. Take values on cylindrical same bus on each layer and get Figure 3.

Fig.3a shows: when  $r=8\text{mm}$ , forming force gradient maximum, when  $r=2, 4\text{mm}$ , forming force gradient basic; when the  $r=6\text{mm}$ , forming force gradient is minimal. Fig.3b shows: curve  $r=2\text{mm}$  time  $t=3, 20\text{s}$ , has two peaks; on curve  $r=4\text{mm}$   $t=20\text{s}$  when there is a peak and peak value minimum; on curve  $r=6\text{mm}$   $t=3\text{s}$  when there is a peak and peak maximum; on curve  $r=8\text{mm}$   $t=21\text{s}$  when there is a peak and peak maximum. From here we can see: the bigger the tool radius, forming force gradient is also bigger, forming force trend to be larger.

Due to changes in forming force large material flow is not easy to make uniform, causes metal buildup, tension crack, folds and other processing defects, so different machining part should be the appropriate choice of tool head, which makes forming force moderate values, change is also more stable. This simulation, the tool radius  $r=4\text{mm}$  is optimal.

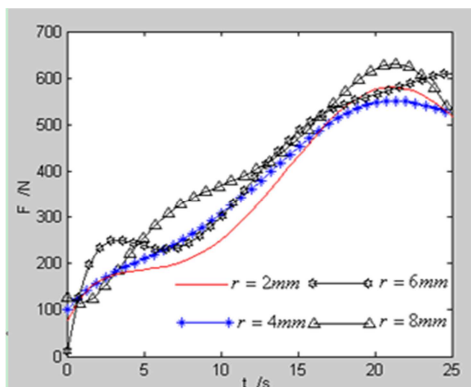


Fig.3b Forming force and timing diagrams under different tool radiuses

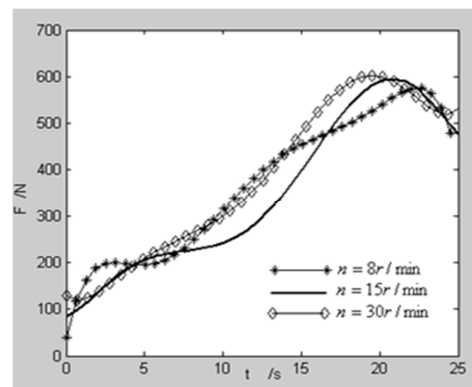


Fig.4 Forming force and time diagram under different revolution speeds

In forming process, the axis of rotation of the tool head around axisymmetric component. It speeds for the revolution speed of the tool head. Other experimental conditions must, take the revolution speed  $n$  to  $8r/\text{min}$ ,  $15r/\text{min}$ ,  $30r/\text{min}$ . Simulation results is shown in Fig.4. That can be seen from the diagram: tool head of the revolution speed has little impact on forming force, but its orbital speed, the lower, forming force curves the more tortuous; its orbital speed the higher, the forming force curves the more smooth. If tool head speed is too low, that can easily cause tool head adhesion of sheet metal; increasing resistance, metal flow caused by uneven; increasing the forming tool head revolution speed, help to mitigate this situation. When revolution speed is  $30r/\text{min}$  of forming tool head in simulations, curve is most smooth, so  $30r/\text{min}$  is optimal speed.

## 5 Consequences

The simulation experiment uses the DEFORM software on vibration experimental to simulate the incremental forming of sheet metal. That has some reference and guidance to the actual process at a later time.

- 1) Add vibration to the incremental forming and greatly reduce forming force to the benefit of extending the life of tool head and reducing defect of metal flow
- 2) Choosing the right vibration frequency, amplitude, tool head of radius and its revolution speed can make forming force change more smooth, is conducive to raising the quality and yield.
- 3) Determine the optimal value of the corresponding process parameters and have certain degree of significance to select the experimental and the actual production process parameters on the other conditions.

About the author: Cai Gaipin, male, born in 1964, E.D, Professor, his research interests on net (near) forming technology. E-mail: cgp4821@Yahoo.com.cn

This project is supported by National Natural Science Foundation of China (Grant No. 50975131)

## Reference

- [1] Ma Linwei, Mo Jianhua. Based on finite element simulation analysis of single point incremental forming of sheet metal [J]. Journal of Plasticity Engineering. 2007,12. 96~104
- [2] Cai Gaipin, Zhang Zhongkai, Jiang Zhihong. Mechanical analysis of the vibration of single point incremental forming of sheet metal [J]. Mechanical Science and Technology. 2010,7(29):915~920
- [3] Tenchev Rosen, Purnell Phil. An application of a damage constitutive model to concrete at high temperature and prediction of spalling. International Journal of Solids & Structures; Dec2005, Vol. 42 Issue 26, p6550~6565
- [4] Yin Changcheng, Wang Yuanxun, Wu Shengjun. Numerical simulation of single point incremental forming of sheet metal [J]. Journal of Plasticity Engineering. 2005,4:17~21
- [5] Li Xiangji, Li Mingzhe, Cai Zhongyi, Sun Yunming. Numerical simulation and experimental research on sheet metal incremental forming [J]. Materials science and technology. 2009,2.66~69
- [6] Li Hui. Complex sheet metal CNC incremental forming technology study [J]. Nanjing University of Aeronautics and Astronautics. 2007,3.
- [7] Zhao Bin. Single point incremental forming mechanism analysis and numerical simulation study [D]. Changchun, Jilin University, 2006:11-20.

## Graphene Based Ultrathin Composite Films Prepared by Layer-by-Layer Electrostatic Assembly and Spinning Coating

Yongqiang He<sup>1,2,a</sup>, Siyao He<sup>2,b</sup>, Qiaojuan Gong<sup>1,c</sup>, Jianping Gao<sup>2,d</sup>  
and Xiaodong Wang<sup>2,e\*</sup>

<sup>1</sup>Department of Applied Chemistry, Yuncheng University, Yuncheng 044000, China

<sup>2</sup>School of Science, Tianjin University, Tianjin 300072, China

<sup>a</sup>heyongqiang@126.com, <sup>b</sup>siyaohe@163.com, <sup>c</sup>gqjuan@163.com, <sup>d</sup>jianpinggaols@126.com  
<sup>e</sup>xdwangls@163.com

**Keywords:** Graphene oxide, Gelatin, Layer-by-Layer assembly, PVA.

**Abstract.** Ultra thin graphene oxide (GO)/polyvinyl alcohol and graphene-polyvinyl alcohol/gelatin composite films were fabricated by electrostatic layer-by-layer assembly and spinning coating methods. The assembling and coating process were traced with UV-visible absorption spectroscopy and the morphology of the formed ultra thin films was observed under scanning electron microscopy. The results show that the adsorption value of the GO based composite films linearly increased as the number of layers increased. The ultra thin graphene oxide/polyvinyl alcohol and graphene-polyvinyl alcohol/gelatin composite films have layered structure with high tensile strength because of the incorporation of GO. These strong ultra thin films have potential applications in coating, sensor and electrochemical devices.

### Introduction

Layer-by-layer assembly (LBL) is a rapid developed simple method to realize surface modification and obtain multifunctional surface or ultra thin films[1], and it has made great progress in the past decade. The materials used to assemble composites have been widely extended. New polyelectrolyte, such as dendrimer and polymer brush, and various colloids such as carbon nanotube have been used to fabricate composites by electrostatic LBL (ELBL)[2-5]. LBL method shows potential applications in anticorrosion, biotechnology and pharmaceuticals, photo and electric technology etc[3,6].

Graphene is ideal fillers for composite materials because of its high tensile modulus and ultimate strength. It can be added into polymers to form polymer based composites with special and different functions. For example, graphene oxide (GO)-polyvinyl alcohol (PVA) shows high strength[7,8], while GO-polyaniline has good electric properties[9-11]. Since GO is dispersed as a very thin nanosheets in solvents, it can be easily incorporated into composites through ELBL. In the present paper, GO is selected to fabricate GO base ultra thin composite films with high strength by ELBL and spinning coating (SC) methods.

### Experimental

#### Assembly of graphene oxide based ultra thin composite films

The glass slide was firstly treated according to the standard procedure and used as matrix. Various solutions including 1% PVA, 0.1% GO, 0.5% Gel (gelatin), GO/PVA solution (0.1% GO, 1% PVA) and 5% glutaraldehyde aqueous solution were previous prepared. In ELBL method, the treated glass

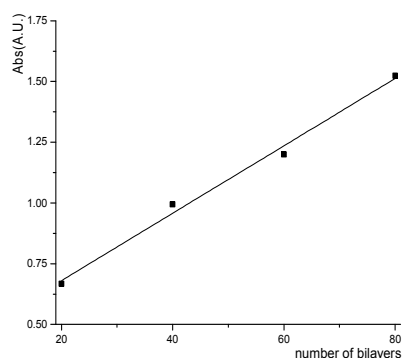
slide was dipped into 1% PVA solution for 5 minutes, rinsed with deionized water, flushed with pressed air and dried. Then PVA coated glass was dipped into 0.1% GO aqueous solution for 5 minutes, rinsed and dried again to obtain a double-layer. After ten double-layers were finished, the film was crosslinked for 30 minutes with 5% glutaraldehyde aqueous solution to strengthen the film. The above steps repeated again and again to form a GO/PVA film up to one hundred double-layers. Similarly, the GO-PVA/Gel film was assembled by using 0.5% Gel and GO/PVA aqueous solutions. In spinning coating method, the PVA and GO aqueous solutions were alternatively spinning coated (1.6k rpm) and dried in an oven at 60°C.

### Characterization

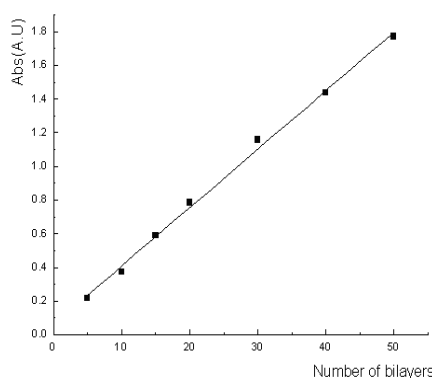
The assembly films were analyzed with Fourier transformed infrared spectroscopy (Perkin-Elmer Paragon-1000 FT-IR spectrometer), UV-vis spectrometer (TU-1901 UV-vis spectrophotometer) and scanning electronic microscope (JEOL-6700F ESEM). The mechanical properties of the films were tested using a Universal Testing Machine (Testometric, UK).

### Results and discussion

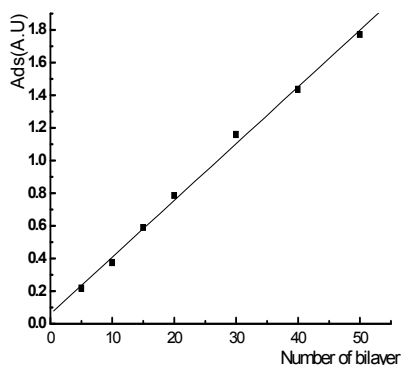
Electrostatic layer-by-layer assembly and spinning coating are useful methods to realize surface modification and obtain multifunctional surface or ultra thin films. Here, we apply these two methods to fabricate graphene based ultra thin films using PVA solution, GO-PVA solution and GO solution as precursors. The glass slides gradually turn dark as the assembling or coating goes on



(a) GO/PVA (ELBL)



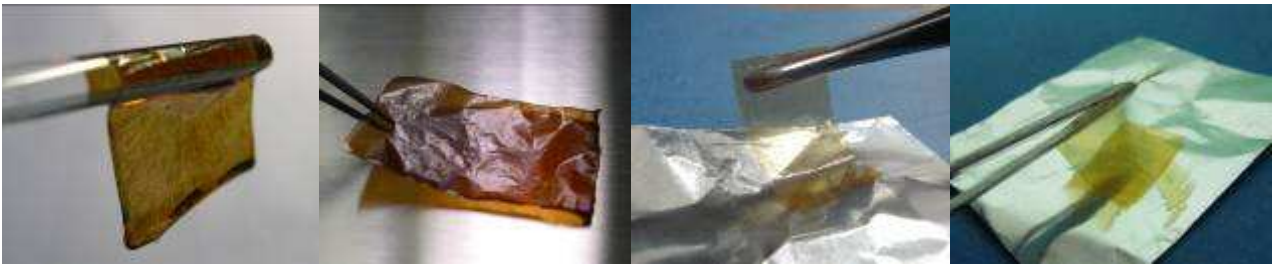
(b) GO/PVA (SC)



(c) (GO-PVA)/Gel(ELBL)

Fig.1 UV- adsorption of GO/PVA and GO-PVA/Gel films (350nm)

and this indicates the thickening of the composite coating layer, which was traced with UV visible absorption spectroscopy and the results are shown in figure 1. The adsorption value of the GO based composite films linearly increased as the number of layers increased for GO/PVA films by both ELBL and SC. However, the ELBL film has lower adsorption than SC film, indicating the thickness of ELBL film is thinner than that of SC film under the same number of layers. Besides, (GO-PVA)/Gel film by ELBL is thicker than GO/PVA (ELBL), but thinner than GO/PVA (SC), because the concentration of GO-PVA solution is high. The above difference in thickness can be directly observed as shown in figure 2. These films have one hundred double-layers. Obviously, SC method can produce ultra thin GO-PVA films, but ELBL can make even thinner GO/PVA and (GO-PVA)/Gel films. So GO/PVA films by ELBL are elastic and transparent while the films by SC



(a) GO/PVA (SC, wet) (b) GO/PVA (SC, dry) (c) GO/PVA (ELBL) (d) (GO-PVA)/Gel (ELBL)  
Fig.2 Optical photos of GO/PVA films at wet (a) and dry state (b,c) and GO-PVA/Gel films (d)

are brown and translucent. At wet state, the films turn to hydrogel that has high strength because of crosslinkage by glutaraldehyde and integration of GO. This high strength and stability in wet state will offer potential applications in tissue engineering and surface modification.



(a) 0.05%GO/PVA (SC) (b) 0.1%GO/PVA (SC) (c) 0.15%GO/PVA (SC)  
Fig.3 Optical photos of GO/PVA films with 50 double-layers made from different PVA concentration

Meanwhile, we also investigate the effect of GO concentration on the GO/PVA films. The films became thick and dark as the GO concentration increased (figure 3).

Figure 4 gives low (A, C) and high magnification (B, D) SEM photos of GO/PVA films (50 double-layers) by ELBL and SC methods. The thickness of ELBL film is about  $1\mu\text{m}$ ; while that of SC film is about  $10\mu\text{m}$ , almost ten times of that of ELBL film. We can clearly see the layer structure of the GO/PVA films.

Graphene is ideal fillers for composite materials because of its high tensile modulus and ultimate strength. When GO was assembled into the GO/PVA (PVA/0.1%GO, 50 double-layers) or (GO-PVA)/Gel (50 double-layers) composite films, the tensile strength increased by 3 folds. The tensile strength can be further improved by increasing GO concentration or forming covalent between GO and polymers.

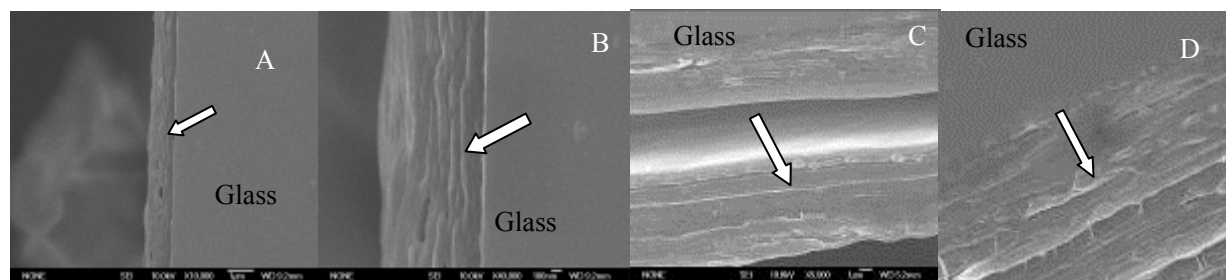


Fig.4 SEM photos of GO/PVA films (50 double-layers) by ELBL (A, B) and SC (C, D) methods

## Conclusions

We have successfully prepared ultra thin graphene oxide (GO)/polyvinyl alcohol and graphene-polyvinyl alcohol/gelatin composite films were fabricated by electrostatic layer-by-layer assembly and spinning coating methods. The light adsorption value of the GO based composite films linearly increased as the number of layers increased. The ultra thin graphene oxide/polyvinyl alcohol and graphene-polyvinyl alcohol/gelatin composite films have layered structure with high tensile strength because of the incorporation of GO. These strong ultra thin films have potential applications in coating, sensor and electrochemical devices.

## Acknowledgments

This work was supported by Tianjin Municipal Science and Technology Commission of P. R. China (09JCZDJC23300) and National Science Foundation of China (No. 21074089).

## References

- [1] G.Decher and F.Nanoassemblies: Science Vol. 277(2010), p. 1232-1237.
- [2] M.Ferreira, O.Onitsuka, W.B.Stockton et al: Photonic and Optoelectronic Polymers Vol. 29(1997), p. 437-444.
- [3] M.Dean, D.L.Champ and T.H.Paula: Chromogenic Phenomena in Polymers Vol. 888(2004), p. 18-33.
- [4] S.Srivastava: Accounts of Chemical Research Vol. 41(2008), p. 1831-1841.
- [5] J. Wang, G.D.Liu, Y.H.Lin: Biomolecular Catalysis Vol. 986(2008), p. 117-128.
- [6] M.Ferreira, O.Onitsuka, W.B.Stockton et al: Photonic and Optoelectronic Polymers Vol. 672(1997), p. 437-444.
- [7] Y.Matsuo, K.Tahara and Y.Sugie: Carbon Vol. 34(1996), p. 672-674.
- [8] Lei Jiang, Xiaoping Shen, Jili Wu: Journal of Applied Polymer Science Vol. 118(2010), p. 275-279,in Chinese.
- [9] T.Cassagneau, J.Fendler, S.Johnson et al: Advanced Materials Vol. 12(2000), p. 1363-1366.
- [10] Jihuai Wu, Qunwei Tang, Hui Sun et al: Langmuir Vol. 24(2008), p. 4800-4805,in Chinese.
- [11] S.Bourdo and T.Viswanathan: Carbon Vol. 43(2005), p. 2983-2988.

## Analysis of the Stability of POY Filament Structure and Properties Spun by WINGS System

Bin Yang<sup>1,2,a</sup>, Zhiyong Yan<sup>1,b</sup> and Yuan Xue<sup>1,c</sup>

<sup>1</sup> College of Material and Textile Engineering, Jiaying University, Jiaying 314000, Zhejiang, China

<sup>2</sup> College of Textiles, Donghua University, Shanghai 201620, China

<sup>a</sup> ybyy23@163.com, <sup>b</sup> zzyong77@163.com, <sup>c</sup> xuexuan168@yahoo.com.cn

**Keywords:** WINGS, Crystallization, Orientation, Mechanical properties.

**Abstract.** Comparing the crystal orientation of the structure, tensile properties, boiling water shrinkage rate between difference filament rolls in the same spinning position spun by WINGS POY system and tradition ACW POY system, it is found that there are differences in orientation degree, crystallinity, tensile strength, elongation at break, initial modulus and boiling water shrinkage rate between difference filament rolls in the same spinning position. Coefficient of variation of the experimental values of WINGS POY system is lower than traditional ACW POY system.

### Introduction

Now the equipments of spinning manmade fiber are more efficiency and energy conservation and more stability and more integrated. WINGS(Winding INtegrated Godet Solution) is a new spinning system which is researched by Oerlikon Barmag Company. This system is efficiency and save room and Convenient operation. Compare with traditional spinning system, WINGS system integrate the guide roller and network devices to the winding head, effectively reducing deflection angle between the tow, reducing the difference between cake POY filament yarn structure and properties differences, making the product quality has been improved[1~3].

### Features of WINGS System

Spinning process of WINGS POY:

Polyester melt→Spinning box→Spinneret extrusion→Ring quenching→Oil cluster→Guide wire hook→First guide wire roll→Network nozzle→Second guide wire roll→Winding→POY yarn roll.

Spinning process of traditional ACW POY:

Polyester melt→Spinning box→Spinneret extrusion→Ring quenching→Oil cluster→Guide wire hook→Network nozzle→First guide wire roll→Second guide wire roll→Winding→POY yarn roll.

The wrapping difference for conventional ACW POY spinning plants is 28 degrees, while WINGS reduces this to only 7 degrees[3]. This guarantees a more even and hence an overall improved yarn quality within a winding position.

### Preparation of Fiber Experiment

**Equipments.** The PET melt is spinned in spinning box both using Barmag SP8X type box. Winder is the WINGS POY winder head and ACW winder of Oerlikon Barmag. Every spinning position has 10 POY filament rolls.

**Process Parameters.** Polyester melt intrinsic viscosity is  $[\eta] = 0.643 \text{ dL/g}$ , content of carboxyl end is  $32.7 \text{ mol} \cdot \text{t}^{-1}$ . Table 1 shows the spinning process parameters. WINGS POY process take whole one spinning position rolls as samples, ten samples which number W-1 to W-10 from the inside to the outside of the WINGS POY winder. In the same way the samples of traditional ACW process craft number A-1 to A-10.